9-5-2013

Novel etch studies and passivation techniques on InAs/GaSb superlattice based infrared detectors

Maya Narayanan Kutty

Recommended Citation

Narayanan Kutty, Maya. "Novel etch studies and passivation techniques on InAs/GaSb superlattice based infrared detectors." (2013). https://digitalrepository.unm.edu/ece_etds/188

Maya Narayanan Kutty

Candidate

Electrical and Computer Engineering

Department

This dissertation is approved, and it is acceptable in quality and form for publication:

Approved by the Dissertation Committee:

Prof. Sanjay Krishna , Chairperson

Prof. Ganesh Balakrishnan

Prof. Elena Plis

Prof. Jamie Phillips

Novel Etch Studies and Passivation Techniques on InAs/GaSb Superlattice based Infrared Detectors

by

Maya Narayanan Kutty

M.S., Electrical Engineering, University of New Mexico, 2007
B.E., Electronics and Communication Engineering, Bangalore University, Karnataka, India, 2001

THESIS

Submitted in Partial Fulfillment of the
Requirements for the Degree of

Doctor of Philosophy
Engineering

The University of New Mexico

Albuquerque, New Mexico

July, 2013

Dedication

Dedicated in memory of Nagaraj Sir-the most inspirational, dedicated teacher and human being!

Dedicated to my eternal life forces
- Mom, Dad and my beloved sister Chaya.

``The most beautiful thing we can experience is the mysterious. It is the source of all true art and all science. He to whom this emotion is a stranger, who can no longer pause to wonder and stand rapt in awe, is as good as dead: his eyes are closed.´´

-Albert Einstein

Acknowledgments

I would like to thank my advisor and dissertation chair, Prof. Sanjay Krishna for giving me the opportunity to work under his tutelage on this dissertation. I am grateful for all his support and guidance throughout these grueling years of research. I have indebted to him for all patience he has shown me in accommodating my various bouts of unfortunate health issues. This incredible journey has molded me and will remain to be the Rosetta stone for the rest of my career.

I would like to thank my committee member, colleague, and mentor Dr. Elena Plis, for her friendship, support, patience and guidance throughout my years of research at CHTM. I am indebted to her for all the time and effort she has put in the long months writing, rewriting and editing journal manuscripts, presentations and these dissertation chapters. The patience she has shown towards me is superhuman and it will remain with me for the rest of my life. I would like to thank my committee member, and friend Prof. Ganesh Balakrishnan, for his friendship, support, humor and candor throughout these years both at work and outside. Even though our roles have changed over these years, his encouragement has been unwavering. It has been a privilege to have worked with him and to learn from him.

I would like to thank my committee member Prof. Kateryna Artyushkova for her knowledge, expertise, time and kindness. I have had the incredible privilege and learning experience to work with her on the XPS on SLS project. For the past almost 3 years she has shown me an endless amount of patience, accommodated my every crazy idea and ran the XPS machine for hundreds of hours on a countless number of samples.

I would like to thank my committee member Prof. Jaime Phillips for his time and valuable recommendations pertaining to this study. I would like to thank Prof. Phillips and his team at University of Michigan, Ann Arbor, for depositing many rounds of ZnTe for our passivation study on SLS. I am truly grateful to them for their time and effort in accommodating this study into their schedule and work.

I would like to thank my friend, my Zen-master (Gandalf in plain clothes) and mentor Dr. Rajeev Shenoi, for his unwavering friendship, endless hours and inexhaustible patience. It has been a privilege to have worked with him and the lessons learnt will last a lifetime, but the kindness he has shown will last beyond.

I would like to thank my friends and colleagues Dr. Stephen Myers, Dr. Ajit Barve, Dr. Nutan Gautam, Dr. Thomas Rotter, Dr. Ashwin Rishinaramangalam, Brianna Klein, and rest of the gang in CHTM room # 117 for their friendship, support, endless discussions pertaining to everything under the sun over numerous cups of coffee/tea. I would like to thank my colleagues Dr. HaSul Kim and Dr. Sang Jun Lee for helping me out in the cleanroom. I would like to especially thank all the member of our group past and present for all their help throughout my years at CHTM. It has been a privilege and honor to have worked along such a wonderful talented group of people.

I am indebted to the cleanroom staff Douglas Wozniak, Steve Wawrzyniec, Beth Fuchs, Dan Bryant, and Rick Bradley for training me on ever equipment in the cleanroom and accommodating my every bizarre request/idea in the cleanroom. This thesis would not have been possible if it were not for their endless patience and support. I would like to also thank all the staff at CHTM especially to Kerry Blecha, Jannell Vander Grift, Karen Walker for their kindness and patience in accommodating my always time-sensitive/ nth minute requirements. I would like to extend a very special note of thanks to ECE graduate coordinator Elmyra Grelle for her friendship, wisdom, words of encouragement and for handling the mountain of paper work that has gone into me achieving a graduate degree.

I would like to thank all my friends and extended family here in Albuquerque,in the US, and back in Bangalore, India for their friendship, encouragement and understanding they have bestowed upon me for all these years. I would like to thank Prof. Anantha Iyer (Anna) for being a constant confidante and presence throughout my life. His belief in my bright future and the love for English poetry he imbibed in me, are everlasting.

I would like to thank my Mom and Dad for their endless support, and unwavering love. This dissertation is a culmination of their inexhaustible hours and efforts they spent in teaching me, inspiring me and molding me. Lastly, I would like to thank the most important person in my life, my best friend, my eternal cheerleader, my baby sister Chaya. Her humor, encouragement and unwavering faith in me has sustained me through darkest of times and made this dissertation possible.

This dissertation is dedicated to my family as they saw in me a light I have never been able to see. Mere words of thanks are not enough to describe the gratefulness I feel and the sacrifices they have made for me can never be recompensed. I can only hope that my life, my work and my being can be a testament to them. As I move on to the next destination in my journey their life lessons, and love are my eternal harbor.

``That best portion of a good man's life, his little, nameless, unremembered acts of kindness and of love ´´- from `Tintern Abbey ´by William Wordsworth.

Novel Etch Studies
and Passivation Techniques on InAs/GaSb Superlattice based Infrared Detectors

by

Maya Narayanan Kutty

M.S., Electrical Engineering, University of New Mexico, 2007
B.E., Electronics and Communication Engineering, Bangalore University, Karnataka, India, 2001

PhD, Engineering, University of New Mexico, 2013

Abstract

Infrared (IR) detectors today are being utilized for a variety of imaging applications such as medical diagnostics, navigation instruments of automobiles and aircrafts, meteorological imaging, night-vision and fog/smoke imaging, surveillance, target acquisition and astronomical/space imaging. These wide ranging implementations have given rise to varied design requirements for these devices such as the required sensitivity, operating temperature, spectral sensitivity, peak wavelength and cost. Type-II band aligned InAs/Ga(In)Sb strained layer superlattice (SLS) material system proposed for the IR detection in the 1970s has been considered in recent years as an interesting alternative to the present day IR detection technologies. Type-II SLS technology posses mature growth technologies

able to achieve uniformity over large areas along with band-gap tunability which results in IR detectors in mid wave (MW), long-wave (LW) and very long-wave infrared (VLWIR) ranges. The large electron effective mass in SLS help in reducing inter-band tunneling and hence allow for longer-wavelength operation in these IR detectors. Large splitting between heavy-hole and light-hole valence subbands due to strain in the SLSs contributes to the suppression of Auger recombination and this enables significantly higher operating temperatures. The commercialization of type-II SLS technology has been hindered by material defects that promote excess dark currents in the bulk and on detector surfaces. During SLS device fabrication the mesa delineation leads to discontinuity of the periodic crystal structure which results in formation of unsatisfied chemical bonds on the etched surfaces and hence enhancing the surface leakage currents. More-over, with the scaling of single pixel dimensions, the performance of focal plane arrays is strongly dependent on surface effects due to the large pixels surface to volume ratio. Hence the reduction of surface leakage currents in LWIR detectors has become a technological necessity and is the objective of this dissertation.

This work focuses on performance improvement of InAs/GaSb SLS LWIR detectors by optimization of mesa delineation and surface passivation techniques. The first part of the dissertation works on the development of optimized etching scheme for the 400μm x 400μm area single-pixel SLS detectors and for 25μm x 25μm area focal plane arrays (FPAs). Firstly, optimization of wet chemical etches were carried out on GaSb substrates and reported here is that HCl:H_2O_2:H_2O (1:1:4) solution rendered the smoothest etched surface with a root mean square (RMS) roughness of 1.59nm. This work also reports the results of comparison of mesa sidewall profiles of InAs/GaSb SLS single-pixel and FPA detectors obtained after (a) a conventional BCl_3 gas based inductively coupled plasma dry etch, (b) a HCl:H_2O_2:H_2O (1:1:4) solution wet chemical etch and (c) combination of both. It was found that HCl:H_2O_2:H_2O (1:1:4) solution wet etch was ideal for single pixel mesa delineation, but not on FPA device proportions. In the etch study experiments, the InAs/GaSb SLS structure was looked at as one single entity and as an amalgamation of its constituents InAs and GaSb materials.

The second part of this research deals with the development of efficient surface passivation methods for the long wave infrared (LWIR) SLS detectors with pin, pBiBn, and graded bandgap designs. A comparative study of dielectric passivants (Silicon di-oxide and Silicon nitride) versus organic passivant of SU-8 versus chalcogenide passivants (Zinc Sulfide, Ammonium Sulfide and Electro-chemical passivation i.e. deposition of pure sulphur) were carried out on InAs/GaSb SLS LWIR single-pixel detectors. Ammonium sulfide [$(NH_4)_2S$] treatment and electrochemical sulfur deposition (ECP) reduced dark current density (J_d) at 77K and applied bias= - 0.1V by (a) by factor of 25 and 200 in InAs/GaSb SLS LWIR detector with p-i-n design and (b) by factor of 3 and 54 in InAs/GaSb SLS LWIR with pBiBn design. In the comparative study of all the sulphur-based passivants of thioacetamide (acid-based and base-based), $(NH_4)_2S$ and ECP on graded-bandgap design based single-pixel LWIR SLS detectors, ECP showed superior performance of all with the highest surface resistivity ($r_{surface}$) of $1.4 x 10^5$ Ω-cm at 77K. In the long term stability study of ECP, it showed degradation over time with J_d=0.09A/cm^2 right after passivation and J_d =2.18A/cm^2 after 4 weeks of passivation. Hence as an alternative to ECP (i.e. sulphur passivation), we propose the utilization of novel chlorine-doped Zinc Telluride (ZnTe:Cl) as a passivation technique. It is for the first time that ZnTe:Cl has been used as a passivation technique on any IR device. This novel ZnTe:Cl passivation technique is implemented on InAs/GaSb SLS LWIR single-pixel detectors with pin and graded-bandgap designs. Though ECP showed a superior $r_{surface}$=10^{5}Ω-cm over ZnTe:Cl passivation with rsurface =6700Ω-cm, ZnTe:Cl passivation had almost no degradation over time. Hence an improved ZnTe:Cl with its robust, uniform passivation layer has the potential to replace ECP in FPA fabrication on InAs/GaSb SLS LWIR detectors and there-of take these high-performing SLS-based IR detectors to commercialization.

Contents

List of Figures

List of Tables

Glossary

SLS	Strained Layer Superlattice
IR	Infrared (detector or radiation)
MWIR	Mid-wave infrared (wavelength range)
LWIR	Long-wave infrared (wavelength range)
FPA	Focal Plane Array
MCT	Mercury Cadmium Telluride (detector)
QE	Quantum Efficiency
R	Responsivity
D^*	Specific Detectivity
R_0A	Zero bias dynamic resistance area product
$r_{Surface}$	Surface Resistivity

Chapter 1

Introduction

All objects with temperature above absolute zero (0K) emit photons. The photon emission spectrum of objects is determined by Planck's law

$$W(\lambda, T) = \frac{2\pi hc^{1/2}}{\lambda^5} \cdot \frac{1}{e^{\frac{hc}{\lambda kT}} - 1} \tag{1.1}$$

where h is the Planck's constant, k is the Boltzmann's constant, c is the speed of light, and λ is the wavelength of light. Units of $W(\lambda, T)$ are $(W/m^2/\mu m)$. This has been plotted in Figure 1.1.

The emission spectrum of objects at room temperature (295K) peaks at a wavelength of 9.8 μm, which falls in the infrared (IR) range, according to Wien's displacement law.

$$\lambda_{max}(\mu m) = \frac{2898}{T(K)} \tag{1.2}$$

IR radiation is referred to the electromagnetic wave with wavelengths that span between the visible light region and microwaves. IR region covers the ranges from

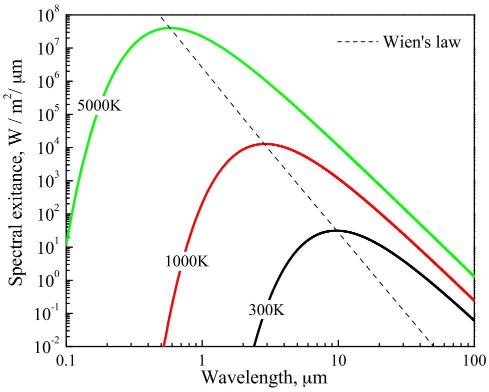

Figure 1.1: Planck's law for a number of black body temperatures. Dashed line represents Wien's law.

0.75 μm to 1000 μm. IR radiation is beyond sensitivity of human eye, however, it can be sensed as a heat. This gave rise to the development of IR detectors, devices which transduce the energy of electromagnetic radiation falling upon them into some other form, in most cases, electrical. Windows in atmospheric absorption are used to classify IR radiation to near infrared (NIR) corresponding to wavelengths from 0.7 to 1.5 μm; short wavelength infrared (SWIR) from 1.5 to 2.5 μm; midwave infrared from 3 to 5 μm; longwave infrared radiation (LWIR) from 8 to 14 μm; very longwave infrared (VLWIR) from 14 to about 32 μm, and terahertz (THz) or far infrared (FIR) from 32 μm to 1000 μm. These regimes are described in Fig 1.2 along with the spectral transmittance of IR radiation in atmosphere. The applications of imaging in the 325 μm regime include medical diagnostics for skin cancer detection; defense for target acquisition, missile detection and tracking, mine detection, surveillance, and biological/chemical agent identification; imaging through fog and fire for search and rescue; navigation instruments in aircrafts and automobiles; imaging weather patterns; and extracting information on temperature and spectral content of far away constellations through space fog.

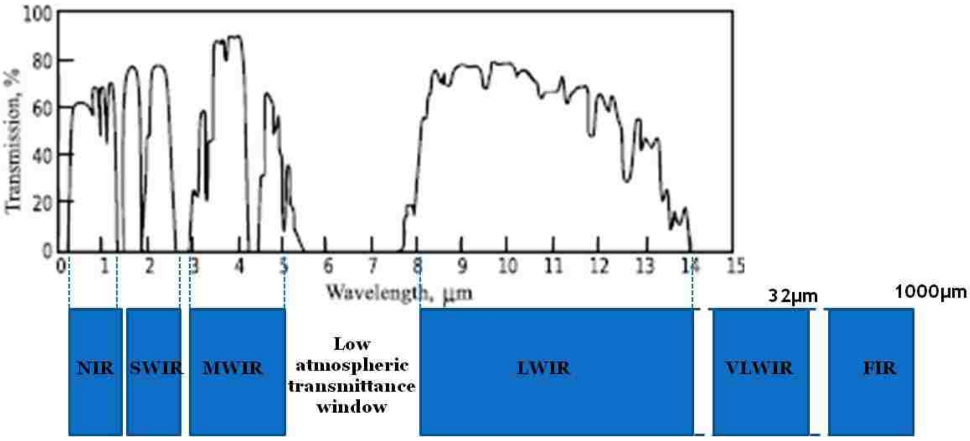

Figure 1.2: Plot of Transmittance of the atmosphere for a 6000ft horizontal path at sea level [54] along with the windows of infrared radiation.

1.1 Infrared Detectors

IR detectors may be divided into two broad classes, thermal and photon detectors. Thermal detectors respond to the heat generated by the absorbed energy of the optical radiation whereas the principal of operation of photon detectors is based on the direct interaction of the optical radiation with the atomic lattice of material.

In thermal detectors (Si-based microbolometers, pyrometers, thermocouples, Golay cells, and superconductors) incident optical radiation increases the temperature of the detector which leads to a change in physical parameters, such as resistance or voltage. Some of the characteristic features of thermal detectors are broad spectrum, room temperature operation, low cost, and slow response. Photon detectors generate free electrical carriers through interaction of photons and bound electrons. The interaction of light and matter produces a parameter change (resistance, conductance, voltage or current) that is detected by an associated circuitry. Photon detectors for IR are typically realized using III-V and

II-VI semiconductors, and can further be divided into intersubband and interband detectors.

Examples of intersubband detectors are quantum well infrared photodetectors (QWIPs) and quantum dot infrared photodetectors (QDIPs), where intersubband transition energies in the conduction band can be tailored to detect infrared radiation. Examples of interband detectors are HgCdTe (MCT), InSb, and InAs/GaSb type-II strained layer superlattice (SLS) systems.

For applications in the LWIR regime with low volume and high cost, such as in astronomy, the MCT technology is the dominant one. Though MCT detectors have demonstrated high sensivity and very low noise, due to problems in the epitaxial growth of mercury-based compounds, there is limited manufacturing yield for MCT large area focal plane arrays (FPAs) and hence leading to very expensive final imaging systems. InSb detectors are commercially used for the detection of MWIR radiation, and need cryogenic cooling. Also, they are not suited for multicolor detection. QWIP is well established and commercially available technology in the LWIR regime due to the relatively inexpensive growth and fabrication of III-V semiconductors, but they exhibit higher dark currents, low quantum efficiency, cryogenic operating temperature along with the inability to absorb normal incident light. In our research described in this dissertation we focus solely on InAs/GaSb type-II SLS detectors and hence they are described in detail in the next section.

1.2 InAs/GaSb Type-II SLS Detectors

InAs/(In,Ga)Sb type-II SLSs were first proposed as an IR sensing material in 1980s by Sai-Halasz, Tsu, and Esaki [111, 34]. IR detectors based on SLSs have been under investigation ever since they were suggested several decades ago by Smith

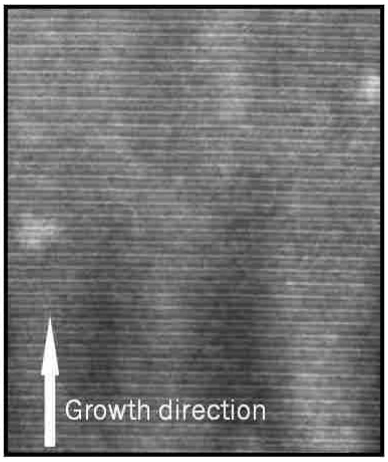

Figure 1.3: TEM image of a 13MLInAs/7ML GaSb LWIR SLS structure. TEM image was taken by Evans Analytical Group.

and Mailhiot [30]. In 1990, Chow and coworkers reported the first $Ga_{1-x}In_xSb$/InAs SL material with high structural quality, LWIR photoresponse, and LWIR photoluminescence [71]. While theoretical predictions of detector performance seem to favor the InAs/InGaSb system due to the additional strain provided by the InGaSb layer, the majority of the research in the past five years has been focused on the binary InAs/GaSb system. This is attributed to the complexity of structures grown with the large mole fraction of In.

The InAs/GaSb SLS consists of alternating layers of nanoscale materials whose thicknesses vary from 4 to 20 monolayers (MLs). This is seen in the transmission electron microscopy (TEM) image of a 13MLInAs/7ML GaSb LWIR SLS structure in Fig. 1.3. The overlap of electron (hole) wave functions between adjacent InAs (GaSb) layers results in the formation of electron (hole) minibands in the conduction (valence) band. Optical transitions between holes localized in GaSb layers and electrons confined in InAs layers are employed in the IR detection process (Fig. 1.4). Thus, using two mid-bandgap semiconductors, devices can be fabri-

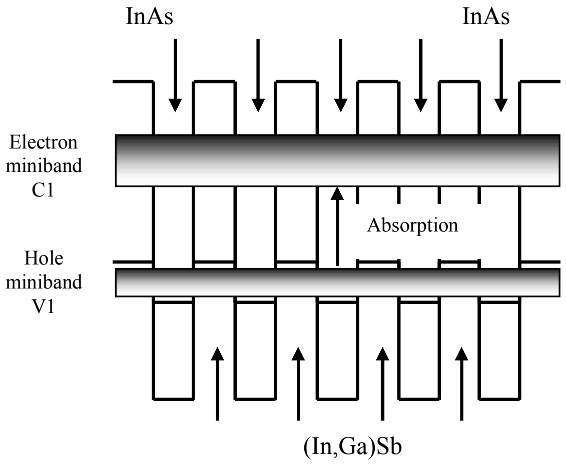

Figure 1.4: Absorption in InAs/(In,Ga)Sb type-II SL

cated with operating wavelengths anywhere between 3 and 32 μm [19, 39, 128].

Tunneling currents in SLS are lower than in MCT detectors of the same bandgap due to larger electron effective mass [30]. Auger recombination is suppressed due to the large splitting between heavy-hole and light-hole valence subbands[132, 43]. Moreover, the SLSs are less sensitive to the bandgap variations due to compositional nonuniformities than the MCT alloys with the same bandgap [44]. In contrast with QWIPs, normal incidence absorption is permitted in SLSs, contributing to high conversion quantum efficiency. Two factors provide SLSs with technological advantages over competing technologies: commercially available low defect density substrates and a high degree of growth and processing uniformity over a large area. FPAs of sizes up to 1024 × 1024 pixels have been demonstrated using the SLS material system, highlighting the potential of this technology [46]. Moreover, several research groups within the last years have reported on high performance InAs/GaSb SLS IR detectors and FPAs for MWIR [103, 129, 90], LWIR [124, 123, 45, 39, 27], and VLWIR [127, 51] spectral regions. Thorough comparisons between MCT, InSb, QWIP, and SLS technologies can be found in the literature [60, 4, 110].

1.3 Motivation

Despite the numerous advantages SLSs offer over present-day detection technologies, including reduced tunneling currents, normal-incidence absorption, and suppressed Auger recombination, the promise of superior performance of SLS detectors has not been yet realized [107], as shown by comparison of dark-current densities in SLS detectors with the MCT benchmark (“Rule 07”). The dark-current density demonstrated by the SLS detectors is significantly higher than that of bulk MCT detectors, especially in the MWIR spectral range, as illustrated in Fig. 1.5. Abbreviations for the different institution working on SLS detectors: Fraunhofer-Institut (IAF), Jet Propulsion Laboratory (JPL), Naval Research Laboratory (NRL), Northwestern University (NWU), Raytheon Vision Systems (RVS), University of California, Santa Barbara (UCSB), Columbia University (Columbia), University of Illinois, Urbana-Champaign (UIUC) and University of New Mexico (UNM).

Generally, there are three major components of dark current in detectors based on narrow band gap semiconductors; generation current associated with the Shockley-Read-Hall (SRH) process in the depletion region of the detector, thermally generated diffusion current associated with Auger [109] or radiative process in both the n- and p- extrinsic regions of the detector, and a surface current associated with the surface states in the junction.

With the SRH and thermally generated diffusion currents in SLS detectors being greatly reduced by the intricate heterostructure engineering [123, 39], the surface current remains a dominant contributor to the total dark current. During the individual pixel isolation process, the periodic crystal structure terminates abruptly

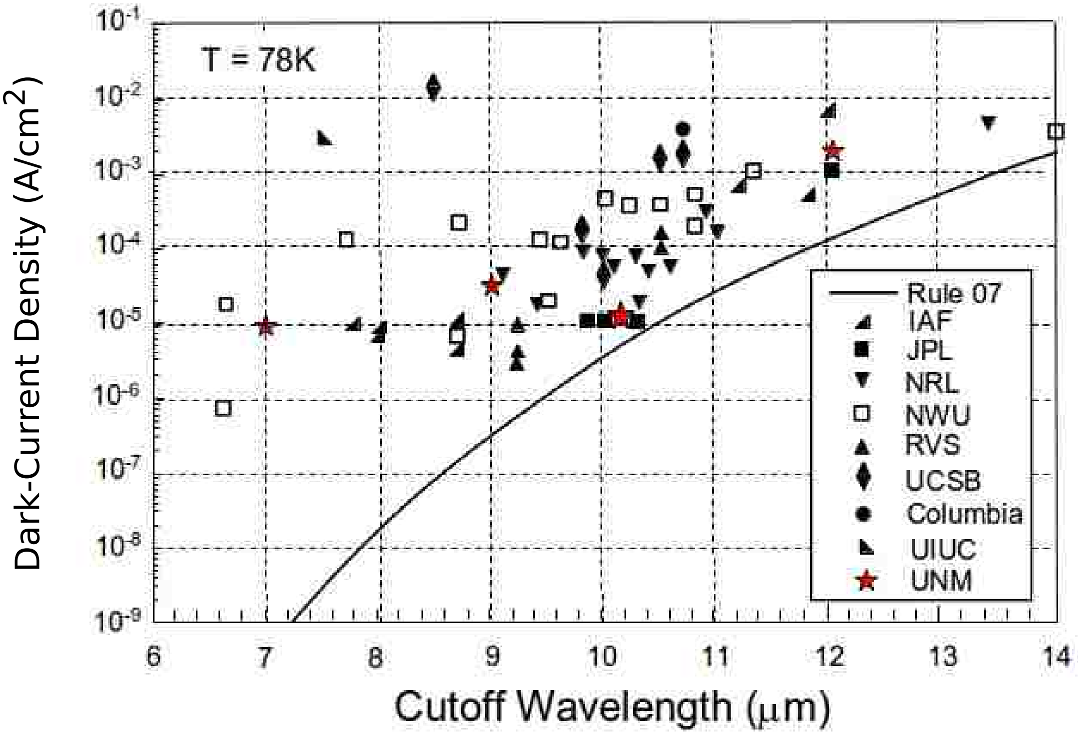

Figure 1.5: Dark-current density of SLS detectors compared with Rule 07. Modified and reprinted from [107].

resulting in formation of unsatisfied (dangling) chemical bonds responsible for generation of surface states within the bandgap. These states cause pinning of the surface Fermi level near the midgap and, as a consequence, enhance the surface leakage currents. Moreover, the surface leakage currents become a dominant contributor to the dark current for FPA pixels with mesa dimensions of $\sim 20\mu$m. Thus, in order to improve the overall device performance, methods for elimination of surface currents, i.e. passivation treatments, have to be developed for InAs/GaSb SLS material system.

The FPA pixel dimensions and high fill factor give rise to problems of accurate mesa dimensions and edge definition control. Furthermore, passivation treatment applied to the etched surfaces that are rough, or contaminated by native oxides and foreign particles, will result in little or no improvement of device performance. Effective methods of native oxide removal or thinning have to be incorporated into the device fabrication sequence prior the passivation step.

1.4 Dissertation Overview

This dissertation is organized as follows: Materials and characterization techniques used in the course of this work are presented in Chapter 2. Mechanisms of surface oxide formation and review of various passivation techniques of InAs/GaSb SLS detectors are in detail discussed in Chapter 3. Chapter 4 covers our efforts to develop an optimized etch for the mesa delineation of SLS detectors.Chapter 5 details the effect surface modifications make on performance of InAs/GaSb SLS LWIR detectors utilizing the common IR detectors figures of merit, i.e., responsivity, quantum efficiency, dynamic impedance area product, surface resistivity and specific detectivity. In Chapter 6, we summarize all the major accomplishments laid out in this dissertation. Lastly, in Chapter 7 we will introduce a few future endeavors we have worked on for improving performances of InAs/GaSb SLS detectors and FPAs.

1.5 Contribution of this dissertation

The aim of this research is to form a better understanding of the various mechanisms existing at the surface of the device. It is near impossible to obtain an immaculate or ``good´´surface, but we strive to eliminate as many detriments as possible to form an `ideal surface´. This dissertation has focused solely on improving the performance of LWIR InAs/GaSb SLS detectors by modifying the surface of the device. The surface we study is generated after the mesa etch phase of device fabrication and encompassed the mesa/device sidewall along with all exposed area on/around the mesa. To achieve the ideal surface, we took 2 distinctive approaches:

1. Prepare an ideal surface with optimized mesa etch technique. This experiment deals with our efforts to obtain an ideal etch that would in-turn lead to an ideal surface for the mesa structure in our devices.
    (a) The first critical contribution of this study was the optimizing an ideal wet etch on the GaSb substrate/surface. We concluded from our experiments that HCl:H_2O_2:H_2O (1:1:4) gave the least amount of debris i.e. an etch remnant free surface, with an rms roughness of 1.59nm and etch rate of 1.9μm/min [70]. This result is significant as it can be applied to any GaSb-based device material system.

    (b) We then study the effects of translating the optimized wet etch onto a 400μmx400μm area single-pixel SLS structure. In this experiment we subjected the InAs/GaSb LWIR SLS detector structure with pin design, to three techniques of mesa etch, namely, (i) Optimized wet etch of HCl:H_2O_2:H_2O (1:1:4), (ii) BCl_3 based plasma dry etch and (iii) combination of both wet and dry etches. The experiment established that the wet etch produced less damage and least amount of etch residue than dry etch but with a reasonable undercut of 5μm [70].

    (c) The optimized wet etch of HCl:H_2O_2:H_2O (1:1:4) was found unpractical on 24μmx24μm area FPAs based on InAs/GaSb LWIR SLS structure. This was due to the 9μm lateral etch/undercut produced during the process. This experiment ascertained that BCl_3 based plasma dry etch is essential in FPA fabrication in order to maintain the device dimensions.

   (d) In our etch study experiments, we looked at the InAs/GaSb SLS structure as a one single entity and as an amalgamation of its constituents InAs and GaSb. These three experiments concluded that under the wet chemical etch of $HCl:H_2O_2:H_2O$ (1:1:4) solution InAs/GaSb SLS material behaved neither as InAs nor as GaSb individually. But under the BCl_3 based plasma dry etch its etch rate of 0.22μm/min was closer to GaSb (0.28μm/min) than InAs (0.13μm/min).These results are crucial as the 16ML InAs/0.8ML InSb/6ML GaSb system contained more InAs than GaSb.

2. Investigate, implement and compare various passivation techniques to InAs/GaSb SLS LWIR detectors by electrical characterization.

   (a) A comparative study of dielectric passivants (Silicon di-oxide and Silicon nitride) versus organic passivant of SU-8 versus chalcogenide passivants (Zinc Sulfide, Ammonium Sulfide and Electro-chemical passivation i.e. deposition of pure sulphur) were carried out on InAs/GaSb SLS LWIR single-pixel detectors with pin architecture. At 77K and applied bias of -0.1V, electro-chemical passivation electro-chemical passivation showed the most improved dark current density (J_d) of 0.09A/cm^2 and highest surface resistivity of 1500Ω-cm over unpassivated detector [89].

   (b) Then, ammonium sulfide and electro-chemical passivation (ECP) were performed on InAs/GaSb SLS LWIR detectors with pBiBn architectures. At 77K and applied bias of -0.1V, ECP improved the J_d by a factor of 54 in when compared to unpassivated devices [89].

   (c) We then studied the long term stability of ECP on InAs/GaSb SLS LWIR single-pixel detectors with pin architecture. We found that ECP had degraded over time with J_d being 0.09A/cm^2 right after passivation and 2.18A/cm^2 after 4 weeks of passivation [89].

(d) In the next study, we compared all the sulphur-based passivants of acid based thioacetamide, base-based thioacetamide, Ammonium Sulfide and Electro-chemical passivation (ECP) on graded-bandgap design based LWIR SLS detectors. Here ECP showed most superior performance of all with the highest surface resistivity of 1.4x10^5 Ω-cm at 77K [88].

(e) Due to the long-term instability of ECP, we proposed and implemented the novel chlorine-doped Zinc Telluride (ZnTe:Cl) passivation technique on InAs/GaSb SLS LWIR single-pixel detectors with pin and graded-bandgap architectures. It is for the first time that ZnTe:Cl has been utilized as a passivation technique on any IR device system. ZnTe was chosen a passivation material for InAs/GaSb SLS material system due to its material properties such as (i) lattice constant of ZnTe=6.1034Å which is lattice matched to GaSb and close to InAs and AlSb, (ii) ZnTe is epitaxially grown by MBE system, ensuring uniform deposition, and robust, high quality material with minimal defects (iii) most crucially, ZnTe being in the chalcogenide family, is expected to mimic the very effective sulphide properties, as a passivant. Though ECP showed a superior surface resistivity ($r_{surface}$) of 10^5Ω-cm over ZnTe:Cl passivation with $r_{surface}$ =6700Ω-cm, ZnTe:Cl passivation had almost no degradation over time. Hence an improved ZnTe:Cl passivation with its robust, uniform passivation layer has the potential to replace ECP in FPA fabrication on InAs/GaSb SLS LWIR detectors and advance the Type-II SLS based detector technology to commercialization.

1.6 Conclusions

In this chapter we have introduced in brief, the physics behind IR radiation, the workings of thermal and photon IR detectors, and evolution of present day IR detectors. We then dwelled into the concept of InAs/GaSb based Type-II SLS detectors, their advantages and limitations. We then established the need for surface study and surface modification in InAs/GaSb based Type-II SLS LWIR detectors. Then, a brief outline of this dissertation is laid-out that describes the work contained within the next few pages. This chapter is concluded with the summary of all crucial contributions achieved during the course of this dissertation in understanding the workings of device surfaces of InAs/GaSb based Type-II SLS LWIR detectors.

Chapter 2

Materials and Methods

During the past 30 years of evolution of the type-II SLS based detectors, several material compositions and device architectures have been proposed. More recently, bandgap engineered structures such as pBiBn [39], nBn [108], M-structure [74], W-structure [6, 124] and CBIRD [123] architectures have all been demonstrated. These new SLS devices credit their improved performance over the established p-i-n architecture, to the reduction in dark currents due to the presence of current blocking layers that reduce one or more dark current components. In the first part of this chapter, we will briefly look at various type-II SLS material systems that we implemented for the purpose of our experiments.

In this dissertation a variety of characterization techniques were utilized to characterize as-grown and fabricated (including passivation) materials. The structural properties of as-grown material were determined by high resolution X-ray diffraction (HRXRD) measurements. The surface morphology of the as-grown, etched, and passivated materials was evaluated by atomic force microscopy (AFM). Exposed detector sidewalls were imaged through scanning electronic microscopy (SEM) technique. The electrical behavior of fabricated detectors was investigated by current-voltage (I-V) measurements. The same measurements were used to evaluate effectiveness of passivating layers. Detector performance also was characterized by spectral response and responsivity measurements.

2.1 Materials

In this section, brief descriptions of the three SLS architectures utilized in this dissertation is presented.

2.1.1 p-i-n architecture

The first InAs/GaSb type-II SLS structure that we implemented in our research study is termed as the ``p-i-n architecture ˝. This SLS structure recreates the classic p-i-n photodiode design as seen in Figure. 2.1. Photodiodes specifically photovoltaic detectors (PV) are manufactured by creating p-n junctions in a semiconductor and it is sensitive to incoming optical stimuli, producing a voltage or current output proportional to the incident light intensity. A photodiode that has a built-in depletion region with the inclusion of an intrinsic layer (i-region) between the p and n regions is called a p-i-n photodiode [28]. Due to the very low density of free carriers in i-region and hence its higher resistivity than doped p or n regions, any applied bias drops entirely across the i-layer, which is fully depleted of carriers at 0V or very low values of reverse applied bias [17]. In order to collect all photo-generated (electron-hole pairs) carriers, the p-i-n diode has a `controlled ´depletion width (W). The thickness of the intrinsic layer and hence depletion width W can be tailored to optimize the spectral response, frequency response and quantum efficiency of the photodiode.

In Fig. 2.2, schematic of a p-i-n photodiode is described along with the corre-

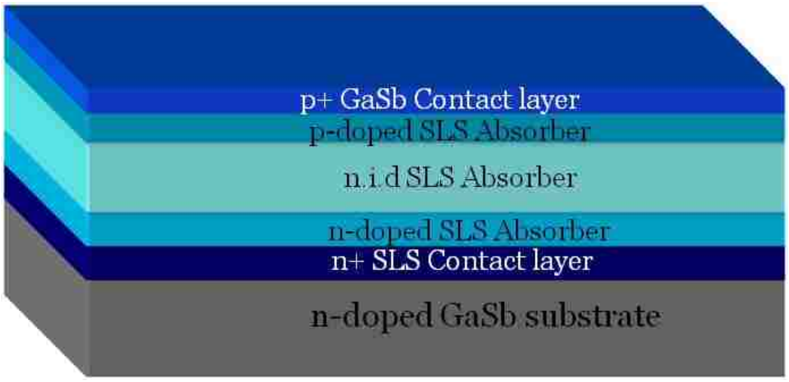

Figure 2.1: Schematic of a InAs/GaSb type-II SLS LWIR detector structure with p-i-n design.

sponding energy-level diagram that depicts the depletion width and the absorption and carrier generation processes. Since the applied bias drops across the entire i-region, any appreciable reverse-bias voltage will cause drift current (I_{dr}) to dominate in this region. Similarly, the lack of an electric field in p or n regions caused diffusion current (I_{diff}) to dominate there. Photo-generated carriers move by drift and diffusion, hence the total current density through a reverse-biased depletion layer is:

$$I = I_{dr} + I_{diff} \tag{2.1}$$

In this structure, p-layer is made thin so that the photo-generated carriers will not have to rely on the slower diffusion currents to carry them to the intrinsic region. Under this condition, the total photocurrent is given by:

$$i = (1 - \varkappa)\phi_0 q(1 - e^{-aW}/(1 + aL_h)) \tag{2.2}$$

Where $\varkappa$ is the Fresnel reflectance, a is the absorption co-efficient, L_h is the diffusion length of holes, W is the depletion width and ϕ_0 is the incident flux.

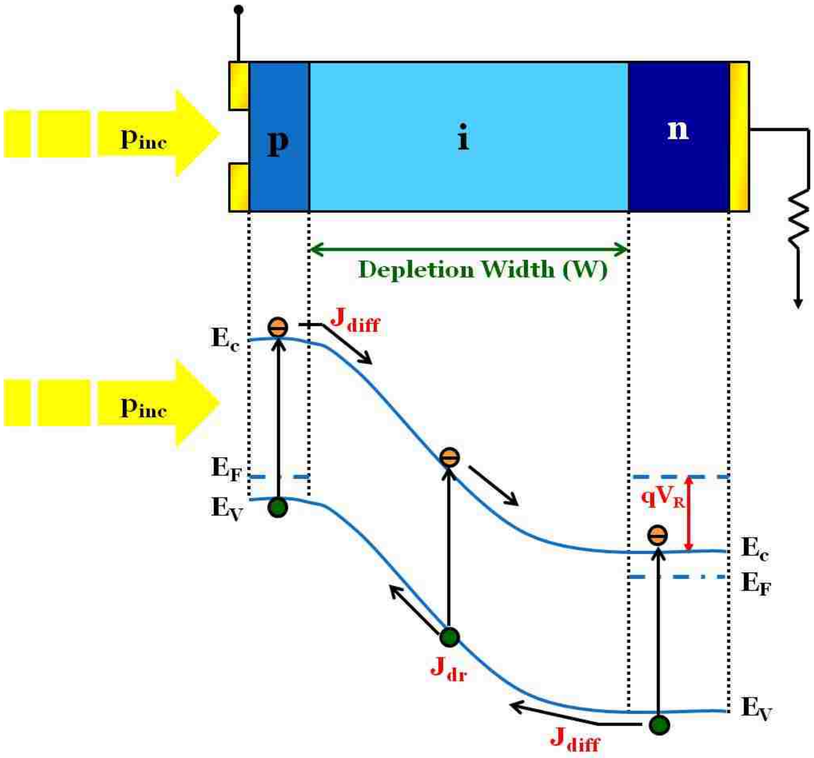

Figure 2.2: Schematic of a p-i-n design and corresponding energy-level diagram depicting the depletion width.

A conventional LWIR SLS pin detector structures (schematic of detector heterostructure shown in Figure.2.1) investigated in this presented work are grown on n-type (Te-doped) GaSb (100) epi-ready substrates by molecular beam epitaxy (MBE). The LWIR detector structure consists of ˜2.1 μm thick absorbing region formed by 16 ML InAs/0.8 ML InSb/6 ML GaSb SLS grown on the top of ˜0. 45 μm thick SLS bottom contact n-region (4x10^{18} cm^{-3}) formed by SLS with the same composition and thickness. Finally, the structure is capped by a 50 nm thick GaSb p-type layer (4 x 10^{18} cm^{-3}). It has to be noted that the gradient absorber composes of both top and bottom 50 periods of absorber being doped p- and n-type, respectively, with doping concentration of 1 x 10^{17} cm^{3}.

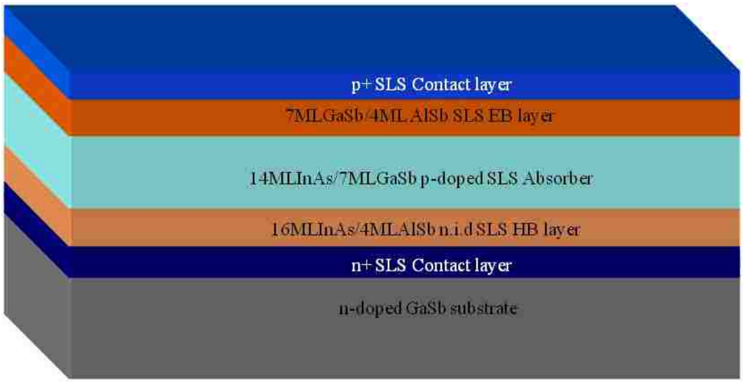

Figure 2.3: Schematic of a InAs/GaSb type-II SLS LWIR detector structure with pBiBn design.

2.1.2 p-B-i-B-n architecture

Early generations of LWIR SLS detectors with p-i-n design, were notorious for their very high dark currents and hence their incompatibility in large array FPA fabrication. One of the heterojunctions implemented to overcome these disadvantages in the InAs/GaSb based type-II SLS structure with pBiBn design [39]. This design is an evolution of the p-i-n design, where in addition to the p-i-n layers, barriers for blocking electrons called electron barrier (EB) and similarly hole barrier (HB) are implemented.

The Fig 2.3 shows a schematic of pBiBn design and Fig 2.4 shows the band-diagram of a pBiBn structure depicting the working of the carrier blocking mechanism. The EB layer that is grown between p-contact SLS layer and the SLS absorber layer blocks the minority carrier (electrons) diffusion from the p-contact layer to the absorber region. Similarly, the HB layer that is present between the n-contact SLS layer and absorber layer blocks minority carrier (holes) diffusion from the n-contact layer to the absorber region. This mechanism hence reduces the dark current in this system. Due to the large amount of electric field drop across the

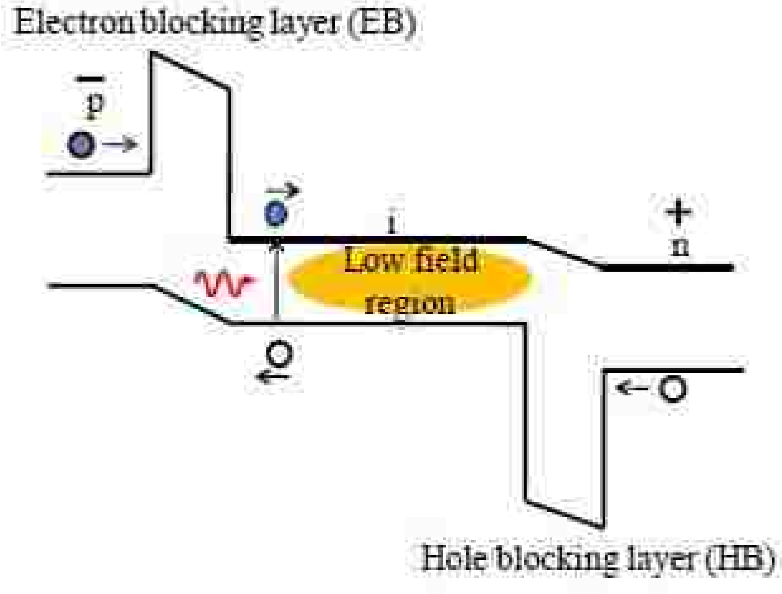

Figure 2.4: Schematic of operation of InAs/GaSb type-II SLS LWIR detector structure with pBiBn design under reverse bias. Re-printed from [39].

EB and HB layer which are constituted of a wider-bandgap material than the absorber region, the field across the active region in this device is smaller than in a p-i-n system. The reduction in electric field results in smaller depletion region and hence leads to reduced Shockley Read-Hall (SRH) recombination centers and reduced tunneling currents which imply reduced dark current in the detector.

As seen in Fig 2.3, the pBiBn system utilized in this research work had 630 nm thick (90 periods)14 ML InAs/9 ML GaSb SLS p-type contact layer doped with Be (p = 2.8 x 10^{18} cm^3) followed by non- intentionally doped (n.i.d.) electron blocking (EB) layer consisting of 295 nm thick 6 ML InAs/10 ML GaSb SLS (60 periods). Then a 1.8 μm thick (312 periods) n.i.d absorber region of 13 ML InAs/6 ML In0.15Ga0.85Sb GaSb SLS was grown. Next, n.i.d 255 nm (40 periods) thick hole blocking (HB) layer made of 17 ML InAs/4 ML AlSb SLS was deposited and 100 nm (15 periods) thick n-type contact layer made of 16 ML InAs/7 ML GaSb doped with Te (n = 3 x 10^{18} cm^3) completed the structure. In both p-i-n design and pBiBn design detector structures, SLSs were grown with imposed InSb interfaces in order to balance strain. It is shown by Gautam et al [39] the typical operating voltage of pBiBn detectors is 50-250 mV (negative bias) and the pBiBn detector structures showed a dark current improvement of two orders of magnitude more than the p-i-n design.

2.1.3 Graded-gap `W´-structured superlattices (GGW)

The third design of detector heterostructure utilized in our work is the graded-bandgap W-design SLS proposed by Aifer et al [6]. In order to suppress tunneling and generation-recombination currents, Vurgaftman et al [124] utilized transition regions composed of W-structured type-II superlattices (WSLs) [69] to grade the bandgap in the depletion region. These WSLs [7] contain barriers that confine the electron wave-functions symmetrically about a hole-well, thereby increasing the electron-hole overlap while nearly localizing the wav-functions. The resulting quasi-2-D densities of states result in strong absorption near the band-edge in the WSL. Now to form a graded-gap WSL (GGW) photodiode structure, a series of WSLs with incrementally increasing bandgaps are grown which enlarges the bandgap at the vicinity of the junction to improvement by a factor of three over the IR-absorbing layer. This concept is made clearer in Fig 2.5 which shows the simulated band structure of the graded-gap and uniform-gap structures. The authors report 10-100 times lower dark current in GGW compared to uniform-gap structure as shown in Fig 2.6, due to the significant increase of the band-to-band tunneling barrier and lowering of intrinsic carrier density in the vicinity of the junction in the GGW structure.

The GGW detector material used in this study was grown by solid source

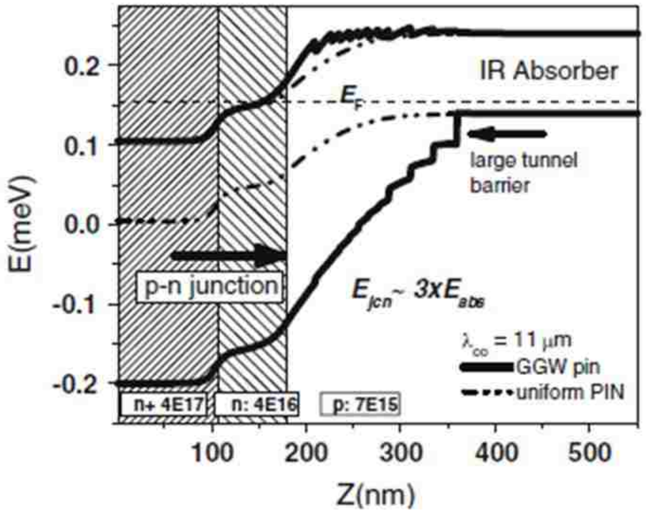

Figure 2.5: Simulated band profiles comparing the graded-gap (solid line) p-i-n photodiode and uniform-gap (dot-dash line) p-i-n photodiode. Re-printed from [6].

MBE on n-type (Te-doped) epi-ready (100) GaSb substrate at Intelligent Epitaxy Technology, Inc. (IntelliEPI). The grading steps (W-SLS) were formed by InAs/GaInSb/InAs/AlGaInSb period structure, with various composition and thickness of barrier, electron and hole wells. The band gap of such n-on-p structure is increased in a series of steps from that of the lightly p-type IR-absorbing region to a value typically two to three times larger. Absorbing region with total thickness of 4μm formed by p-type InGaSb/InAs SLS (p = 4 x 10^{15} cm^{-3}) was surrounded by n and p-type contacts composed of InAs (n = 4 x 10^{17}cm^{-3}) and GaSb (p = 3 x 10^{18} cm^{-3}), respectively.

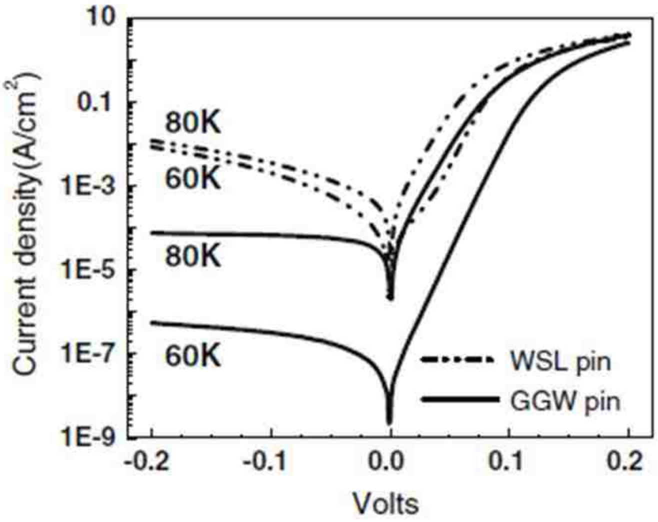

Figure 2.6: Current density (in A/cm^2) vs bias (in volts) graph at 60K and 80K comparing the graded-gap (solid line) p-i-n photodiode and uniform-gap (dot-dash line) p-i-n photodiode. Re-printed from [6].

2.2 Material Characterization

In this following section we will look at the study of the chemical state of a solid material by two points of view:

1. **Bulk Material characterization** that indicates the material quality before device fabrication. The techniques deployed for the study of structural properties of as-grown material were high resolution X-ray diffraction (HRXRD) measurements which looked at the structural composition of as-grown SLS structures, and Transmission Electron Microscopy (TEM) measurements that imaged the cross-sectional features of our structures.

2. **Surface Material characterization** that depicts the surface morphology of as-grown, etched, and passivated materials. Some of the tools employed for

surface study were atomic force microscopy (AFM) which looked at the as-grown and etched devices, scanning electronic microscopy (SEM) technique that imaged fabricated detector structures and exposed detector sidewalls, Energy Dispersive X-Ray spectroscopy (EDX), Auger electron spectroscopy (AES), and X-ray Photon Spectroscopy (XPS) were implemented to study the chemical composition of passivants and their interfaces with InAs/GaSb SLS structure.

2.2.1 High Resolution X-ray diffraction (HRXRD) Measurements

HRXRD is a non-destructive technique for the structural characterization of thin crystalline films. X-rays interact with electrons in matter and are scattered in various directions by the atomic electrons. If distances comparable to the wavelength of the X-rays separate the scattering centers then interference between the X-rays scattered from particular electron centers can occur. For an ordered array of scattering centers this can give rise to interference maxima and minima.

In order to observe x-ray diffraction from a crystalline lattice, the Bragg condition must be satisfied (2.3). The Bragg condition depends on the angle of the incident x-ray beam as it enters the crystal lattice and the direction at which the diffracted beam exits the lattice. It is met only when the scattered waves from all the atoms in the lattice are in phase, and interfere constructively.

$$2d_{hkl} \cdot sin\Theta = n\lambda \tag{2.3}$$

here d_{hkl} is the distance between the atom planes (h,k,l are the Miller indices), Θ is the incident angle, n is the order of diffraction and λ is X-ray wavelength.

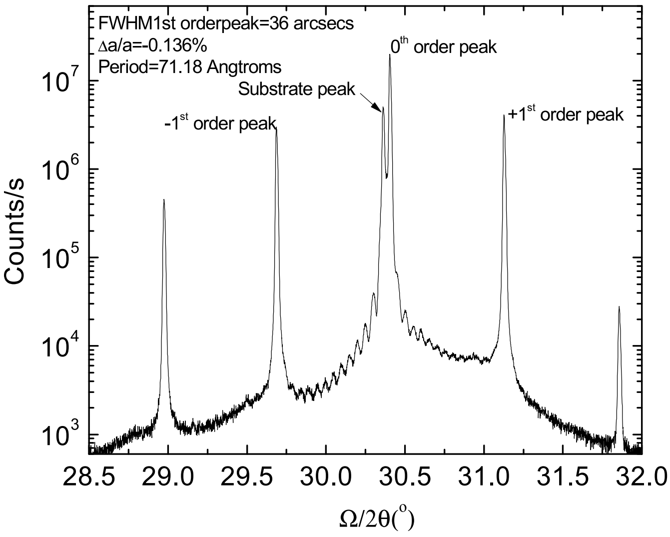

Figure 2.7: Typical HRXRD spectrum of a LWIR SLS detector, showing calculated lattice mismatch, FWHM of first order SLS satellite peak, and period thickness.

HRXRD scans in this work were performed with a Philips double-crystal X-ray diffractometer using the $Cu - K_{\alpha 1}$ line. The typical XRD spectrum from InAs/GaSb SLS is presented in Figure 2.7.

Parameters, which can be extracted from this spectrum, are:

- Lattice constant of substrate and average lattice constant of SLS

  Using equation(2.3) the lattice constant of substrate can be calculated for the symmetrical (004) X-ray scan:

  $$a = \frac{2n\lambda}{sin\theta} \tag{2.4}$$

  here n is equal to one, λ is known and equal to 1.5406Å, angle θ can be determined directly from the XRD spectrum. The average lattice constant of superlattice can be estimated using the same equation (2.4) with angle θ corresponding to the zero-order peak of the superlattice.

- Strain relation between substrate and epilayer

  Lattice mismatch between substrate and epilayer can be estimated as

  $$\frac{\Delta a}{a_s} = \frac{a_e - a_s}{a_s} = \frac{sin\Theta_e - sin\Theta_s}{sin\Theta_s} \tag{2.5}$$

  here a_s ($sin\Theta_s$) and a_e ($sin\Theta_e$) correspond to the lattice constants of substrate and zero-order peak of SL, respectively.

- Thickness of SLS period

  The separation between the +1 and -1 order superlattice peaks, expressed in arc-seconds, can be analyzed with an automated algorithm to determine the SLS period thickness. In this work we used the algorithm based on the dynamical theory of diffraction (Bede RADs software).

- Full Width at Half Maximum (FWHM) of SLS Satellite Peaks

  This is good qualitative measure of structure's crystalline quality. Narrow and symmetrical SLS peaks with FWHM in order of 18-25 arcsec indicate perfectly ordered structure with compositionally abrupt interfaces. On the contrary, broad and asymmetrical satellite peaks (FWHM of 55-65 arcsec) indicate variation of period thickness and growth defects accumulating at the interfaces of SLS. Typically, FWHM for the first satellite peak of SLS is calculated.

2.2.2 Transmission Electron Microscopy (TEM)

Transmission Electron Microscopy (TEM) is an analytical technique for structural determination and it is based on the diffraction of electrons when they pass through a very thin sample [48]. A image is formed from the interaction of the electrons transmitted through the sample, then image is magnified and projected on to an fluorescent screen or a CCD camera and this is what we see. The sample preparation is generally destructive as generally the sample has to be thinned down to a thickness of a few thousand angstroms by chemical etching or ion-milling. The TEM instrument set-up usually consists of an emission source (Tungsten filament or LaB6 source), and this electron gun is connected to a high voltage (~100-300kV) source. When the gun is supplied with required amount of current, it emits electrons by field electron emission or thermionic emission into the vacuum chamber. Next set of mechanisms in the instrument (top down) are the optical lenses in the TEM that facilitate for beam convergence utilizing the angle of convergence as a variable parameter. This gives the TEM its unique ability to change magnification by simply modifying the amount of current that flows through the coil, hexapole or quadrupole lenses. Lastly, the display setting usually consists of phosphor screen (10-100μm thickness) that allows the operator to view images directly. Also available in most machines are image recording systems like CCDs.

In our research, we have used the JEOL 2010 200kV high resolution transmission electron microscope (HRTEM) instrument (shown in Fig 2.8) with Point-to-Point Resolution = 0.194 nm, Minimum Spot Size = 0.5 nm and housed at the Earth and Planetary Sciences department at UNM. The sample preparation and TEM images we taken by Dr. Ying Bing and Dr. Elena Debrova. Cross-sectional TEM image of SLS in Fig. 1.4 were imaged by Evans Analytical Group. The cross-sectional TEM images show the planarity of interface and the structure of various reacted layers and hence a crucial tool in analyzing our MBE grown structure.

2.2.3 Atomic Force Microscopy (AFM) Measurements

Atomic force microscopy (AFM) is a surface imaging technique, providing the topographic information of the surface with nanometer resolution. An AFM unit

Figure 2.8: Photograph of JEOL 2010 200kV high resolution transmission electron microscope (HRTEM) instrument.

is mainly composed of a laser diode, a flexible cantilever, a piezoelectric motor, and a position-sensitive photodetector. AFM is designed on the basis of the atomic force between the tip and sample surface. A sharp tip is mounted on a flexible cantilever, a few angstroms away from the sample surface. The repulsive Van der Waals force between the tip and the surface causes the cantilever to deflect. The motion of the cantilever is magnified by a laser beam reflection and recorded as the vertical displacement of the tip. In this way, the surface topography can be imaged by scanning the tip over the sample surface. AFM is typically operated in one of the two basic modes: contact mode or tapping mode. Contact mode is a fast and convenient way of imaging a relatively hard surface, but the drawback for this mode is that there are large lateral forces on the sample as the tip is ”dragged” over the surface. In tapping mode, on the other hand, the cantilever is oscillated at or near its resonant frequency (often hundreds of kilohertz), and the tip gently taps the surface with a significantly reduced contact time. Tapping mode is thus extremely useful for topographical imaging of soft samples.

2.2.4 Scanning electron microscope (SEM)

SEM is a type of electron microscope that produces images of a sample by scanning it with a focused beam of electrons. The electrons interact with electrons in the sample, producing various signals that can be detected and that contain information about the sample's surface topography and composition. The electron beam is generally scanned in a raster scan pattern, and the beam's position is combined with the detected signal to produce an image. We performed SEM measurements with the JSM6400 field emission scanning electron microscope (FESEM) and the instrument is shown in Fig 2.9. This is an analytical grade SEM utilizing a field emission source (tungsten cold cathode design). Accelerating voltages range between 0.5 to 30kV. The magnification ranges between 10 - 500,000 times at 39 mm working distance. Resolution is approximately 1.5 nanometers at 30kV and 8mm working distance. The SEM images presented in this work we taken by Dr. S. Smolev, Dr. Mikhail Naydenkov, Dr. Yagya Sharma, Dr. Stephen Myers and Dr. Ashwin Rishinaramangalam.

2.2.5 Energy Dispersive X-Ray spectroscopy (EDX) Measurements

Energy Dispersive X-Ray spectroscopy (EDX/EDS) is an analytical tool found on most Scanning Electron Microscopy (SEM) instruments that is used for chemical or elemental analysis of a specimen. This tool operates under the assumption that each element has its own unique atomic make-up and hence this allows the X-rays which are a distinguishing feature of an elements atomic structure, too would be unique to the element and hence identifiable.

In order to stimulate the emission of X-ray from the sample, a high-energy beam

Figure 2.9: Photograph of JSM 6400 field emission scanning electron microscope (FESEM) instrument.

of charged particles such as electrons or protons or a beam of X-rays is directed on the material. Fig. 2.10 shows the schematic of a photoemission process. The incident beam can excite an electron from the inner shell of the atom, creating an electron hole and ejecting the excited electron. Then an electron from an outer, higher energy shell fills this hole. It is the difference in energy between the higher energy shell and lower energy shell that is released as an X-ray. The energy-dispersive spectrometer can measure the energy and number of X-rays emitted from the sample.

During the emission of X-rays from the sample as it stops the streaming electron beam, the ``balloon-shaped″primary volume of excitation (i.e. the Brehmsstrahlung sphere volume) within the sample expands with increasing the energy of the e-beam by higher voltages applied on the cathode source. The size of the primary volume of excitation varies from 0.5 to 3m in diameter as well as in depth within the sample. Since the X-rays are emitted as a result of the loss

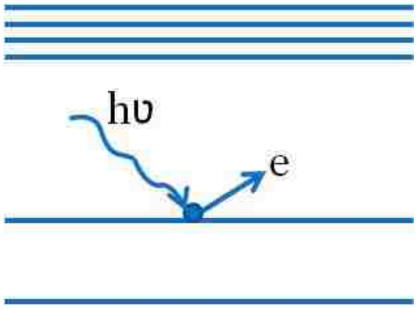

Figure 2.10: Schematic Diagram of photo-emission process. Redrawn from Ref [97].

of kinetic energy of the electron beam at this ``expanding volume-element˝, the differences in the EDX peak intensities for the constituent chemical elements point to compositional heterogeneity between the near-exterior (sub-surface) region as compared to the deeper regions of the specimen(SLS). It must be noted that the EDX spectrum presented in this work is plotted with X-ray energy (in keV) on the X-axis and the intensity (in counts) on the Y-axis.

For the purpose of our measurements we used the JEOL 5800LV SEM, equipped with an Oxford Analytical ultrathin-window EDS and an Oxford Isis 300 X-ray analyzer attached to the microscope. It must be noted that we used automated analyses feature on tool and its analytical software provides semi- to fully quantitative EDS analysis down to boron. The EDX measurements presented in this work we carried-out by Dr. Mikhail Naydenkov.

2.2.6 Auger Electron Spectroscopy (AES) measurements

The three spectroscopic techniques of EDX, XPS and AES that are described in these sections are closely related mechanisms. Auger Electron Spectroscopy (AES) is one of the most widely used surface analytical tool over the last 40years. AES can be

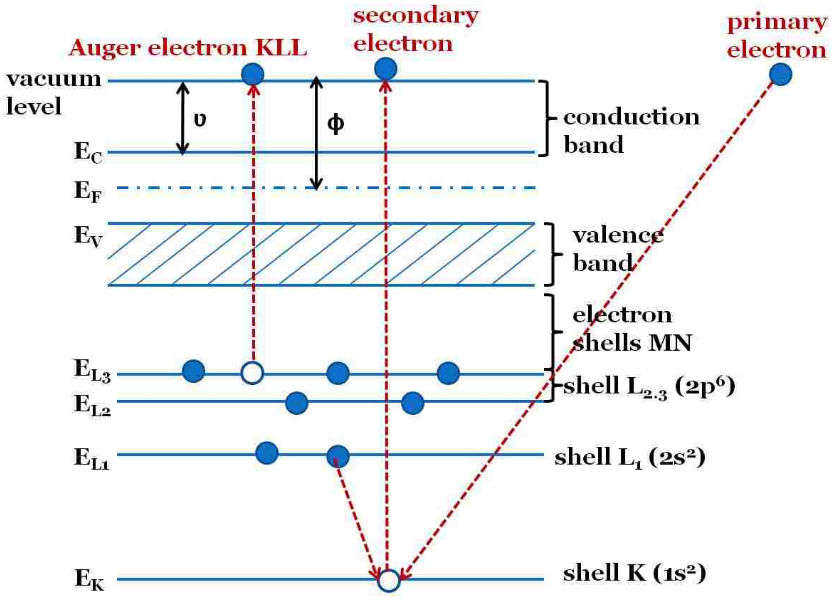

Figure 2.11: Schematic illustration of Auger electron generation process for the transitions KLL. Redrawn from Ref [48].

implemented for qualitative and semi-quantitative determination of composition near-surface region, along with chemical-state and structural information. The guiding principle of this spectroscopic technique is the Auger Effect and is based on the analysis of electrons emitted from an excited atom after a series of internally occurring relaxation steps.

In an atom, the Auger process occurs from the decay of a core-level hole created due to the interaction of energetic photons or electrons or ions with an electron in the core level. The decay of this hole takes place through a many-body process in which an electron from shallower level fills the core-level hole, causing the emission of either an Auger electron by transfer of excess kinetic energy to a third electron (as shown in Fig 2.11) or a photon (fluorescence process shown in Fig 2.12) [97].

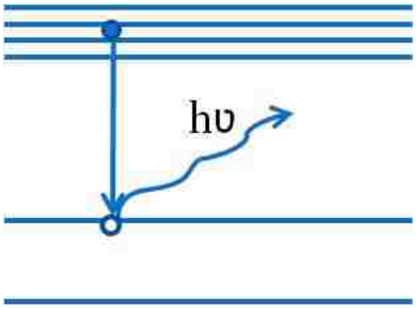

Figure 2.12: Schematic diagram of fluorescence process. Redrawn from Ref [97].

In Auger electron spectroscopy (AES), the specimen is irradiated by a focused beam of electrons with energy range of 2-20keV. Then atoms at an inner core level e.g. the K-level (as seen in Fig 2.11) get ionized. Subsequently, de-excited by an electron falling from a higher level L1, whose energy balance is being removed by a third electron from level L3. The last electron is the Auger electron and is emitted with an energy E_{Auger} which is defined as:

$$E_{Auger} = E_K(Z) - E_{L_1}(Z) - E_{L_2}(Z + \Delta) - \Phi \tag{2.6}$$

Where Z is the atomic number of the element, Φ is the work function of the surface and component Δ (experimentally between 1/(2 to 3/2)) takes into account the fact that the atom is in a charged state when the final electron is ejected. The AES measurements presented in this work we carried-out by Evans Analytical Group.

2.2.7 X-ray Photon Spectroscopy (XPS) measurements

X-ray Photon Spectroscopy (XPS) is a photoemission technique utilized to examine the compositional and chemical state distribution of species at surfaces of solids. The principle is that when a solid material is irradiated, it absorbs discrete quanta of energy resulting in direct emission of electrons, and kinetic energy distribution of the emitted electrons provides detailed information about that solid. In XPS, the kinetic energies of the emitted electrons forming the spectral peaks are measured using an electrostatic charged-particle energy analyzer or hemispherical analyzer (HSA). The schematic of a XPS instrument is shown in Fig.2.13. The binding energies of these electrons can be calculated using the following equation:

$$E_b = h\upsilon - E_k + \Delta\Phi \tag{2.7}$$

Where E$_b$ is the electron binding energy (BE), h$\upsilon$is the energy of the incident photon; E$_k$ is the kinetic energy (KE) and $\Delta\Phi$ is the difference in work-functions between the sample and the detector material i.e. assuming there is no electrical charging at the sample surface. Fig. 2.10 shows the schematic of a photoemission process.

The XPS measurements performed as a part of this research project were carried out in a commercial Thermo K-alpha system equipped with a monochromatic Al Kα source, a hemispherical electron energy analyzer, and a magnetic electron lens. The penetration depth of this XPS system is ~5nm with the nominal spot size and analyzer field of view to be 0.5mm^2. It has to be noted that the scans for Ga 2p, Sb 3d, In 3d and As 2p regions were obtained by high-resolution normal emission angle-integrated scans. These room temperature measurements were carried in an ultra-high vacuum (UHV) chamber with base pressure at Torr. The XPS measurements presented in this work were carried-out by Dr. Kateryna Artyushkova.

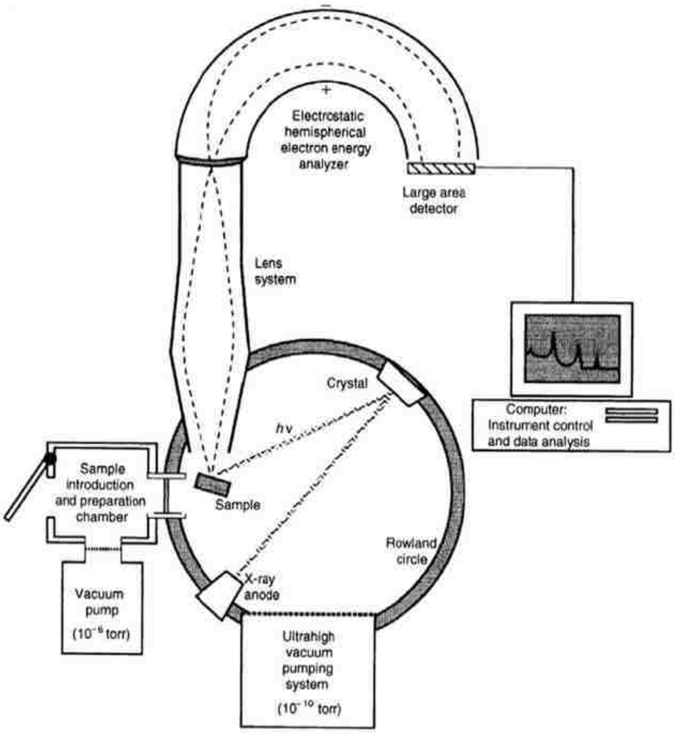

Figure 2.13: Schematic of XPS/ ESCA spectrometer. Reprinted from Ref [97].

2.3 Device Characterization

The electrical behavior of fabricated detectors was investigated by current-voltage (I-V) measurements. The same measurements were used to evaluate effectiveness of passivating layers. Detector performance also was characterized by spectral response and responsivity measurements. In this section, various detector characteristics and figures of merit, such as spectral response, dark current, resistance-area product, surface resistivity, responsivity, and detectivity are discussed.

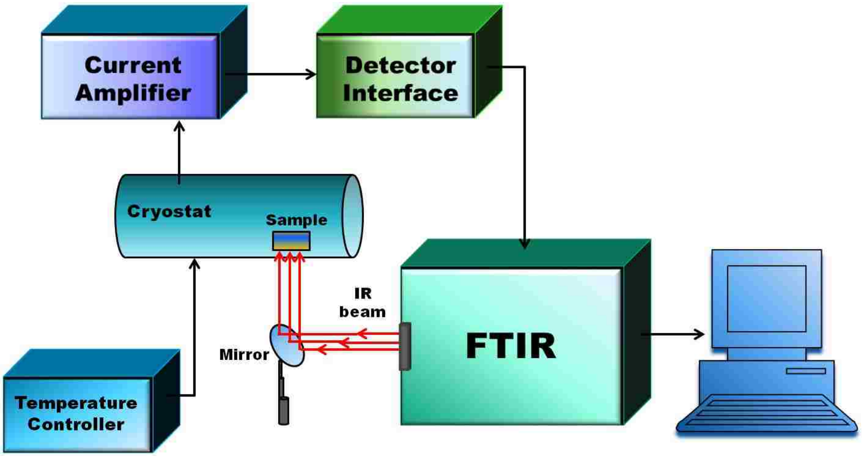

Figure 2.14: Schematic for the spectral response setup.

2.3.1 Spectral Response

Spectral response or photocurrent spectrum of a fabricated detector is measured using a Nicolet 670 Fourier transform infrared spectrometer (FTIR) which is equipped with a broadband infrared glowbar source. The instrument is software controlled and values of different parameters such as resolution and velocity of the scanning mirror of the FTIR can be selected by the user. The spectrum can be corrected for the background in the software and should be corrected with respect to the detector response as well. Spectral response gives the cutoff wavelength of a detector as well as the relative quantum efficiency (QE) at different wavelengths. The experimental set up for the spectral response measurements is schematically shown in the Figure 2.14

2.3.2 Dark Current Measurements

The current that flows through the detectors in the absence of any photon flux is called the dark current. Dark current is a very important figure of merit, since it determines the maximum operating temperature for the detector for a given signal-to-noise ratio (SNR). In SLS detectors, the dark current may be divided into two major components, bulk and surface currents. Bulk component of dark current includes minority carrier diffusion current, generation-recombination current (G-R, or Schockley-Read-Hall, current), tunneling (trap assisted and band to band) currents. Surface current is caused by surface states and also referred as surface leakage current. The performance improvement in a SLS detector is carried out by reducing the dark current without affecting the photocurrent.

The effectiveness of passivation is commonly evaluated using variable area diode array (VADA) method [42]. Fig. 2.15 shows the schematic of the arrangement of VADA diodes in our mask set and it indicated the difference between conventional detector diode configuration and that of VADA diode. For the square mesa diode, the dark current density can be expressed as the summation of bulk component of dark current and the surface leakage current. If the bulk current dominates the detector performance, then the curve will have a slope close to zero. If the surface leakage is significant, then an increase in the dark current density will be observed for smaller devices. In other words, the surface dependence of inverse of the dynamic resistance area product at zero bias R_0A of passivated diode can be approximated as

$$\frac{1}{R_0A} = \frac{1}{R_0A}_{Bulk} + \frac{1}{r_{surface}}\frac{P}{A} \tag{2.8}$$

where R_0A_{Bulk} is the bulk R_0A contribution ($\Omega \cdot cm^2$); $r_{surface}$ is the surface re-

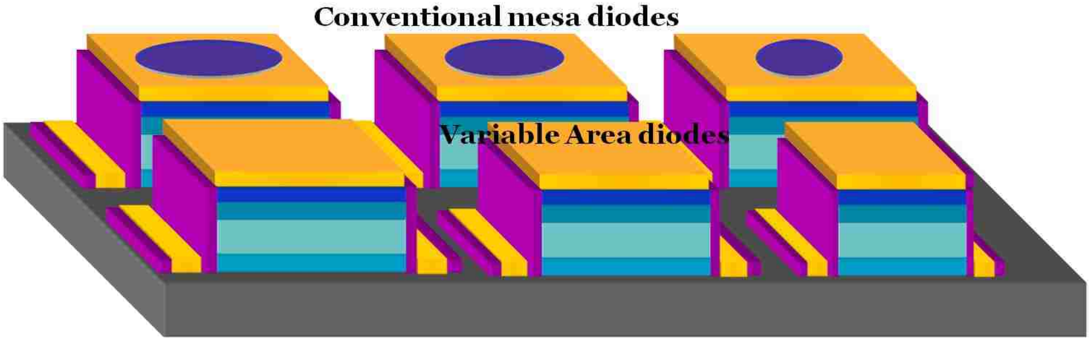

Figure 2.15: Schematic of our mask set showing conventional diodes and Variable area diodes (VADA).

sistivity ($\Omega \cdot$ cm); P is the diodes perimeter and A is the diodes area. The slope of the function given by equation (2.8) is directly proportional to the surface-dependent leakage current of the diode. Higher values of surface resistivity indicate weaker dependence of the diode's characteristics on the surface effects. Figure 2.16 schematically illustrates the ($\frac{1}{R_0 A}$) vs ($\frac{P}{A}$) dependence for the diode with ideal and non-ideal passivations.

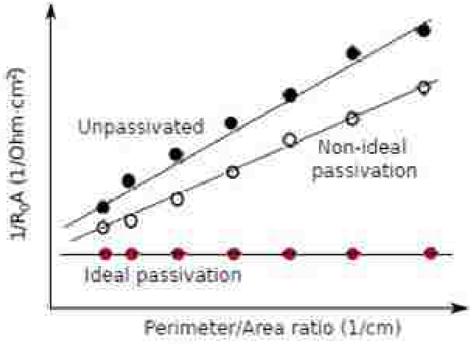

Figure 2.16: Dependence of the dynamic resistance-area product at zero bias vs. perimeter-to-area ratio for VADA diodes with ideal and non-ideal passivations.

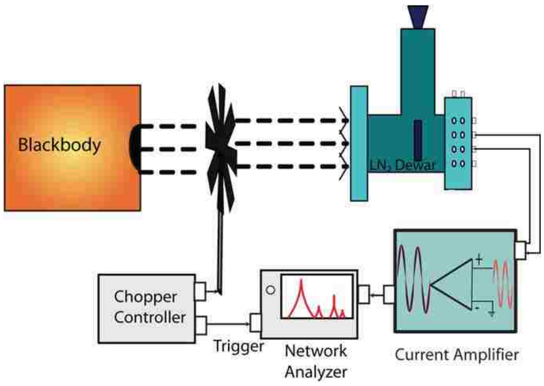

Figure 2.17: Measurement set-up for responsivity calculations.

2.3.3 Responsivity

Responsivity is defined as the amount of photocurrent flowing through the external circuit per watt of optical power incident on the detector. It is typically measured with a calibrated blackbody source radiating photons in the detector response range, which can be calculated by using Planck's law (eqn. 1.1). The measurement set-up for responsivity measurements is described by the block diagram in Fig 2.17. Using basic radiometric calculations, the number of photons falling on the detector per second can be calculated for the given parameters such as blackbody temperature, aperture size, distance from the detector, detector optical area and the wavelength range of interest.

To calculate responsivity of SLS detector, blackbody-to-peak conversion factor has to be defined first:

$$C = \frac{\int_0^x M(\lambda,T)d\lambda}{\int_0^x R(\lambda)M(\lambda,T)d\lambda} = \frac{M_{BB}}{M_{effective}} \tag{2.9}$$

Where $M(\lambda,T)$ is the spectral excitance for black body (BB) at given BB temperature, $\frac{W}{cm^2\mu m}$; $R(\lambda)$ is the relative responsivity $M_{effective}$ and M_{BB} is the effective excitance and excitance from the blackbody respectively.

Since temperature of BB is known, spectral excitance from BB can be calculated using Planck's equation

$$M(\lambda, T) = \frac{c_1}{\lambda^5(e^{\frac{\frac{hc}{k}}{\lambda T}} - 1)} \tag{2.10}$$

Then the peak responsivity for the SLS detector is calculated as

$$R_{peak} = R_{BB} \times C \tag{2.11}$$

here R_{BB} is the responsivity measured using the total blackbody incidance.

To obtain the absolute spectral response values, the result of eq.(2.11) was multiplied by the relative spectral response curve obtained in section 2.3.1.

2.3.4 External Quantum Efficiency (QE)

The external quantum efficiency (QE or n_e) of a photodetector is defined as the number of carriers (electron-hole pairs) collected at the output divided by the number of incident photons [17][6]. It can be indicated as:

$$n_e = \frac{I_{ph}/q}{P_{inc}/hv} \tag{2.12}$$

where I_{ph} is the photocurrent generated by the electron-hole pairs and P_{inc} is the incident optical power. The QE is the number of independent electrons produced per photon and is normally expressed in percent. It takes into account reflectance, absorptance, scattering, and electron recombination [28]. From section 2.3.3, we know that responsivity = $\frac{I_{ph}}{P_{inc}}$. Hence, for photodiode absorption QE can be extracted from responsivity (R), using the following equation.

$$QE = R \times \frac{1.24}{\lambda} \times 100 \tag{2.13}$$

here R is in A/W, λ is in μm, and QE is in %. In the case of a photoconductor, which has an inherent photoconductive gain inside the device, the above formula needs to be modified, with the left hand side becoming conversion efficiency, which is a product of QE and photoconductive gain.

2.3.5 Specific Detectivity

Specific detectivity (D*) is a widely used figure of merit for describing the SNR of a detector, normalized with respect to the detector area (A$_d$) and measurement bandwidth (Δf). It is defined as

$$D^*(\lambda) = \frac{R(\lambda) \cdot \sqrt{A_d \cdot \Delta f}}{i_n} \tag{2.14}$$

where, i$_n$ is the root mean square (rms) noise current. For $\lambda = \lambda_{\ Peak}$, D$^*(\lambda)$ is referred to as peak-specific detectivity, expressed in units of 'Jones, which is often quoted as the figure of merit for a single-pixel detector.

2.4 Conclusions

In this chapter we briefly described the three different architectures of Type-II SLS LWIR detectors used during the course of this work namely, (i) p-i-n design, (ii) pBiBn design, and (iii) graded bandgap `W´structure. The second part of this chapter briefly introduces the working mechanisms of characterization techniques used in this work, namely (1) Material characterization such as HR-XRD, TEM, AFM, SEM, EDX, AES and XPS and (2) Electrical characterization explained the principles behind spectral response measurements, dark current densities, surface resistivities, responsivity measurements, quantum efficiency and specific detectivity calculations.

Chapter 3

Surface Effects

3.1 Introduction

It has been recognized from the earliest days of solid-state electronics that surfaces and interfaces play decisive roles in device performance. This is evident from the critical dependence of the first transistor (point-contact transistor) on the surface recombination velocity of germanium [100]. Researchers still look for a ``superior´´surface that is a very broad term which includes surface smoothness, contamination free, native oxide free surface, wherein surface Fermi level pinning is eliminated. ``Surface Passivation´´in general terms, is a technique of making the surface passive i.e. less or non-reactive. This treatment of the device surface also includes the decrease in the number of recombination centers on the surface. It has been earlier used in terms of metal surface wherein the metal surface was prevented from corroding by depositing passivants like oxides. Obtaining ideal surfaces through passivation techniques on GaAs has been in study as early as late 1980s [130, 114, 131]. The earliest investigation into passivation of GaSb was reported in 1990s [86, 63]. Along with the problems of surface Fermi level pinning and high surface state densities, GaSb-based devices also have to deal with a conductive native oxide layer on the surface. This chapter explains the nature of native oxides formed on sidewalls of GaSb-based devices, highlights the methods of native oxides thinning, and, finally, reviews various techniques developed for passivation of GaSb-based devices, in particular, InAs/GaSb SLS detectors.

3.2 Native Oxides

3.2.1 Native Oxide Formation

The performance of individual FPA pixels with typical mesa dimensions of ~20 μm x 20 μm is strongly dependent on surface effects due to their large surface/volume ratio. Presence of surface leakage currents may be explained using the surface potential theory. With a nonzero surface potential at the sidewall interface, band-bending occurs due to the Fermi level position and this results in accumulation/inversion of majority carriers that can then create conductive leakage channels parallel to the surface. The most important reasons for the nonzero surface potential are the abrupt termination of periodic crystalline lattice at the semiconductor-air interface with formation of unsatisfied (dangling) bonds and undulation effects presented on the device sidewalls due to differential etch rate of SLS constituent layers (InAs, GaSb, InSb, GaAs, and sometimes AlSb). In addition to the surface potential modification native oxides and contaminants also contribute to dark current by creating additional interfacial states. Interface states located within band-gap alleviate the carrier tunneling, inducing surface recombination and contributing to trap-assisted tunneling dark current.

The native oxides are readily generated on exposed SLS device sidewalls saturating the dangling bonds and forming a secondary compound. Since thicknesses of InAs and GaSb SLS constituent layers are in order of tenths of MLs, whereas thicknesses of interfacial InSb and GaAs layers is commonly assumed to be less than a monolayer (ML) [81, 119], the formation of native oxides on GaSb and InAs is detrimental to the SLS device performance [18, 9].

Analysis of ternary phase diagrams [115] (Fig. 3.1) for gallium (indium)-based group III-group V-oxygen systems predicts the multilayered composition of the oxide film for the GaSb and InAs due to thermal oxidation with oxygen or water vapor in the air.During the thermal oxidation of GaSb, the initial oxide layer is formed by breaking the bonds of the surface atoms of Ga and Sb. Then the diffused O2 atoms interact with both Ga and Sb to form non-equilibrium Ga_2O_3+SbO_3 on the surface (as follows):

$$2GaSb + 3O_2 \longrightarrow Ga_2O_3 + Sb_2O_3 \tag{3.1}$$

It has to be taken into account that Ga_2O_3 and elemental antimony Sb are the only stable phases that exist in thermodynamic equilibrium with GaSb. Ergo, any Sb_2O_3 formed (as seen in Eq.3.1 should react with GaSb to give rise to GaS_2O_3 and free Sb:

$$2GaSb + Sb_2O_3 \longrightarrow Ga_2O_3 + 4Sb \tag{3.2}$$

Also the above reaction (Eq. 3.2) occurs spontaneously (even at room temperature), hence a surface of GaSb when exposed to air will form a native oxide layer composing of Ga_2O_3 and elemental Sb. The oxidation of a GaSb surface can accordingly be summarized in a single reaction:

$$4GaSb + 3O_2 \longrightarrow 2Ga_2O_3 + 4Sb \tag{3.3}$$

Utilizing the similar argument, we can propose the thermal oxidation of InAs with O_2 or H_2O at room temperature can occur by the following two reactions:

$$2InAs + 3O_2 \longrightarrow In_2O_3 + As_2O_3 \tag{3.4}$$

$$2InAs + As_2O_3 \longrightarrow In_2O_3 + 4As \tag{3.5}$$

The final predicted oxide film composition is $GaSb/(Ga_2O_3 : Sb)/(Ga_2O_3 : Sb_2O_3)/GaSbO_4$ and $InAs/(In_2O_3 : As)/(In_2O_3 : As_2O_3)/InAsO_4$ for GaSb and InAs, respectively.

The XPS measurements [49] carried out on oxidized InAs detected the presence $InAs_xO_y$ at the oxide-InAs interface with composition closer to $InAsO_3$ than to $InAsO_4$. Moreover, elemental As was found distributed throughout the oxide film. This implies that the phase diagrams are not entirely complete and further XPS studies on oxide- InAs interfaces must be carried out for a whole picture. Additionally XPS measurements performed on oxidized GaSb [125] showed the existence of elemental Ga and Sb along with GaSb, Ga_2O_3, Sb_2O_3 and Sb_2O_5.

3.2.2 Effects of Native Oxides on Device Operation

Presence of native oxides on InAs, GaSb surfaces lead to the generation of surface states at their interface with air and this leads to pinning of the Fermi level. The

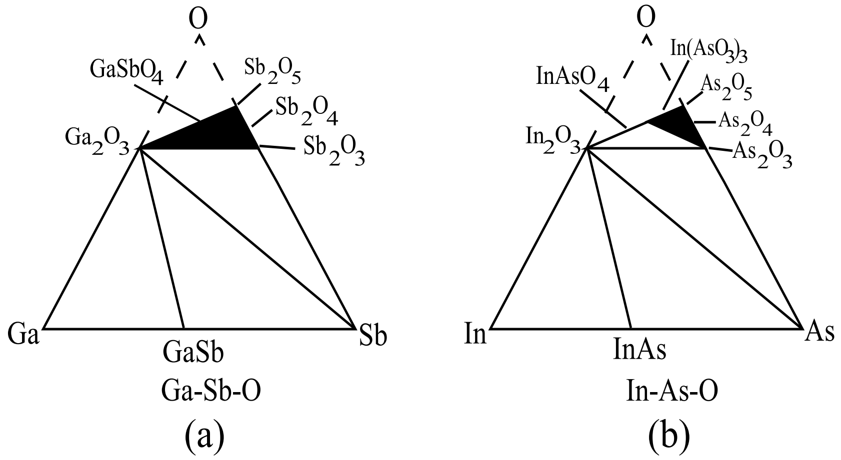

Figure 3.1: (a) $Ga - Sb - O$ and (b) $In - As - O$ equilibrium phase diagrams [102]

presence of various compositions of native oxides leads to the creation of additional interface states within the energy bandgap enabling trap-assisted tunneling. This can severely degrade the performance of the detector by increasing the dark current output of the device. Furthermore, the manifestation of elemental antimony during the thermal oxidation process of GaSb at the air-GaSb interface adds on to the already existing surface leakage currents. The reason for this increase in surface state density, hence in surface leakage currents is due to the metallic nature of elemental Sb providing an alternate conduction path for the transport and propagation of charge carriers. Therefore the definition of sidewalls free of native oxides is crucial for the working of an efficient, reproducible InAs/GaSb SLS IR detector.

Pre-treatment etches are utilized to remove unwanted native oxides from device surfaces prior, during or immediately after the pixel isolation process, but before metal/passivation deposition. In Schwartz et al [101], the oxidation of both group III elements, In and Ga, are reduced to 40% of that found in the native oxide by the 10 second etch in NH_4OH. The Ga oxide quickly returns with ozone treatment and then saturates, while the In oxide increases more slowly. On the other hand, the group V oxides are only slightly reduced by the oxide etch. Since it is clear that the oxide etch causes a detrimental change in the detector surface, the much greater reduction in the group III oxides suggests that good device performance will require that these oxides be restored to the levels in the native oxide. An XPS investigation of the InAs or GaSb surfaces after treatments mimicking those performed on the detectors shows that the group III oxides are most affected by the native oxide etch [77]. This implies that the In and Ga oxides are needed to effectively passivate the surface. Furthermore, InO_x may be the more important oxide to encourage in the quest of eliminating surface conduction.

It has also been observed that the immersion in passivant ammonium sulfide [$(NH_4)_2S$] [9] immediately after mesa definition etch effectively removes native oxides with minimal surface etching. This is due to the formation of $(NH_4)OH$ in water solution of $(NH_4)_2S$. A 10-30 sec dip of InAs/GaSb SLS sample in phosphoric acid based (H3PO4 : H2O2 : H2O = 1:2:20) or hydrochloric acid based (HCl : H_2O = 1:10) solutions is observed to also remove native oxide with minimal surface damage [81]. Introduction of BCl_3 gas into the plasma chemistry is also effective in removal of native oxides and re-deposited byproducts [36].

3.3 Surface Passivation

Before we look into each of the constituent passivant material, it is essential to establish the criteria we look for in a particular passivation technique. An ideal passivation technique must encompass the following criteria:

1. The surface passivant must prevent interaction between semiconductor surface and ambient atmosphere.

2. It must eliminate the formation of interfacial states in the forbidden gap of the semiconductor;
3. The passivant must also serve as an effective energy barrier for charge carriers at the surface. This means the surface passivant material must possess sufficient energy barrier so that electrons will not be lost from the semiconductor surface to the passivating layer. It also means that the passivation layer must not form an alternate conducting layer either;
4. Uniform deposition of passivant on the device surface is crucial, as this can decrease the stress at the interface between passivant and semiconductor;
5. Thermal stability i.e. the passivant must not undergo any change in its constitutional, physical and interfacial properties during various cycles of temperature is crucial as SLS based IR detectors are known to operate not only at low temperatures of 10-77K but also at room temperature (300K);
6. Long term stability of the passivant is crucial especially when we look for commercial application. Ergo, an ideal passivant must perform all the above factors throughout the lifetime of the detector

3.3.1 Categories of passivation

The work on passivation of bulk III-V semiconductor surfaces was following in two main directions, as stated in work of Bessolov et al [12].

1. Encapsulation is when a surface passivant prevents the interaction between semiconductor surface and ambient atmosphere. In this category, the passivation is carried out by either deposition of relatively thick insulator layers or photoresist/organic based solutions are spun on to the surface. Here, the

semiconductor/insulator heterojunction with properties defined by the density of states at the interface is formed. Encapsulant passivation can then be categorized depending on the make-up of the material such as:

   (a) Dielectric/insulating passivants- SiN_x and SiO_2.

   (b) Organic Passivants- Polyimide and SU-8

2. Chemical passivation is a general term that defines all passivation techniques where in all surface bonds are covalently satisfied thereby shifting the surface states out of the bandgap and into the valence and conduction bands. We have also seen the use of the term electrical passivation which implies passivants that remove interfacial states from the band gap and/or prevent their formation [83]. Just as in encapsulant passivation, chemical passivants can be categorized depending on the make-up of the material such as:

   (a) Chalcogenide passivation such as Zinc Sulfide (ZnS) and Ammonium Sulfide ($(NH_4)_2S$)

   (b) Sulfide passivation such as Electrochemical Passivation (ECP)

   (c) Passivation by Overgrowth of wider bandgap material

Our research employs the same categorization of passivation methods of InAs/GaSb SLS detectors, in particular, encapsulation of etched sidewalls with thick layers of dielectrics, organic materials (polyimide and various photoresists), or wider-band gap III-V material, and chalcogenide passivation, that is saturation of unsatisfied bonds on semiconductor surface by sulphur atoms. The following sections will take an in-depth look into each of the categories mentioned above.

3.3.2 Dielectric Passivation

1. **Silicon Dioxide (SiO_2) Passivation of InAs/GaSb SLS Detectors** Si (solid)+O_2 (gas) =SiO_2 (solid) is a heterogeneous reaction. SiO_2 is stable to InAs/GaSb in the usual processing temperatures without any reactions. However, in the presence of water molecules (humidity) and/or sodium ions arising from improper quality of de-ionized water used for rinsing, there can be secondary reactions between amorphous SiO_2 layers and InAs/GaSb. Incidentally, SiO_2 layers are invariably amorphous since silica is a glass forming constituent i.e. only under special conditions SiO_2 crystallizes to quartz (crystalline solid).As in silicon nitride, in SiO_2, silicon is cationic Si(4+) whereas oxygen is anionic O(2-) i.e. oxide ion. When you cross multiply the charges in the formula, we get Si_2O_4 or simplified as SiO_2. This forms the most thermodynamically stable phase in the silicon-oxygen system.

   Gin et al. [40] reported passivation of InAs/GaSb SLS detectors with SiO_2 resulted in improvement of zero-bias resistance by a factor of 2, which leads to a detectivity improvement of 41%, assuming all other variables remain the same as with unpassivated detectors. The best passivation results were achieved with SiO_2 grown in plasma enhanced chemical vapor deposition (PECVD) system at 160°C. It should be noted that the typical temperature of SiO_2 deposition in a PECVD system is 320°C [52]. Special care has to be taken to develop a low-temperature process of high-quality SiO_2 deposition to prevent SLS period intermixing.

   Hood et al. [51] utilized SiO_2 for passivation of very-long wavelength ($\lambda_{50\% cut-off}$ = 12.0 μm at 77K) IR InAs/GaSb SLS detectors. Approximately 300 nm of silicon dioxide was deposited by PECVD at a susceptor temperature of 160°C. The R_0A fell in the 0.02-0.07 Ω cm^2 range for nearly all passivated diodes. A surface resistivity was evaluated to 7 Ω cm and 33 Ω cm for unpassivated and silicon dioxide passivated devices, respectively. Nolde et al. [77] have investigated relationship between thickness and composition of native oxides on LWIR ($\lambda_{\ 50\%cut-off}$ = 8.75 μm at 77K) InAs/GaSb SLS detector sidewalls prior SiO_2 deposition and diode performance. The best surface resistivity ($4.38 \times 10^6\ \Omega\ cm$) was demonstrated by detector with ozone-enhanced native oxides.

2. **Silicon Nitride (SiN_x) Passivation of InAs/GaSb SLS Detectors**

   Si_3N_4 is the stoichiometric compound formed by the reaction of Si which is the fourth group element in the periodic table having the valency of +4 and N which is the fifth group element with the negative valency of -3 i.e. 5-8=-3. Here Si can be considered a cation having Si(4+) charge and N can be considered as an anion having N(3-) charge. When the two form a compound, we cross-multiply the values of charges and hence the stoichiometric compound silicon nitride i.e. Si_3N_4 is formed and this is the most stable configuration. Si_3N_4 is a high melting ceramic solid with high melting point, low thermal expansion (and therefore highly thermal shock resistant), high fracture toughness and chemically least reactive to water vapor molecules and sodium ions, whereas SiO_2 is reactive to both these reagents. Hence Si_3N_4 layers are coated over integrated chips as passive layers. SiN_x is a chemical representation for non-stoichiometric compound having no fixed Si: N ratios i.e. x is variable and generally is much less than 1. Therefore SiN_x is much richer in silicon and is mostly amorphous (i.e. like glass) and not crystalline as verifiable by x-ray diffraction. SiN_x has shown to be a mixed phase i.e. composite of Si_3N_4 (x-ray amorphous) in which nano-particles of Si (amorphous or crystalline) are embedded within. In our research work, we deposit SiNx at or above 300°Cin a plasma enhanced chemical vapor deposition (PECVD), because the layer tends to crystallize on hot substrates. The atoms/molecules deposited on hot substrates reorganize in 2-dimensional layers leading to better crystallinity. At higher substrate temperatures, nitrogen reacts with silicon nano-particles more easily. This will ensure higher electrical resistivity and hence lower leakage currents.

Dielectric passivation, though shown to be effective, presents challenges such as developing high-quality, low fixed and interfacial charges density dielectrics at process temperatures substantially lower than the InAs/GaSb SLS growth temperature to prevent the SLS period intermixing. Moreover, dielectric passivation layer alters the band bending presented at mesa sidewalls caused by abrupt termination of the periodic crystal structure. This band bending induces accumulation or type inversion of charge resulting in surface tunneling currents along sidewalls. As was shown by Delaunay et al. [25], the narrow bandgap devices (with bandgap of 120 meV or lower) are more susceptible to the formation of charge conduction channels along the sidewalls. Native fixed charges presented in dielectric passivation layer (e.g. SiO_2) can either improve or deteriorate the device performance, [22] consequently, the dielectric passivation may not passivate the low band gap materials as effectively as high bandgap materials. Despite all of the potential drawbacks, the dielectric (SiO_2) passivation attracts attention of researchers for passivation of LWIR SLS detectors because it is compatible with current FPA fabrication procedures.

3.3.3 Passivation with Organic Materials

Organic materials (photoactive polyimides, epoxy polymer such as SU-8 or various photoresists) are attractive for the passivation of InAs/GaSb SLS detectors due to simple integration into fabrication procedure. Usually they are spin-coated at room temperature with different speeds that give rise to film thicknesses in the range of 0.2 -100 μm. The passivation mechanism of these organic materials can be either encapsulant or passivant. We consider them as encapsulants i.e. they envelop the device surface but do not make any chemical/atomic bonds with the exposed crystal lattice of the InAs/GaSb superlattice. Photoresists contain the corresponding monomer or oligomer (partly polymerized) plus one or more photo-sensitizers. Chemically and intrinsically the corresponding giant molecules (polymers) are not true passivants. They form coherent dielectric coatings having high resistivity and therefore decrease surface leakage currents. Whether the monomers (before polymerization) or the photo-sensitizers therein are modifying the surface states present on GaSb or InAs/GaSb SLS structures is not reported so far. Since the solutions before photo-polymerization are able to cover on to the sidewalls as well as the flat surfaces of the mesa; the organic solutions may exhibit better encapsulation stability. Post photo-polymerization, these set/hardened indicating long-term durability.

Passivation of MWIR [58, 33] and LWIR [57] SLS detectors with SU-8 have been reported. SU-8 is a high-contrast epoxy-based negative photoresist, which was developed by IBM [3]. Presently, SU-8 is widely used in MEMs [5] and optoelectronics applications [92]. SU-8 consists of a bisphenol-A novolak epoxy resin, a photo initiator, and solvent γ-butyroalectone [116]. The photo initiator is easily broken down and changes into strong acid ($HSbF_6$) upon exposure of UV. This acid causes a high cross-link density in the SU-8 film, thereby leading to an increase in its chemical resistance to the developer. Photo-polymerized SU-8 is mechanically and chemically stable after a hard bake.

Comparison of unpassivated and SU-8 passivated single pixel SLS MWIR devices ($\lambda_{\ 50\% cut-off}$ = 4.6 μm at 77K [58]) resulted in four orders of magnitude reduction in dark current density (from 8×10^{-3} to 5×10^{-7} A/cm^2 at an applied bias of -0.3V), and five-fold increase in the surface resistivity (from 1.9×10^2 to 1.0×10^3 $\Omega \cdot cm$ at 87 K). DeCuir et al [33] investigated the effect of SU-8 pas-

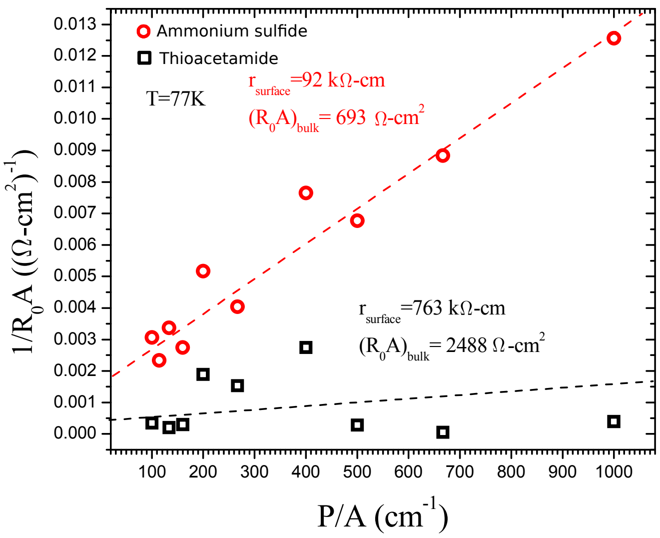

Figure 3.2: Inverse R_0A vs. P/A of diodes for two sets of variable area diodes (ranging from 40-400 μm) using either ammonium sulfide or thioacetamide pre-treatment. Reprinted from Ref. [33]

sivation on MWIR ($\lambda_{\ 50\%cut-off}$ = 4.9 μm at 77K) SLS detectors preceded by the non-aqueous thioacetamide treatment or ammonium sulfide treatment. Figure 3.2 presents inverse R_0A vs. P/A of diodes for two sets of variable area diodes (ranging from 40-400 μm) using either ammonium sulfide or thioacetamide pre-treatment. The eight-fold increase in surface resistivity of SU-8 passivated diodes pre-treated with non-aqueous thioacetamide has been observed as compared with aqueous ammonium sulfide.

Passivation of LWIR ($\lambda_{\ 100\%cut-off}$ = 12 μm at 77K [57])InAs/GaSb SLS detector resulted in a 30-fold reduction in the dark current density at a low value of applied bias ($V_b = -0.1V$) for the small area (50 μm x 50 μm) devices, as shown in Figure 3.3. It should be noted that a considerable degree of nonuniformity of dark current densities for unpassivated devices was observed and the uniformity was improved after the SU-8 passivation.

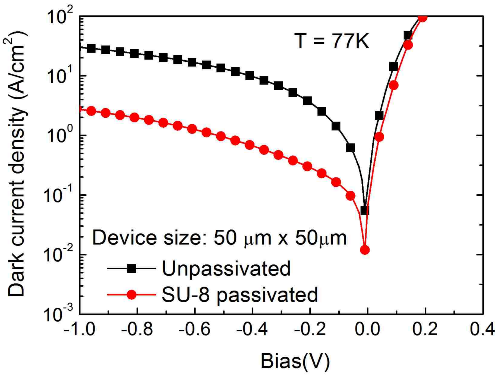

Figure 3.3: Dark current density vs applied bias for LWIR unpassivated and SU-8 passivated small area device. Reprinted from Ref. [57]

Hood et al [50] reported on passivation of InAs/GaSb LWIR SLS detectors ($\lambda_{100\%cut-off}$ = 11.0 μm at 77K) with polyimide layer. Polyimides (sometimes abbreviated PIs) are polymers of imide monomers, widely known for their thermal stability, good chemical resistance, and excellent mechanical properties. In performed study, conformal polyimide (PI-2555, HD Microsystems) was spun onto the sample with defined mesas. No surface dependence was observed and diodes R_0A values were found within the range of $\sim 6 - 13\ \Omega\ cm^2$. Moreover, authors found that prolonged vacuum desorption (288 hrs) performed prior polyimide passivation helped to improve the uniformity of R_0A values and to bring the zero-bias electrical behavior close to the near bulk-limited case. In addition, polyimide passivation was shown to be stable upon exposure to various ambient conditions as well as over time. The polyimide passivated devices (LWIR,$\lambda_{100\%cut-off}$ = 10.0 μm at 77K) were measured again after 3 months of storage in ambient conditions [73]. The same R_0A and perimeter/area trend as in the initial measurement were obtained, which confirmed the long-term stability of this passivation technique.

Chaghi et al. [21] reported on passivation of the MWIR InAs/GaSb SLS detector ($\lambda_{\ 50\% cut-off}$ = 4.9 μm at 80K) sidewalls with photoresist. Photoresist AZ-1518 was spun onto the sample right after the mesa etching and heated at 200°C for 2 hr to be polymerized. It was found that photoresist effectively protects the device sidewalls from oxidation in ambient atmosphere, moreover, performance of passivated devices was not degraded over three weeks suggesting good long-term stability of photoresist passivation.

3.3.4 Passivation with Wide-bandgap Materials

Surface currents may be suppressed by reduced exposure of narrow gap materials to the environment as a result of deposition of wider band gap materials on etched sidewalls or the ``shallow etch ′′technique that isolates the neighboring devices but terminates within a wider bandgap layer.

Rehm et al. [95] have suggested passivation of SLS InAs/(In,Ga)Sb LWIR photodiodes ($\lambda_{50\%}$ = 10 μm at 77K) by subsequent overgrowth of lattice matched, large-bandgap semiconductor layer ($Al_xGa_{1-x}As_ySb_{1-y}$) over etched mesa sidewalls (shown in Fig. 3.4. Position of the Fermi level at the interface can be adjusted by variation of doping concentration of the large-gap semiconductor material. In order to prevent Al-containing passivation layer from oxidation, thin (200 nm) layer of silicon nitride was deposited after re-growth process.

Mesa sidewalls encapsulation with GaSb to eliminate the surface currents in InAs/GaSb FPAs has been proposed by Szmulowicz and Brown [122]. In an offered scheme, the GaSb encapsulant acts a barrier to electrons at both the n- and p-sides of the SLS and as a well for the minority holes on n-side of the junction. Thus electrons are confined in the SLS whereas holes are depleted from the active volume of the device. The surface currents are reduced by eliminating sidewalls,

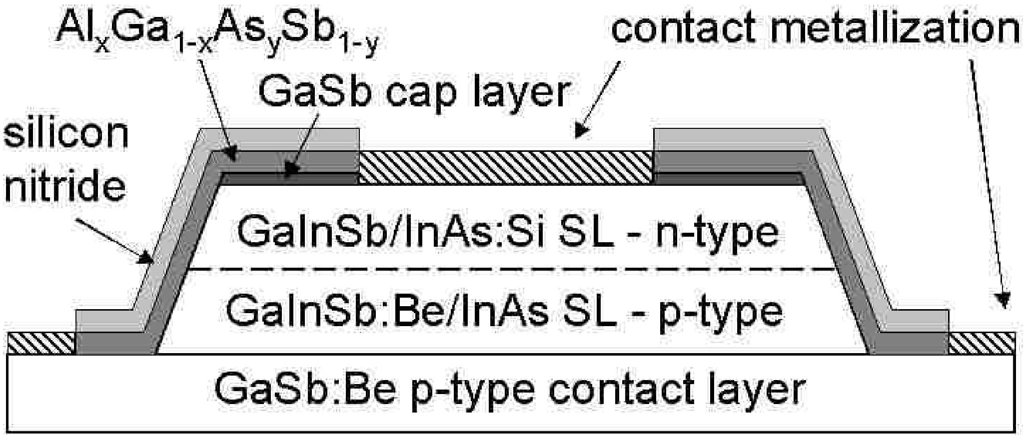

Figure 3.4: Cross-sectional schematic of a completely fabricated InAs/(In,Ga)Sb LWIR SLS photodiode passivated by MBE overgrowth with AlGaAsSb. Reprinted from [103]

in addition, the SRH and Auger recombination lifetimes are expected to be higher due to reduction of hole density in the depletion region.

Aifer et al. [6] proposed the shallow-etch mesa isolation (SEMI) approach for the device definition. The neighboring photodiodes are isolated from one another by etching just deep enough to break the doping-defined junction and to leave the narrower-gap IR-absorbing layer buried below the wider-gap material. SEMI restricts the exposed surfaces to the wide-band gap layers, thus suppressing the surface recombination and the ability of surface electric fields to produce conducting channels that would bypass the junction.

Passivation of narrow bandgap SLS material with wide bandgap materials regrown on sidewalls of fabricated device by MBE is an effective technique for the surface leakage current reduction. However, this passivation approach requires very careful surface cleaning prior the overgrowth procedure, which significantly complicates the integration of this passivation methods into fabrication process of detectors and FPAs.

The "buried" architecture of InAs/GaSb SLS detectors realized with "shallow etch" technique excludes the need for the passivation. Due to the way detectors are fabricated, the size of the device is not defined by the etch dimensions but by the lateral diffusion length of minority carriers. If the values of lateral diffusion length are larger than the distance between neighboring pixels in the FPA, crosstalk between the FPA elements can be encountered. Presence of crosstalk in the FPA could lead to degradation of image resolution. Although Aifer et al. [6] did not observe the evidence of cross-talk for 256 x 256 FPA with 40 μm pitch and 24-μm-wide SEMI mesas based on graded bandgap W-structure, further investigation of SEMI approach realized on SLS detectors based on different heterostructures is needed.

3.3.5 Chalcogenide Passivation

The next approach of passivation of InAs/GaSb SLS detectors we will study is chalcogenide passivation. In the past there were a number of reports on the improved electronic properties of chalcogenide-passivated III-V materials. In particular, enhanced photoluminescence (PL) and band bending were observed on passivated GaAs (001) surfaces [113, 117, 16]. Based on the photoreflectance measurements, Paget et al [82] proposed that the formation of Ga-S bond was responsible for the reduction of surface states within the forbidden gap.

Passivation of InAs (001) surface by ammonium sulfide solution was also studied [80, 85]. It was found that passivation effectively removes native oxide with the minimal surface etching and creates a covalently bonded sulfur layer. Final structure of passivated InAs surface can be represented by S-on-In-on-As layer-cake model. as shown in Fig 3.5(a). In this idealized model there exits alternating

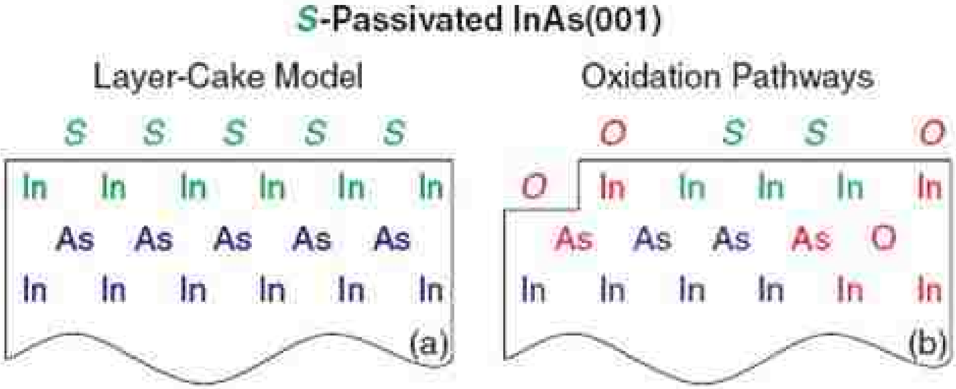

Figure 3.5: Schematic of a S-passivated InAs(001) surface.(a) The idealized layer-cake structure model. (b) Potential oxidation pathways [85].

In and As atomic layers with the top In layer terminated by the passivating S layer. Also, this structure proposes exclusively In-S and not As-S bonding [85]. Further, this model describes the mechanism of oxidation on a S-passivated InAs wherein displacement of S by O takes place along with oxidation of defects in the top In layer, and oxygen diffusion through the protective layer as shown in Fig 3.5 (b).

In order to improve the GaSb surface characteristics, various surface passivation processes have been studied based on wet or dry chemical processing. Stimulated by the successful application of sulfide passivation of GaAs surfaces, the passivation of GaSb surfaces by alkaline sulfides, including Na_2S and $(NH_4)_2S$ in aqueous solutions, have been studied by several research groups [84, 32, 11]. Observation of enhanced PL intensity and reduced diode leakage current indicated the improvement in the electrical and optical properties of the GaSb surface by sulfur-based treatments.

The theory of chalcogenide passivation is developed for the most studied material among III-V compounds, GaAs [14, 15, 16]. The reduction in the density of surface states by chalcogenide passivation was attributed to the formation of an ordered layer of sulfur adatoms on the surface. Electronic structure of the passivated surface could be predicted theoretically based on the suitable choice of reconstruction, optimization of the position of the atoms on the surface due to total energy minimization, and calculation of the density of electronic stated distribution for the given atomic structure. Following this procedure, Ohno et al [78, 79] reported the theoretical calculation results for ideal GaAs (001)-1x1 surfaces with a full monolayer of S atoms adsorbed on either the Ga- or As- terminated surface. They found that surface bridge sites were energetically favorable for S adsorption.

The interactions between the Ga dangling bond and the S sp^3 orbitals form the bonding and anti-bonding states. The fully filled bonding states are located within the valence band, while the empty anti-bonding states are in the conduction band. Therefore the S adsorption on an ideal Ga-terminated surface replaces the mid-gap Ga-related surface states with a low-lying S-induced surface states. However, on an As-terminated surface, the S-As anti-bonding states are still within the energy gap and they are partially filled with electrons, preventing the reduction of the gap-region surface state density.

In general, mechanism of formation of passivation coating for III-V compound can be divided into two stages:

1. Removal of oxide layer from the surface
2. Transfer of electrons from the semiconductor into the solution and formation of chemical bonds between semiconductor and sulfur atoms

Bessolov and Lebedev [12] described the sulfidization of III-V semiconductors from solutions of inorganic sulfides as an red-ox reaction

$$A^{III}B^{V} + HS^{-} + R - OH \longrightarrow \qquad (A^{III})_{x'}S_{y'} + (B^{V})_{x''}S_{y'} + R - O^{-} + H_2$$

here R is a hydrogen atom (for aqueous solutions) or an alkyl group (for alcohol solutions). The sulfide coating is a mixture of different sulfides, since the stoichiometric coefficients x(x) and y(y) can vary from 1 to 5.

It was proposed the formation rate of sulfur passivating coating should increase with increasing temperature of treatment, the concentration of sulfur atoms in the solution and with reduction of pH of the solution.

From the passivation study of GaAs it was found the sulfidization of III-V semi- conductors proceeds more efficiently in alcohols than in water. It was attributed to the lower dielectric constants of alcohols: a less polar medium allows a stronger electrostatic interaction between solution ions and the semiconductor surface. Liu et al [133, 64, 65] investigated non-aqueous versus aqueous-based passivation of GaSb (100) surfaces. A non-aqueous passivation solution contained sodium sulfide in anhydrous benzene. To increase solubility of sodium sulfide, a cation complexing agent, 15-crown-5, (a compound of the crown-ether family) was added to the solution. Aqueous passivation consisted of the immersion of GaSb wafers in saturated Na_2S aqueous solution. The aqueous passivation resulted in a threefold increase in PL intensity whereas non aqueous passivation resulted in marked enhancement in PL intensity. In addition, the non-aqueous passivation process exhibited higher sulfide coverage, lower content of the residual oxide as well as elemental Sb.

1. Ammonium Sulfide Passivation of InAs/GaSb SLS Detectors

   Passivation of InAs/GaSb SLS detectors with aqueous ammonium sulfide solutions is easily integrated into fabrication sequence, since it is performed simply by immersion of sample in $(NH_4)_2S$-based solutions. Moreover, no native oxide removal step is required prior passivation, since the native oxides are etched by $(NH_4)OH$ formed in water solution of ammonium sulfide.

Ammonium Sulphide when utilized for passivation purposes is usually in aqueous form. An established comprehensive chemical model is missing in literature for these reactions and therefore we will try to expand on them here. The chemistry of sulfur in aqueous media is that $(NH_4)_2S$ does not prevail in solutions only as NH_4+ and S_2- ions, but as:

$$(NH_4)_2S = 2NH_4(+1) + S(2-) \tag{3.6}$$

$$(NH_4)_2S + H_2O = NH_4OH + NH_3 + H_2S \tag{3.7}$$

$$(NH_4)_2S + HO(-1) = NH_4OH + NH_3 + HS(-1) \tag{3.8}$$

Thus the solution contains S_2, HS(-1) and H_2S of which HS(-1) ions dominate in the pH range of 8 to 14. Besides, S_2- and HS(-1) can undergo catenation i.e. a type of polymerization involving its own kind (in this case S atoms).

$$HS(-1) + S(2-) = HS_2(1-) + 2e(-) \tag{3.9}$$

$$HS(-) + 2S(2-) = HS_3(1-) + 4e(-) \tag{3.10}$$

H-S-S(-1), H-S-S-S(-1),(and so on), are called disulfide, trisulfide (and so on) ions leading to polysulfide ions i.e. HS_n(-1) where n is a large number.

Gin et al [41] reported passivation of InAs/GaSb LWIR ($\lambda_{100\%cut-off} = 8$ μm at 77K) SLS detectors with various solutions of ammonium sulfide. The soaking of 400 μm x 400 μm square mesa samples in full-strength ammonium sulfide [$(NH_4)_2S$ 20%] solutions for 15 minutes resulted in reduction of dark current density by factor of 2 and improvement of maximal differential resistance by factor of 3 compared with unpassivated devices. However, examination of the passivated samples under the scanning electron microscope revealed the severe undercut of the detector mesas and etching of the GaSb buffer layer. To reduce the deleterious effect of dull-strength ammonium sulfide solution, samples were treated with the $(NH_4)_2S$ solution diluted in four parts of de-ionized water for the same time. No visible damage on sidewalls was observed, and dark current density was reduced at least by two orders of magnitude as compared to unpassivated samples. With increased time of passivation treatment the efficiency of passivation was improved. The average values of differential resistance were 18.23 kΩ and 19.61 kΩ for 15 and 30 min passivation, respectively, versus 970 Ω for the unpassivated detectors.

The mechanism of ammonium sulfide passivation on LWIR InAs/GaSb SLS detectors was in details investigated by Banerjee et al [9]. X-ray photoelectron spectroscopy (XPS) measurements were performed on as-etched with phosphoric acid based solution ($H_3PO_4 : H_2O_2 : DIH_2O$ = 2:1:20 for 1 min) and ammonium sulfide treated (24% aqueous $(NH_4)_2S$ solution at 60° for 15 min) LWIR SLS samples. Figure 3.6 shows XPS spectra obtained for as-etched and $(NH_4)_2S$-treated samples for In (Fig. 3.6 a), As (Fig. 3.6 3.6 b), Ga (Fig. 3.6 c), and Sb (Fig. 3.6 d).

The sulfur peak in the range of 161 eV to 165 eV [2] corresponding to the binding energy of sulfur $2p_{3/2}$ bonded to In, As, Ga, or Sb was too weak on either sample and could not be distinguished from the background. The results indicate that no sulfur bonds were created during the treatment. However, it is also clear that the oxides were removed effectively and the surface was sustained after 30 min of exposure to air, indicating weak sulfidization. The XPS measurements were repeated on the same samples exposed to the ambient atmosphere for ten days and revealed reappearance of the detrimental

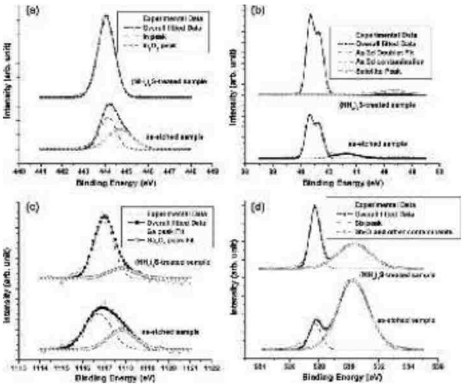

Figure 3.6: (a) In 3d5/2, (b) As 3d, (c) Ga 2p3/2, and (d) Sb 3d5/2 of as-etched (bottom) and ammonium sulfide treated (top) SLS samples. Reprinted from Ref. [125]

oxides on the surface of treated samples earlier also observed by other researchers [94].

In conclusion, the aqueous ammonium-sulfide treatment showed the short-term benefits for performance of InAs/GaSb SLS LWIR detectors. However, the treatment may cause the degradation of device performance attributed to the secondary oxidation, since the hydrophobic surface generated by oxide removal step repels the solution and leaves the surface exposed for O_2-re-adsorption. In addition, temporal instability of such passivation layer was observed and the necessity for a suitable capping layer to preserve good passivation quality in the long term was reaffirmed.

2. Thioacetamide passivation of InAs/GaSb SLS Detectors

Thioacetamide (C_2H_5NS or TAM) has been proposed as an alternate sulfidizing agent for the passivation of GaSb and InAs surfaces [120] as well as GaInAsSb [112] and InAs/GaSb LWIR [10] photodiodes. Depending on preparation the TAM solution may be acidic or basic, in contrast with always basic aqueous solution of $(NH_4)_2S$. As a result, TAM treatment offers formation of more stable M-S bonds, where M is Ga, In, As or Sb, than ammonium sulfide treatment resulting in weaker M-O-S bonds. Moreover, the TAM treatment does not produce elemental antimony on the semiconductor surface.

The acidic TAM passivation of LWIR InAs/GaSb SLS mesa-etched photodiodes resulted in four times improvement of R_0A value (590 Ωcm^2 at 85 K) compared to ammonium sulfide treated diodes. However, the XPS studies revealed the reappearance of surface oxides on the TAM treated surface after long term air exposure asserting the need for a suitable capping layer.

3. ZnS Passivation of InAs/GaSb SLS Detectors

ZnS is an attractive candidate for the passivation of InAs/GaSb SLS detectors, since it effectively saturates the dangling bonds with sulfur and acts as self-encapsulant, preventing desorption of sulfur atoms from the surface. Moreover, electron-beam evaporated ZnS showed relatively small fixed charge density [62] with which the SLS detector sidewalls surface is hardly inverted or accumulated to induce tunneling current. Typical thickness of ZnS film is 200-400 nm, the deposition rates are 0.607 Å/s below 500 Å and then 11.2 Å/s until the end. A slower initial deposition rate is maintained to help the passivant molecule to find the minimum energy position on the semiconductor surface.

The chemical interaction of ZnS on GaSb and InAs of the superlattice is an example of how a typical Chalcogenide would interact with the InAs/GaSb superlattice. The chemical formulations are such:

$$(1-x)GaSb + xZnS = Ga(1-x)ZnxSb(1-x)Sx \tag{3.11}$$

$$(1-x)InAs + xZnS = In(1-x)ZnxAs(1-x)Sx \tag{3.12}$$

Herein, Zn goes into cationic sub-lattice of either Ga or In and act as acceptor impurity, since it has effectively one positive charge less than Ga or In i.e. Zn^{2+} in the place of Ga_{3+} or In^{3+}. Sulphur (S) goes into the anionic sub-lattice of Sb or As and act as donor impurity since it has one electron more than Sb or As i.e. S(2-) in the place of Sb(3-) or As(3-). Thus, ZnS diffusion into the SLS as zinc and sulfur atoms causes equivalent acceptor and donor states and thereby increasing the surface resistance.

Sb_2S_3 or Sb_2S_5 are not metallic since there are no multiple valencies for any of the constituents in both the solids. It must me noted that metallic in nature here means the resistance of a material increases with increasing temperature while for insulators (including semiconductors), resistance decreases with temperature. Now in solids with mixed valencies of the same constituent, metallic nature can be seen e.g. Ti_2O_3 is metallic since Ti^{2+} and Ti^{4+} coexist in this solid. In Sb_2S_3, all Sb atoms are in 3+ valence state whereas in Sb2S5 all Sb atoms are present in Sb^{5+}. In both cases, S atoms are present as S^{2-} and consequently no mixed valence states are present in the same solid.

Mallick et al [67, 68] reported on ultralow noise MWIR InAs/GaSb SLS avalanche photodiode (APD, $\lambda_{\ 100\%cut-off}$ = 4.14 μm at 77K) passivated with ZnS. ZnS passivated APD showed a maximum R_0A value of $7.5x10^5$ Ω cm^2 and dark current of 2 μA at a reverse bias of -1.0 V. Compared to an unpassivated diode, the ZnS-passivated APD demonstrated the R_0A value enhanced by a factor of 3.5, dark current reduced by an order of magnitude, as well as increased the breakdown voltage and multiplication gain by 10 V and factor of 20, respectively.

The same research group investigated the effectiveness of ZnS passivation on InAs/GaSb SLS LWIR ($\lambda_{\ 100\%cut-off}$ = 10 μm at 77K) detectors [8]. The maximum R_0A value and dark current density of ZnS passivated detector were 492 $\Omega\ cm^2$ and 0.01 A/cm^2 compared to the 0.72 $\Omega\ cm^2$ and 1.93 A/cm^2 of unpassivated devices. To reduce the native oxides, prior the deposition of ZnS the APD and LWIR detector samples were treated with 20% warm (60°C) aqueous solution of $(NH_4)_2S$ for 10 min.

4. Electrochemical Passivation (ECP) of InAs/GaSb SLS Detectors

   The ECP cell (shown in Fig. 3.7) consisted of the sample (anode), a platinum mesh electrode (cathode) and the electrolyte (0.1M Na_2S in ethylene glycol) in a glass beaker at room temperature [87]. A constant DC current of 33μA was supplied using a programmable current source for a limited time of 5min. Once the electrical stimulus is applied, the following reactions take place:

$$Cathode : 2Na^{+} + 2e \longrightarrow 2Na \tag{3.13}$$

$$Anode : S^{2-} \longrightarrow S^{+} + 2e \tag{3.14}$$

   Hence the sample placed at the anode is deposited by pure sulphur. After the 5min duration, the sample is blow dried with N_2.The AES measurements shown in Fig. 3.8, indicated that the deposited sulfur-rich layer uniformly distributed over exposed sidewalls. AES detected not only sulphur, but also the presence of sodium, carbon and oxygen on the SLS sidewalls which are remnants from the ECP electrolyte. The thickness of this sulphur-rich layer was estimated to be was 50Åthick.

In electro-chemical passivation (ECP), the electrolyte solution consists of Na_2S and ethylene glycol. Specifically, Na_2S can be termed as the electrolyte and the ethylene glycol(EGL) i.e. CH_2OH-CH_2OH or $C_2H_6O_2$ is the non-aqueous solvent. The latter is chosen so as to minimize the incorporation of OH(1-) ions in the sulfide layers which is widely prevalent when water is used as the solvent for ECP. Even in non-aqueous medium of EGL, the OH-incorporation in the deposited films is not totally avoided since Na_2S and $(NH_4)_2S$ are not soluble in water-free EGL. Hence we dissolve these solids in minimum water and then mix with EGL. Deposition of sulfur alone from ECP is not assured in an anodic compartment of the electrochemical cell. Presuming that the deposit is dominantly S-rich, the latter can vary from S_2, S_3 so on upto S_8 since elemental sulfur does not exist as atomic S but as molecular species dominantly S_8. It has to be noted that EGL is only a solvent and does not form a part of the solid deposit. The deposition rates will control the surface roughness which in turn is dependent on the applied anodic potential and the current density during ECP deposition process. Significantly, the XPS studies of ECP layers [131] from a Na_2S source show partial oxidation of sulfide to sulfite along with Na contamination in the passivated layer.

Electrochemical passivation (ECP) of MWIR ($\lambda_{100\%cut-off}$ = 4.5 μm at 77K) and LWIR ($\lambda_{100\%cut-off}$ = 10 μm at 77K) InAs/GaSb SLS photodiodes has been demonstrated by Plis et al [91]. Figure 3.9 shows three orders of magnitude improvement in R_0A product for MWIR SLS detector at 50K after ECP. To measure the stability of the passivation, dark current densities were measured for the as-processed and passivated devices. No considerable degradation of dark current density for passivated device was observed even after 12 weeks after ECP. ECP of LWIR InAs/GaSb SLS detectors (mesa area of 50 μm x 50 μm) resulted in dark current reduction by two orders of magnitude.

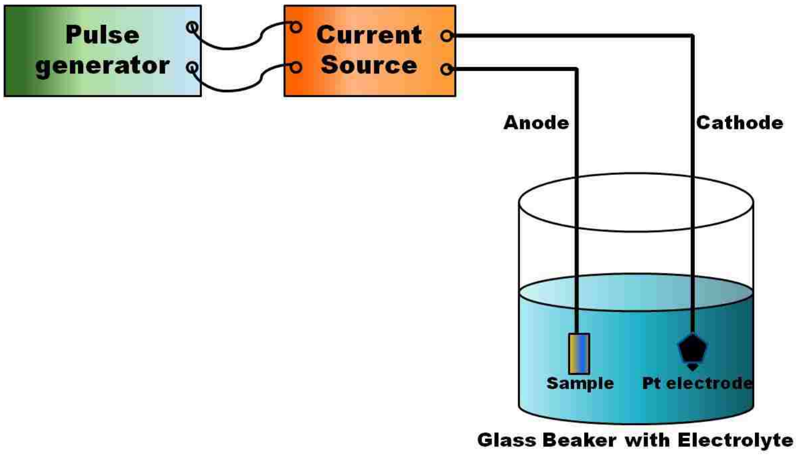

Figure 3.7: Schematic of the electro-chemical passivation set-up

Surface resistivity $r_{surface}$ was equal to 6 and 2717 Ωcm for the unpassivated and ECP treated detectors, respectively.

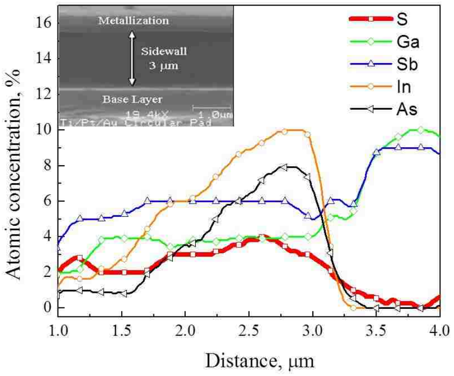

Figure 3.8: AES measurement of ECP passivated sidewall of a SLS detector showing presence of sulphur atoms. (Inset) SEM image is of the detector showing the sidewall of the device.

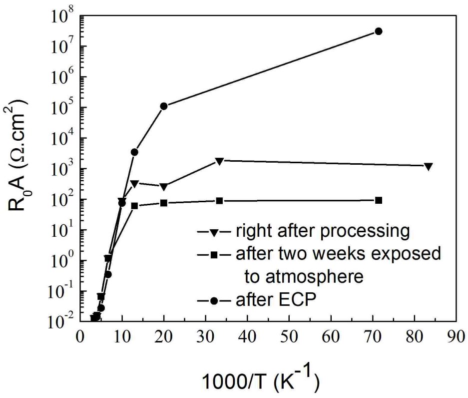

Figure 3.9: Dynamic impedance-area product at zero bias R_0A against temperature measured for as-processed, stored two weeks without inert atmosphere and passivated MWIR SLS detectors. Reprinted from Ref. [91]

3.3.6 Conclusions

The third generation of IR detection systems is expected to provide enhanced capabilities like larger number of pixels, higher frame rates, better thermal resolution as well as multicolor functionality. One of the most demanding challenges of present day SLS technology is the suppression of surface leakage currents associated with the exposed mesa sidewalls, which appear during the definition of device optical area. With scaling of pixel dimensions to 20 μm x 20 μm, FPA performance is strongly dependent on surface effects due to large pixels' surface/volume ratio.

In this chapter, we described in detail various passivation techniques of InAs/GaSb SLS detectors with operation wavelengths mainly covering MWIR and LWIR spectral regions. Since passivation treatment applied on a surface that is rough or contaminated by native oxides or with foreign particles will result in little or no improvement of device performance, we discussed methods of native oxide removal and single pixel isolation. In order to reduce surface currents on InAs/GaSb

SLS detectors researchers have employed two categories of passivation techniques: (a) encapsulation of etched sidewalls with thick layers of dielectrics (e.g. SiO_2), or organic materials (polyimide and various photoresists), and (b) saturation of unsatisfied bonds on semiconductor surface by forming covalent bonds with the InAs/GaSb SLS structure such as chalcogenide passivation or wider-band gap III-V material overgrowth with wide band gap material or shallow etch technique.

The dielectric passivation presents the challenges of developing high-quality, low fixed and interfacial charges density dielectrics at process temperatures substantially lower than the InAs/GaSb SLS growth temperature to prevent the SLS period intermixing. Dielectric passivation is shown to be effective for MWIR detectors; however it may not passivate the low band gap materials as effectively. The narrow bandgap devices (with bandgap of 120 meV or lower) are more susceptible to the formation of charge conduction channels along the sidewalls. Native fixed charges presented in dielectric passivation layer (e.g. SiO_2) can deteriorate the LWIR device performance. Method of band-bending control at SLS-SiO_2 interface by applying a voltage along devices sidewall has been recently proposed. The ability to establish the flat-band condition at SLS-dielectric interface together with compatibility with SLS FPA fabrication procedure makes dielectric passivation very attractive for passivation of LWIR SLS detectors.

MBE re-growth of a lattice-matched wide-bandgap III-V semiconductor layer on top of the exposed mesa sidewalls of narrow-bandgap SLS detector is an elegant solution of passivation problem in LWIR wavelength range. In addition to surface current reduction due to elimination of sidewalls, reduction of SRH and Auger recombination currents is expected (for the overgrowth with GaSb). However, this passivation technique requires very careful surface cleaning prior the overgrowth procedure, which significantly complicates the fabrication process of detectors and FPAs. The shallow etch mesa isolation approach (SEMI technique) restricts the exposed surfaces to the wide-band gap layers, thus suppressing the surface recombination and the ability of surface electric fields to produce conducting channels that would bypass the junction. Since no cross-talk has been registered for LWIR FPA mini-arrays (256x256) fabricated with SEMI technique, this passivation approach may be a way to solve passivation of SLS detectors operating in LWIR region.

Chalcogenide passivation through an immersion in a sulfur-containing solution, or deposition of sulfur based layer, effectively reduces dark currents in MWIR, LWIR and VLWIR InAs/GaSb SLS detectors. However, the chalcogenide-based passivation does not provide physical protection and encapsulation of the device and there are some reports on the temporal instability of such a passivation layer. Additional research on appropriate encapsulation of sulfur passivation layer needs to be performed, as well as the compatibility of S-based passivation with FPA fabrication procedure still needs to be investigated. The ZnS passivation solves the task of chemical passivation (i.e. saturates the dangling bonds) and simultaneously provides protection of devices sidewalls. However, no data are available yet on LWIR FPA passivation with ZnS.

In conclusion, there are various passivation techniques developed for passivation of MWIR and LWIR InAs/GaSb SLS detectors. However, there is no universal approach developed yet that would treat equally efficiently the SLS detectors with different cut-off wavelengths. Moreover, further studies have to be conducted on interface quality between SLS detector sidewall and passivation coating in order to better understand the chemistry underlying various passivation schemes. Finally, since passivation needs to be successfully integrated into FPA fabrication procedure, more research on compatibility of various passivations, especially S-based, with FPA fabrication, has to be performed.

Chapter 4

Mesa Definition of InAs/GaSb SLS Detectors

Semiconductor material surfaces when modified by technological processes such as cutting/cleaving, smoothing, mechanical polishing, annealing, epitaxial growth methods, device fabrication, exhibit damaged surface regions containing various abruptions like point defects, line defects, vacancies, stress, contaminants and native oxides. The impurities on a semiconductor surface can consist of physically or chemically absorbed gas, metal ions, organic material (carbon based compounds) or their combinations along with stable chemical compounds. It has to be noted that metallic contamination usually comes from chemical agents whereas organic solvents, photoresists (PR), or human interaction may be the sources of organic impurities. It is the exposure of the semiconductor surface to the atmosphere that activates its reaction with oxygen (O_2) molecules or with steam (H_2O) causing the formation of native oxides. In SLS device technology it is unavoidable to work without contact to atmosphere and hence it becomes crucial to prepare the surface with least amount of damage and this is often achieved by employing various etching processes.

During the fabrication process of InAs/GaSb SLS detectors, the physical dimensions of the device are defined by mechanical termination of the InAs/GaSb crystal lattice (refer to Appendix A for complete processing details). The structure so defined is universally addressed as a "mesa". This process exposes the sidewalls of the structure comprising of alternating layers of InAs and GaSb along with very thin layers of InSb and GaAs. The thicknesses of InSb and GaAs layers are commonly assumed to be approximately a monolayer (ML) [81] and hence the thicknesses of InAs and GaSb layers can get to be in the order of tens of MLs each. The exposed layers comprising of their abruptly terminated crystal lattice made up of millions of dangling bonds. These dangling chemical bonds react with the oxygen molecules in the active atmosphere and water (during fabrication process) to form native oxides. This chapter details on definition of InAs/GaSb SLS device sidewalls free of native oxides, surface defects and impurities by various chemical and or mechanical treatments before the passivation layer and contact metals are applied.

4.1 Surface Etching

The word ``etch´´can be defined as to cut, bite or corrode with an acid or the like. This technique has existed since 1827 when Parisian engraver Lemaitre made an etched copy of an engraving of Cardinal d'Amboise by placing a glass plate coated with bitumen mixed with lavender oil (acting as a mask), in strong acid [66]. In terms of microfabrication ``etching´´is not only considered as a process to sculpt desired three dimensional shapes or structures on a substrate but also used as a process of chemically removing layers from a substrate or surface.

A surface is well prepared to naked eye when the applied treatments results in no abrasions, cuts or physical damages. But we are also looking for etchants that remove organic contaminants, native oxides and hopefully chemically terminate free dangling bonds. Good etchant should perform the following functions:

1. Smooth the surface layer damaged by thinning/polishing, cleaving/cutting processes.
2. Minimize the presence of native oxides and hence able to control the surface recombination velocity.
3. Reveal least amount of surface defects and low index planes.
4. Remove the surface layer containing organic contaminants.

The choice of the etching process depends on the composition of the semiconductor material being etched and its intended result. The most common etching processes are listed below.

1. Polishing/Thinning/Smoothing Process

   Polishing is a homogeneous semiconductor material removal process that often results in a mirror-like shining surface. This process can be used to remove large amounts (in microns) of semiconductor material or can be used to just finish the surface with a smooth mirror-like surface.

2. Wet Chemical Etching

   Wet chemical etching is a controlled dissolution of a solid like a crystal lattice in a reactive solvent by breaking of covalent bonds with no mechanical force. This process can take place at room or elevated temperature. The most favorable characteristic of wet chemical etches is the ability to cause minimal surface damage. Wet chemical etches are also known to perform chemical selectivity, crystallographic etching and can be tailored to various material compositions. Wet chemical etches are usually isotropic processes with the unavoidable tendency to undercut masks hence making precise dimensional control difficult.

3. Dry Chemical/Mechanical etching

   Dry etching covers a gamut of family of methods by which a solid material is etched such as in gas or vapor phase, physically by ion bombardment, chemically by chemical reaction through a reactive species or by combined physical and chemical mechanisms [66]. In device fabrication processes, dry chemical etching when compared to wet chemical etching, is considered to provide greater repeatability, higher aspect ratios, more anisotropic profiles (straighter edges), improved uniformity, and improved control over etch depth. In our work, we utilized the dry etch technique of Inductively Coupled Plasma (ICP) system. In this technique the plasma is driven inductively with a power source operating at standard 13.56MHz in an ICP source. These ICP source creates low-pressure, high-density, low-energy plasmas by coupling ion-producing electrons to the magnetic field arising from the RF voltage [66]. Moreover, the plasma in this etching chamber is shielded from the electric field of the RF to avoid capacitive coupling, which tends to create higher energy ions.

4. Electrolytic Etching

   In the electrolytic etch process, the etch material is placed on the anode which along with an inert cathode (commonly Pt), are dipped in an appropriate electrolyte [38]. It has to be noted that the products of the reaction must be soluble in the electrolyte and also the electrolyte must have enough electrical conductivity.

In this dissertation, during the fabrication of InAs/GaSb SLS detectors, we implement two distinctly different methods of defining the physical dimensions of the device (the mesa structure). These are (a) Chemical Wet etch treatments (b) Dry etch treatments using both chemical and mechanical means. Both techniques lead to the termination of the crystal lattice, hence it is essential for us to systematically look into effects of these techniques.

4.2 Etch of Constituent SLS Layers

Fabrication of InAs/GaSb SLS-based detectors involves definition of the physical dimensions of the device, which results in exposure of its sidewalls. These sidewalls are composed of InAs, GaSb, and, in part, InSb and GaAs layers. Since the thickness of InSb and GaAs layers in SLS are commonly assumed to be approximately one ML and the thicknesses of InAs and GaSb layers are on the order of tens of MLs, the optimization of InAs and GaSb etches is critical to SLS detector performance.

4.2.1 Etch Mechanism of GaSb

As explained in chapter 3, GaSb surface exposed to air will form native oxide layer consisting of Ga_2O_3 and a small percentage of elemental Sb and even a small percentage of elemental Sb is sufficient to drastically increase the surface recombination velocity and surface leakage [28].Since oxidation of GaSb plays such a crucial role in the device performance along with the fact that GaSb oxidizes more rapidly and aggressively than InAs, it becomes essential to reduce the formation of native oxides of GaSb. Furthermore InAs/GaSb superlattice structure are usually grown on GaSb substrates, and after hybridization of the fabricated FPA to the ROIC, the GaSb substrate has to be removed. This is performed in order to reduce substrate scattering and interference as FPAs are back illuminated devices. Hence etching study on GaSb material is given significance in this study.

To break the mixed covalent-ionic bonds in GaSb, an oxidizing agent is required. The conventionally used oxidizing agents are hydrogen peroxide (H_2O_2) and nitric acid (HNO_3), due to their controllable etch rates, purity and mode of attack [31]. Even though tervalent antimony can exist in strong acid solutions, it can easily hydrolyze into antimonyl ions which when diluted can precipitate as antimonyl oxy-salts. When GaSb is attacked by strong oxidizing agents, it forms insoluble trioxide (Sb_2O_3) or pentoxide (Sb_2O_5). Hence to keep antimony in soluble form, a complexing agent such as hydrochloric acid (HCl), hydrofluoric acid (HF) or carboxylic acid (e.g. Tartaric acid, citric acid, and lactic acid) is required. Furthermore, the addition of a complexing agent does not interfere with the dissolution of group IIIs such as aluminum, gallium or indium.

It has to be taken into account that a optimized solution composition is critical for the intended surface morphology and for control of the reaction/etch rate. Take in to account the ratio of HNO_3 to HCl; if it is very large, then insoluble antimony oxides Sb_2O_3 or Sb_2O_5 is formed. When the HCl content is large, then highly insoluble $SbCl_3$ is formed. It has to also be noted that the ratios of organic complexing agents are restricted as strongly acidic solutions tend to suppress the ionization of the organic acids, which is critical for them to act as complexing agents. For that reason the ratio of organic acid to HNO_3 must favor the organic acids.

Another factor to be taken into account while etching is the polar nature of III-V compounds as the etch rates on (111)A and (111)B planes are different. It has been observed [35] that the etchant HNO_3: tartaric acid attacks the antimony face of GaSb more rapidly than the gallium face.

4.2.2 Etch Mechanism of InAs

Unlike the antimonides which tend to form insoluble oxides or oxyhydroxides, arsenides tend to form soluble arsenic acid ($HAsO_4$) with strong oxidizing agents. In the case of InAs etching, that arsenic in solution forms anions in the presence of oxidizing agents such as H_2O_2 i.e. AsO_3(3-) and AsO_4(3-) (arsenite and arsenate ions respectively) wherein the dissolved products in the $HCl+H_2O_2+H_2O$ solution are $InCl_3+H_3AsO_3$ (or H_3AsO_4 at higher H_2O_2 concentration). In case of GaSb, Sb forms only cations, thus $SbCl_3$ or $SbCl_5$ along with $GaCl_3$ are the dissolved products.

The difference in covalent potential of Ga, Sb, In and As atoms in GaSb and InAs crystals is 1.295 and 2.154, respectively [47]. Thus, the ionicity of covalent bonds is higher in InAs rather than in GaSb, resulting in higher reactivity of InAs in certain etchants and hence explaining its faster etch rates.

4.3 Development of Optimized Etch for GaSb and InAs

Optimization of wet chemical etch for GaSb was performed on double-side polished Te-doped (n = 10^{17}cm^{-3}) GaSb (100) substrate with thickness of 525 μm. The substrate was then subjected to various different etch schemes listed in Table 4.1 along with their optimized solution composition, average etch rates, surface morphology and root mean square (RMS) roughnesses. It has to be noted that all etches were carried out at 20C in a cleanroom environment. An Alpha step profilometer was utilized to measure the etch depths (in μm) after each etch and then the etch rates (in μm/min) were calculated. The RMS surface roughness of

Table 4.1: Summary of the chemical etch experiments on GaSb substrate, in order of improving surface quality.

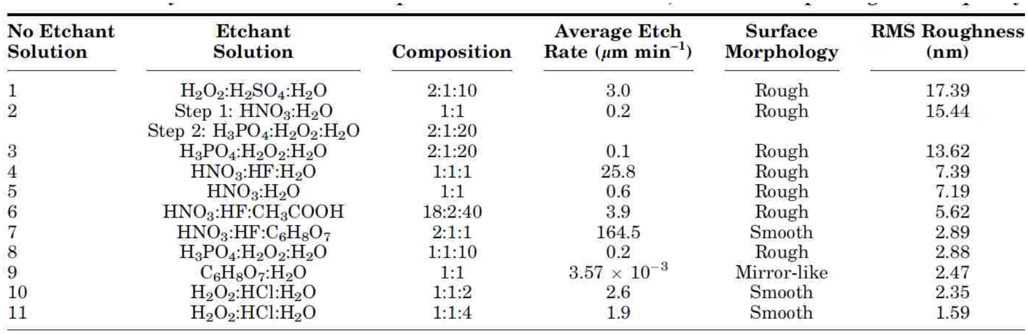

No Etchant Solution	Etchant Solution	Composition	Average Etch Rate (μm min^{-1})	Surface Morphology	RMS Roughness (nm)
1	H_2O_2:H_2SO_4:H_2O	2:1:10	3.0	Rough	17.39
2	Step 1: HNO_3:H_2O	1:1	0.2	Rough	15.44
	Step 2: H_3PO_4:H_2O_2:H_2O	2:1:20			
3	H_3PO_4:H_2O_2:H_2O	2:1:20	0.1	Rough	13.62
4	HNO_3:HF:H_2O	1:1:1	25.8	Rough	7.39
5	HNO_3:H_2O	1:1	0.6	Rough	7.19
6	HNO_3:HF:CH_3COOH	18:2:40	3.9	Rough	5.62
7	HNO_3:HF:$C_6H_8O_7$	2:1:1	164.5	Smooth	2.89
8	H_3PO_4:H_2O_2:H_2O	1:1:10	0.2	Rough	2.88
9	$C_6H_8O_7$:H_2O	1:1	3.57×10^{-3}	Mirror-like	2.47
10	H_2O_2:HCl:H_2O	1:1:2	2.6	Smooth	2.35
11	H_2O_2:HCl:H_2O	1:1:4	1.9	Smooth	1.59

each etched substrate was estimated by atomic force microscopy (AFM) on an area 1 μm x 1μm. The surface morphology simply recounts the state of the substrate after each etch. Etch depth versus etch time for various etch solutions on GaSb substrates are presented in figure 4.1.

Of all the wet chemical etches we carried out, as stated in Table 4.1, the highest RMS surface roughness of 17.39 nm was observed with H_2O_2:H_2SO_4:H_2O (2:1:10) solution as etchant. In this mixture, it is the oxidizing agent H_2O_2 that breaks the mixed covalent-ionic bonds of GaSb surface structure and then the H_2SO_4 dissolves the oxides formed. H_2O works as the neutralizer that not only helps control the etch rate but also later forms an oxide layer on the etched surface. It has to be stated that the thickness of this oxide layer depends on the pH of the solution which in turn is determined by the H_2SO_4:H_2O_2 ratio. The rapid etch rate of 2.98 μm/min may be attributed for the highly rough surface morphology of this experiment.

The lowest RMS surface roughness of 2.47 nm and lowest average etch rate of 3.27 x 10^{-3} μm/min was seen when citric acid ($C_6H_8O_7$):H_2O (1:1) was used as the etchant. This indicates that diluted citric acid barely etched the GaSb surface. The HNO_3: HF: H_2O (1:1:1) solution on GaSb resulted in a rough surface with

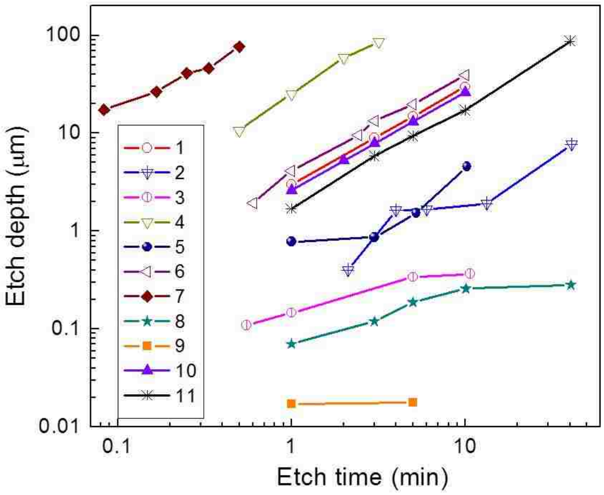

Figure 4.1: Etch depth versus etch time for various etch solutions on GaSb substrates.

RMS roughness of 7.39 nm and a surface without the appearance of etch pits. The HNO_3:HF:CH_3COOH (acetic acid) (18:2:40) solution [36] exhibited a surface roughness of 5.62 nm and a moderate etch rate. Among all the etchants, the HNO_3:HF:$C_6H_8O_7$ (2:1:1) had the fastest etching rate with a smooth surface (RMS roughness of 2.89 nm). It has to be noted that the latter solution would be ideal for GaSb substrate removal in LWIR FPA processing due to its rapid etch rate and smooth after-etch surface.

Various research groups [93] have reported the utilization of phosphoric acid (H_3PO_4) based solutions for etching of GaSb and GaSb-based structures. As seen in Table 4.1, we developed several etch chemistries containing H_3PO_4 acid. The smoothest surface among them was obtained using H_3PO_4:H_2O_2:H_2O (1:1:10) solution with RMS roughness of 2.88 nm. In the aforementioned solution, when GaSb reacts with H_3PO_4, it results in $Sb(H_2PO_4)_3$ and $Ga(H_2PO_4)_3$ which further oxidizes to $Sb(H_2PO_4)_5$ along with $Ga(H_2PO_4)_3$ in the strong acid medium containing H_2O_2. Since gallium does not react with H_2O_2, $Ga(H_2PO_4)_3$ remains stable. Then $Sb(H_2PO_4)_5$ further reacts to form $Sb_2(HPO_4)_5$ and $Sb_3(PO_4)_5$ and this is due to increased pH during cleaning in H_2O. Both $Sb_2(HPO_4)_5$ and $Sb_3(PO_4)_5$ being highly insoluble, leave behind considerable amount of debris on the etched surface, causing roughness that is undesirable for device fabrication.

Among all etches investigated, H_2O_2:HCl:H_2O (1:1:2) etch solution has demonstrated the smoothest etched surface (RMS roughness of 2.35 nm) along with a etch rate of approx. 2.62 μm/ min. It is the only etchant that revealed etch pits with etch pit density (EPD) to be 2.7 x 10^3 etch pits/cm^2 which is comparable to the results reported by Heinz [47]. It may be due to the coalescing of adjacent defects that these oval shaped etch pits are formed. The reaction with GaSb may take place as follows:

$$6HCl + GaSb \longrightarrow GaCl_3 + SbCl_3 + 3H_2 \tag{4.1}$$

It has to be noted that $GaCl_3$ may remain as Ga^{3+} ions, which do not oxidize. Once again, we have to take into account the fact that H_2O_2 does not react with gallium. In presence of HCl + H_2O_2, the continued exposure of GaSb surface in the etchant can lead to Sb-tri-chloride further oxidizing as:

$$2HCl + H_2O_2 + SbCl_3 \longrightarrow SbCl_5 + 2H_2O \tag{4.2}$$

The etch product $SbCl_5$ + $2H_2O$ will then lead to form $SbO(OH)_3$ or $SbO_2(OH)$ which are both insoluble, but can be dissolved in organic complexing agents like citric acid to further form soluble complexes, resulting in smoother surfaces. In order to slow down etch rate for better control of etch dimensions, we further diluted H_2O_2:HCl:H_2O (1:1:4), resulting in a etch-rate of 1.88 μm/min and RMS surface roughness equal to 1.59 nm.

The stoichiometric reaction of the H_2O_2:HCl:H_2O (1:1:4) with InAs substrate under weaker oxidizing conditions (i.e. lower H_2O_2 concentration) is represented as

$$InAs + 3HCl + 3H_2O_2 \longrightarrow InCl_3 + H_3AsO_3 + 3H_2O \tag{4.3}$$

Now under stronger oxidizing conditions (i.e. higher H_2O_2 concentration) this stoichiometric reaction will take the form of

$$InAs + 3HCl + 4H_2O_2 \longrightarrow InCl_3 + H_3AsO_4 + 4H_2O \tag{4.4}$$

The formed reaction/etchant products namely, arsenous acid (H_3AsO_3), arsenic acid (H_3AsO_4), and $InCl_3$ are all water soluble.

In our quest to optimize the ideal etch on InAs/GaSb SLS structures, we utilized an InAs substrate and subjected it to the previously optimized solution of H_2O_2:HCl:H_2O (1:1:4). The AFM images of both InAs and GaSb substrates treated with H_2O_2:HCl:H_2O (1:1:4) is shown in Figs 4.2 and 4.3. The experiment revealed that the average etch rate of InAs substrate in the solution is 0.64 μm/min with a RMS surface roughness of 22 nm, whereas a GaSb substrate treated with the same solution showed an average etch rate of 1.9 μm/min with a RMS surface roughness of 1.59 nm. This implies that the optimized etch of H_2O_2:HCl:H_2O (1:1:4) solution is rougher on InAs than GaSb, but the etch rate is faster in GaSb substrate.

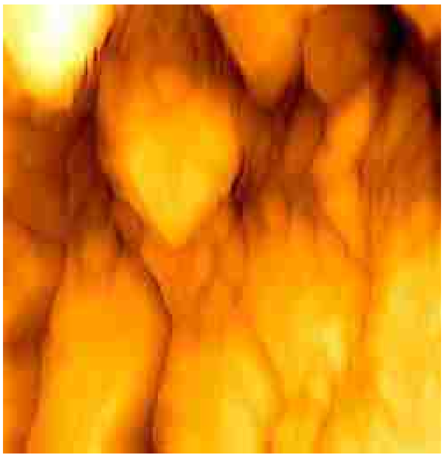

Figure 4.2: AFM image on 1 μm x 1 μm area of InAs substrate etched with H_2O_2:HCl:H_2O (1:1:4) solution.

4.4 Etching of InAs/GaSb SLS Detectors

During the fabrication process of InAs/GaSb SLS detectors (as described in Appendix A), the definition of the mesa structure is usually the first and crucial step.

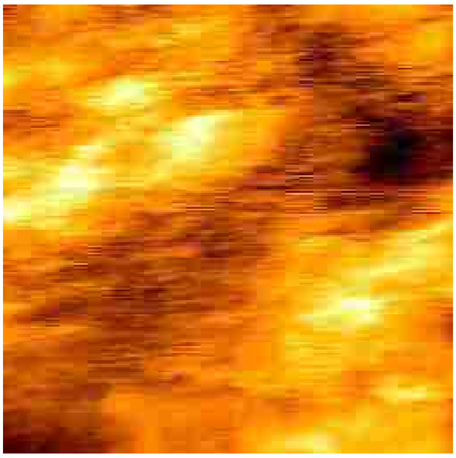

Figure 4.3: AFM image on 1 μm x 1 μm area of GaSb substrate etched with H_2O_2:HCl:H_2O (1:1:4) solution.

Along with all the characteristics listed in section 4.1, the mesa definition etch techniques must fulfill the following criteria:

1. the resulting etched mesa structure must exhibit smooth sidewalls with no etch remnants;
2. the etched mesa structure must exhibit no lateral etching (as lateral etching on any side of the mesa sidewall can lead to the mishap of the intended mesa pattern which is crucial for the next step of metal contact pattern in detector fabrication;
3. the etch technique must possess a controllable etch rate, hence we have a less chance of overshooting intended etch depths;
4. the etch technique must not etch photoresist (PR) mask, as if the PR is etched away then our pattern is etched away resulting in a obscure mesa structure.

Nowadays, high-density plasma etch processes are commonly utilized for InAs/GaSb SLS material in spite of the inevitable degradation of sidewall surface electronic properties due to ion bombardment or unwanted deposition of etch by-products [96, 52, 61, 53]. Plasma chemistry usually consists of chlorine-based precursors (BCl_3, Cl_2 or $SiCl_4$) due to high volatilities of gallium, indium, antimony and arsenic chlorides providing fast etch rates and smooth morphologies [95]. The resulting etch profiles are vertical due to the plasma sheath and the ionized gas directionality. Damage produced during the dry etch may be partially restored by subsequent chemical treatment [73]. Due to the ability of wet etches to cause virtually no surface electronic damage, a chemical etch attracts attention of researchers for single-pixel SLS device fabrication. However, the isotropic nature of wet etch process resulting in concave sidewall profile and an unavoidable tendency to undercut etch masks making precise dimensional control more difficult and stipulates limited application of wet etches for SLS FPA fabrication.

Utilization of wet chemical etch process for fabrication of large area single pixel SLS detectors has been reported by various research groups (MWIR detectors [21, 20, 23] and LWIR detectors [23, 29]). The choice of the appropriate wet chemical solution is complicated by dissimilar chemical properties of InAs and GaSb causing the preferential etch of either compound in SLS stack resulting in the formation of ripples on the devices sidewalls, acting as an additional source for electrical active sites [126].

Chaghi et al [21] compared different chemical solutions based on orthophosphoric (H_3PO_4) acid employed for fabrication of SLS detectors with cut-off wavelength of 4.9 μm at 80K. Detector processed with $H_3PO_4/H_2O_2/H_2O/C_6H_8O_7$ (citric acid) followed by a second immersion in $NaClO : H_2O$ showed the best performance with R_0A of 1.6×10^5 Ω cm^2.

320 x 256 LWIR ($\lambda_{100\%}$ = 10 μm at 77K) FPA with 30 μm pitch fabricated by wet etch technique was demonstrated by QmagiQ [121], with dark current density of upto 2×10^4 A/cm^2 (77 K) at 0.3 V bias. Despite the relatively high dark current density the NEDT had acceptably low values mainly due to the high quantum efficiency (45% at 0.3V), a key finding for SLS FPA viability.

Inductively coupled plasma (ICP) etch with chlorine-based chemistry was employed by Ngyuen et al. [76] for pixel isolation of SLS LWIR ($\lambda_{50\%}$ = 10.3 μm at 77K) detectors. Four samples with different etch conditions were studied: a $C_4H_6O_6 : H_3PO_4 : H_2O_2 : H_2O$ wet etch followed by a citric clean-up dip (sample A); a BCl_3-Ar dry etch followed by a citric clean-up dip (sample B); a CH_4-H_2-Ar plasma (sample C); and a $BCl_3 - Cl_2 - CH_4 - H_2 - Ar$ plasma (sample D). Vertical ripples on the sidewalls, and also a significant amount of undercut with sidewalls sloped at an angle of 54.9° was observed for sample A. The preferential etching in samples B and C has resulted in waffle-like pattern observed in the plane of the mesa. In addition, the indium droplets on the sidewalls of sample B were due to the low volatility of InCl$_x$. This effect may be compromised by using higher etch temperatures and increased ion energy values. However, it would result in increased amount of sputtering and more pronounced preferential etching. Sample D exhibited smooth sidewalls with no preferential etching, inferred from the lack of the waffle-like pattern, or indium residuals. The amount of surface leakage provided by each investigated etch scheme was characterized by the size-dependent effective resistance-area product, RA_{eff}. Samples A (wet etch) and D ($BCl_3 - Cl_2 - CH_4 - H_2 - Ar$ plasma etch) showed relatively flat behavior compared to the other samples, with a surface resistivity that is at least 7.4 times higher. Combination of chlorine- and methane-based etches resulted in electrical device performance comparable to the wet etched samples. Moreover, near-vertical, smooth sidewalls with minimal dielectric mask erosion were achieved with good anisotropy resulting in more than three times higher fill factor.

The electron cyclotron resonance (ECR)-reactive ion etching is alternative high density plasma approach of InAs/GaSb SLS mesa definition. Huang et al. [53] compared electrical performance of LWIR ($\lambda_{50\%}$ = 9.3 μm at 77K) InAs/GaSb SLS detectors fabricated with ICP and ECR etching techniques. Both processes were based on $BCl_3 : Ar$ chemistry, for protection of etched sidewalls. SiO_2 and polyimide were utilized separately. The ECR process was followed by citric acid-based wet etch to remove plasma induced surface damage. Detector etched by ICP with sidewalls encapsulated by polyimide has demonstrated the highest surface resistivity ($6.7\times 10^4\ \Omega\cdot cm$) among four treatments. Comparison of electrical performance of detectors etched with ECR and ICP with the same post-etch encapsulation method (polyimide) revealed an order of magnitude lower dark current density for ICP-polyimide sample. This is attributed to the better surface conditions prior passivation achieving by ICP.

Figure 4.4: Heterostructure schematic of InAs/GaSb SLS LWIR detector with pin design.

4.5 Mesa Definition of InAs/GaSb SLS Single-Pixel Detector

We incorporated the optimized etch scheme (H_2O_2:HCl:H_2O (1:1:4)) into the fabrication process of InAs/GaSb SLS LWIR single-pixel photodetectors. Detector structures were grown on n-type (Te-doped) GaSb (100) epi-ready substrates by molecular beam epitaxy using a solid-source VG-80 reactor equipped with valved cracker sources for group V Sb_2 and As_2 fluxes and Ga/In SUMO®cells. The detector structure consisted of a 2.1 μm -thick absorbing region formed by 16 ML InAs/0.8 ML InSb/6 ML GaSb SLS grown on top of a 0.45 μm-thick SLS bottom contact n-region (4.0 x 10^{18} cm^{-3}) formed by SLS with the same composition and thickness. The structure was capped by a 50-nm-thick GaSb p-type layer (4.0 x 10^{18} cm^{-3}). The top and bottom 50 periods of the absorber region were doped p- and n-type, respectively, with a doping concentration of 1.0 x 10^{17} cm^{-3} to improve transport of photogenerated carriers. The heterostructure schematic of the detector is shown in Fig. 4.4.

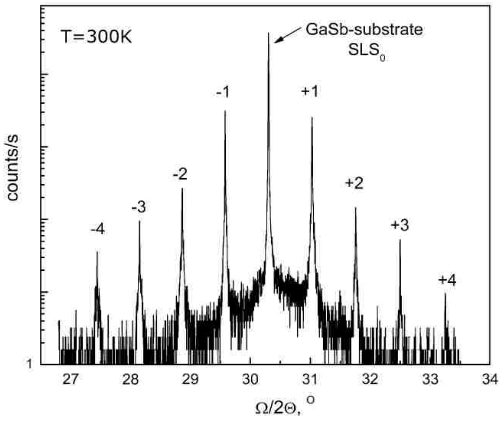

Figure 4.5: HRXRD spectrum of the InAs/GaSb SLS LWIR pin detector near GaSb (004) reflection.

The structural quality of the detector was assessed by high-resolution x-ray diffraction (HRXRD). The HRXRD setup comprised a Philips double-crystal x-ray diffractometer using the Cu-Ka1 line, and all measurements were carried out at 300 K. The HRXRD spectrum of the InAs/GaSb SLS LWIR pin detector near GaSb (004) reflection is shown in Fig. 4.5. The lattice mismatch of the SLS to the GaSb substrate is very close to zero. Low lattice mismatch enables growth of superlattice (SL) diodes with a large number of periods without degrading quality. Furthermore, observation of the sample surface by Nomarski microscope reveals good surface quality without growth defects. The full-width at half-maximum (FWHM) of the first-order satellite peak of SLS is found to be 31 arcsec, and the presence of four orders of SLS satellite peaks indicates very good crystalline quality of the material. The measured period was equal to 7.01 nm , which is slightly larger than the nominal value (6.95 nm). We attribute this to the deviation of the InSb interface thickness from its intended value.

The material was processed as normal incidence single-pixel detectors with

400 μm x 400 μm mesa area and apertures ranging from 20 μm to 300 μm in diameter. Processing was initiated by material patterning for the mesa definition using a standard optical photolithography technique with 4330 photoresist. Then, three different methods were utilized for diode mesa definition: (a) inductively coupled plasma (ICP) etch with BCl_3 gas, (b) HCl-based chemical etch, and (c) a combination of plasma assisted BCl_3-based and HCl-based chemical etches. In each case, material was etched to the middle of the bottom contact layer (etch depth 2.3 μm). However, in (c), material was first dry etched to the middle of the absorbing layer (etch depth 1.2 μm) followed by the wet chemical etch to reach 2.3 μm. A PlasmaTherm SLR 770 ICP Chlorine Etcher with an ICP power of 499 W, average radio frequency (RF) power of 156 W, pressure of 3.2 mtorr, directcurrent (DC) bias of 252 V, and BCl_3 flow of 30.2 sccm at a temperature of 25C was utilized for the dry etch. The ICP etch rate of the GaSb substrate alone was found to be 0.267 μm min. Etch rates for the plasma-assisted and chemical etch of the LWIR structure were 0.2173 μm/ min and 0.39 μm/min, respectively. Ti/Pt/Au (50 nm /50 nm/300 nm) was used as contact metals for both top and bottom contact metallization. A three-dimensional (3D) schematic of a processed single-pixel detector is shown in Fig. 4.6.

The 50% cutoff wavelength of processed devices was defined through spectral response measurements performed with a glow-bar source in the Fourier-transform infrared spectrometer and was found to be 14 μm at 30 K (at bias of 0 V). Fig. 4.7 shows normalized spectral response from a 300 μm diameter device at T = 30 K.

Fig. 4.8 shows scanning electron micrograph (SEM) images of 400 μm x 400 μm mesa of InAs/GaSb SLS LWIR detectors obtained after (a) plasma-assisted etch, (b) optimized chemical etch (H_2O_2:HCl:H_2O = 1:1:4), and (c) combination of both. Whereas the plasma-assisted etch is expected to be an anisotropic process

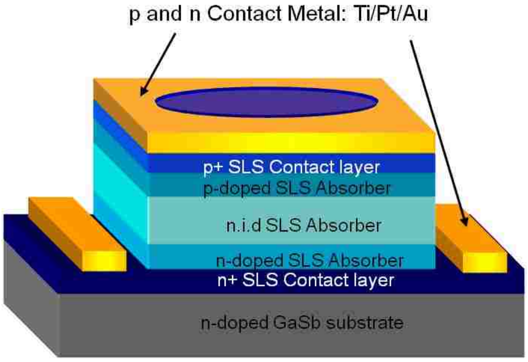

Figure 4.6: Three-dimensional view of a processed InAs/GaSb SLS LWIR pin detector.

and provide well-defined vertical sidewalls, we observed a two-step etch profile (Fig. 4.8a) for devices etched with BCl_3 plasma. Moreover, numerous etch residues were noticed on the mesa sidewalls and planar surfaces of etched terrace and bottom contact layer. Devices etched with optimized HCl-based chemical etch (Fig. 4.8b) resulted in the expected undercut profile (inset to Fig. 4.8b) with clean sidewalls free of any etch remnants. This undercut was estimated to 5 μm on

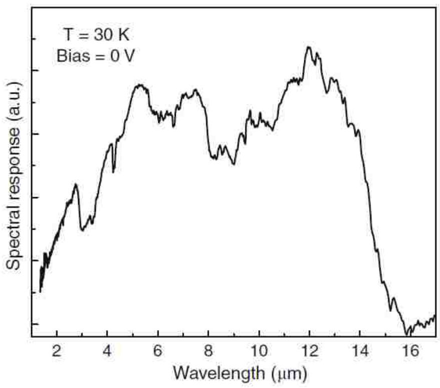

Figure 4.7: Spectral response from a 300 μm-diameter device at 30 K and V_b = 0 V.

each mesa side. Formation of etch pits was observed only on the planar surface of bottom contact and not on etched sidewalls. Removal of damage (etch residues and two-step sidewall profile) induced by the plasma-assisted etch was observed for devices etched with the combination of BCl_3 and optimized HCl-based chemical etch (Fig. 4.8c). However, sidewalls were rough with clear formation of ripples. In addition, the surface near the base of the etched mesas was heavily degraded, with width of the damaged region of 3 μm.

4.6 Mesa Delineation of InAs/GaSb SLS Focal Plane Array

Focal Plane Arrays (FPAs) are high performance detectors with a slightly more complex fabrication process than single-pixel devices. One of the distinguishing factors of FPAs from single pixels is that FPAs have smaller mesa areas of 24 μm x 24 μm. Typical FPA fabrication process involves the following steps: the individual pixel isolation and passivation; contact metalization followed by the under bump metal (UBM) deposition; bump metal (indium) deposition; reflow process, hybridization of FPA to the read-out integrated circuit (ROIC) and the substrate removal. There is an increased emphasis on large format (1M-4M) FPAs in which the pixel size is further shrunk to 15 μm x 15 μm. Appendix B outlines the detailed FPA fabrication procedure.

Just as in the case of single-pixel processing, during the individual pixel isolation process by mesa etching, the periodic nature of the idealized crystal structure of the superlattice is ended abruptly leading to the formation of allowed electronic quantum states within the energy band gap of the SLS resulting in large surface leakage currents. Furthermore, possessing a pristine device surface after mesa etch plays a more crucial role in FPA fabrication due to the smaller size of each pixel and hence more pronounced the effect of each impurity and defect would wield. Additionally, the mesa etching is the first step in FPA fabrication and hence preparation of a good surface forms a solid foundation to the multitude of processing steps to follow.

The dry-plasma assisted etching has to be the most prevalently [21, 26, 52] used mesa etch technique in FPA fabrication despite the inevitable degradation of sidewall surface properties due to ion bombardment or deposition of unwanted etch byproducts. Damages produced during dry plasma-assisted etches can be restored to some extent by subsequent chemical treatment [72, 61].

Wet chemical etching is commonly an isotropic process and is usually thought to be incompatible with the current format of fabrication of high-fill factor large-format FPAs based on InAs/GaSb SLS. The question of its incompatibility mainly arises due the tendency of wet etches to undercut mask dimensions and due to the difficulty in controlling their etch rates.

In Section 4.5 we studied the surface of 400 μm x 400 μm etched mesa sidewalls of InAs/GaSb LWIR (with 50% cut-off wavelength of 14 μm) detectors after conventional BCl_3-based plasma-assisted etch, optimized chemical etch (H_2O_2:HCl:H_2O = 1 : 1 : 4) and the combination of both etches. We found that the smoothest sidewall profile with reasonable undercut was obtained after wet chemical etch alone. Here we extend our work performed on single element SLS LWIR detectors with large mesa size to small size pixels used in the FPAs based on the same LWIR SLS material.

The FPA mask is so designed that each single pixel in the 320 x 256 array has a mesa area of 24 μm x 24 μm with the distance between the neighboring pixels being 6 μm. The pattern was laid on the InAs/GaSb SLS LWIR with PR4330 utilizing standard UV photolithography process. The sample was then etched with the wet chemical etch H_2O_2:HCl:H_2O (1:1:4) solution to the intended etch depth of approx. 2.3 μm (the middle of the bottom contact) and the etch rate was found to be 0.67 μm/min. The resulting etch profile is shown in Fig. 4.9 (a).

A significant lateral etch of 9 μm was observed, which is large enough to disrupt further FPA processing and hence rendering this particular etch scheme not suitable for FPA fabrication. In order to slow down the etch rate for better control of etch dimensions, we diluted the solution to H_2O_2:HCl:H_2O (1:1:10). The resulting etch-rate was found to be 0.40 μm/min and resulted sidewall profile is shown in Figure 4.8 (b). Here the lateral etch of 5.5 μm, which is less pronounced than previous experiment, but yet etches 5% of the FPA mesa area and the sidewalls were observed to be rough. The unsatisfying results in terms of desired surface properties and physical dimensions, from the HCl-based etches motivated us to try several other etchant solutions.

Citric Acid ($C_6H_8O_7$) based etchant solution has been reported in literature [73] in the fabrication of InAs/GaSb SLS FPAs. We etched our InAs/GaSb SLS LWIR material with H_3PO_4+H_2O+ citric acid (1:1:3) resulting in an etch rate of 0.68 μm/min and the sidewall profile, as seen in Fig. 4.8 (c), shows a considerable lateral etch of 10 μm resulting in symmetrical pyramid shape of the etched mesas. With such disappointing results again, we moved on to utilizing H_3PO_4+H_2O_2+H_2O (2:1:20) solution to etch our InAs/GaSb SLS LWIR material resulting in a rough looking etched surface illustrated in Fig. 4.8 (d). It exhibited an etch rate of 0.13 μm/min and a lateral etch of 1 μm, hence ceding to be undesirable for FPA device fabrication.

Analyzing the performances of the four wet chemical etch techniques described above, we concluded that wet chemical etch by itself may not be sufficient to give us pristine mesa etched surfaces along with intact physical dimensions in a tightly packed FPAs with 24 μm x 24 μm mesa area each. Furthermore, to investigate which material is responsible for the wet chemical etches resulting in such huge lateral etches and rough surface in SLS structure, we looked into the constituent compounds of InAs and GaSb individually. Firstly, we defined 24 μm x 24 μm square pixels with pitch size of 30 μm on (a) n-type (n= 4 x 10^{16} cm^{-3}) InAs (100) and (b) n-type (n = 5 x 10^{17} cm^{-3}) GaSb (100), both double side polished substrates with thickness of 525 μm. We then subjected these structures to the optimized wet chemical etch H_2O_2:HCl:H_2O (1:1:4) solution. The results are illustrated in the Fig. 4.10 (a) for InAs and Fig. 4.10 (d) for GaSb substrates. We observed that the undercut was 3 times lager in InAs (lateral etch on each mesa side 6 μm) than in GaSb substrates (lateral etch on each mesa side 2 μm). Subjected to the wet chemical etch H_2O_2:HCl:H_2O (1:1:4) solution for 1 minute, InAs showed a RMS roughness of 22 nm where as GaSb showed RMS roughness 1.49 nm.

The next set of samples underwent plasma-assisted etch performed on a PlasmaTherm SLS 770 ICP chlorine etcher. It must be noted that the sample was physically clamped to the loading substrate electrode/carrier by means of conduction paste in order to reduce lateral etching [45].The temperature of 25C was maintained in the etch chamber by the flow of He to the backside of the wafer. The resulted etch structures look smooth and well defines vertical sidewalls free of etch remnants as shown in Fig. 4.10 (b) for GaSb and (e) InAs substrates.

Now let us take into account the etch rates of our materials as seen in Table. 4.2. The etch rate of the ICP-BCl_3 based etch on InAs/GaSb SLS LWIR material was found to be 0.22 μm/min whereas for chemical etch with H_2O_2:HCl:H_2O (1:1:4) solution was 0.39 μm/min. On GaSb substrate, the ICP-BCl_3 based etch showed an etch rate of 0.28 μm/min whereas the chemical etch with H_2O_2:HCl:H_2O (1:1:4) solution was 1.9 μm/min. Additionally on InAs substrate, the ICP-BCl_3 based etch showed an etch rate of 0.13 μm/min whereas for chemical etch with H_2O_2:HCl:H_2O

Table 4.2: Comparison of etch rates (units: μm/min) in SLSs, InAs and GaSb substrates.

Etch Technique	SLSs	InAs	GaSb
Dry Etch	0.22	0.13	0.28
Optimzed Wet Etch	0.39	0.64	1.9

(1:1:4) solution was 0.64 μm/min.

Under the wet chemical etch with H_2O_2:HCl:H_2O (1:1:4) solution, the InAs/GaSb SLS material does not behave neither as InAs nor as GaSb, but under ICP-BCl_3 based etch it's etch rate was closer to GaSb than InAs. But the 16ML InAs/0.8ML InSb/6 ML GaSb SLS structure has more InAs content per period than GaSb. The applicability would be while performing calibration processes of SL in IC BCl_3 based etches, GaSb can be used as a reliable substitute material.

The third set of samples we put through the combination etch consisting of both dry ICP-BCl_3 based etch and wet chemical etch using the H_2O_2:HCl:H_2O (1:1:4) solution. InAs substrate with FPA mesa pattern after the combinational etch is shown in Fig. 4.10 (c) and it demonstrates rough planar etched surface of FPA grooves along with two step mesa sidewall profile due to the lateral etch. On GaSb substrate (Fig. 4.10 (f)) we observed the formation of etch pits on the sidewalls of mesas defined with the combinational etch. It must be noted that the etch depth was measured utilizing Alpha Step profilometer and was kept around 2.5 μm for the all etches thus resembling the typical etch depth of LWIR SLS detector. For the combination of plasma-assisted and the optimized HCl based chemical etches the dry etch depth was 1.3 μm and the rest of the 1.2 μm was etched with the wet chemical etch using the H_2O_2:HCl:H_2O (1:1:4) solution.

Fig. 4.11 displays SEM images of InAs/GaSb SLS LWIR FPA with 30 μm pitch obtained after (a) combination of consisting of both dry ICP-BCl_3 based etch and wet chemical etch using the H_2O_2:HCl:H_2O (1:1:4) solution and (b) ICP etch only. Insets of Fig. 4.11 depict the sidewall profiles of 24 μm x 24 μm FPA mesas. We observe that the application of chemical etch subsequent to the plasma-assisted etch (Fig. 4.11 (a)) resulted in undercut 8 μm on each side of FPA mesa. Hence the final size of defined mesa area is only 8 μm x 8 μm which is not acceptable for the subsequent FPA fabrication steps. InAs/GaSb SLS LWIR FPA etched with the ICP etch only demonstrated the expected smooth vertical sidewalls free from any etch residuals with clean FPA grooves as show in Fig. 4.11 (b). Thus reestablishing that the anointed ICP etch alone is the acceptable technique to create small dimensional mesa structure during the fabrication of high fill factor FPA based on InAs/GaSb SLS LWIR material.

4.7 Conclusions

We have examined the surface of etched mesa sidewalls of InAs/GaSb LWIR (50% cutoff wavelength is 14 μm) detectors after conventional BCl_3-based plasma assisted etch, chemical etch (H_2O_2:HCl:H_2O= 1:1:4), and a combination of both etches. Chemical etch was primarily optimized using n-type GaSb substrates, and during this process numerous chemical etchants were examined. Contradictory to our expectations, we found that the smoothest sidewall profile with reasonable undercut was obtained after chemical etch alone. Plasma-assisted etch generated a lot of damage; in particular, etch residues and a two-step sidewall profile were observed. We also observed that the application of chemical etch subsequent to the plasma-assisted etch restored the damaged surface. However, resulting sidewalls were rough with clearly visible ripples, and the surface near the base of etched mesas was heavily degraded.

Since wet chemical etching is usually an isotropic process, it is commonly thought to be incompatible with current trends in fabrication of high-fill-factor large-format FPAs based on InAs/GaSb SLS. The observed undercut (5 μm for each mesa side) should provide dimensions of FPA pixels (typical pitch size 30 μm) that are still acceptable for subsequent fabrication steps.

Next, we have studied sidewall profiles of 24 μm x 24 μm mesas etched on InAs/GaSb SLS LWIR. Material was the same as for the single-pixel device etch studies. The chemical etch using the H_2O_2:HCl:H_2O= 1:1:4 solution showed significant lateral etch (9 μm each side) and hence rendering itself unpractical for FPA fabrication. An additional optimization of chemical etch on 24 μm x 24 μm size features was undertaken and resulted in rough sidewalls as well as lateral etching. Plasma-assisted (ICP) etch resulted in smooth vertical sidewalls of individual FPA pixels free from any etch residuals with no undercut (with respect to mask) observed. Application of chemical etch subsequent to the plasma assisted etch was expected to further smooth the sidewalls, however, it resulted in undercut estimated to be 8 μm on each side of FPA mesa, which is not acceptable for the subsequent FPA fabrication steps. In conclusion, we found that the plasma-assisted (ICP) etch is the only acceptable method for fabrication of small dimension mesa structures in high fill factor FPAs based on InAs/GaSb SLS.

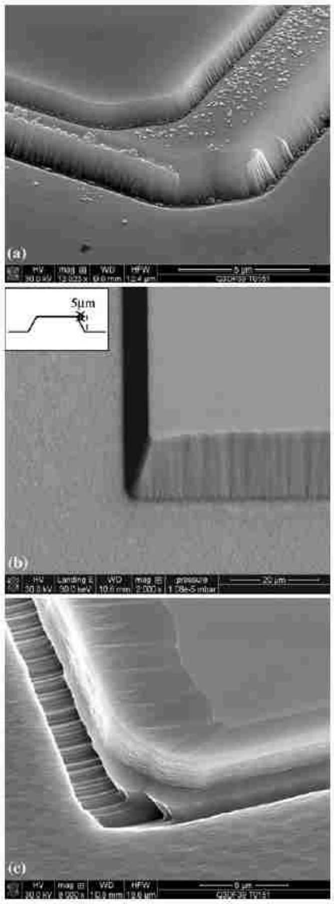

Figure 4.8: Sidewall profiles obtained for (a) plasma-assisted dry etch, (b) optimized chemical etch, with inset showing the etch profile having an undercut with respect to mask, and (c) combination of plasma-assisted and chemical etch.

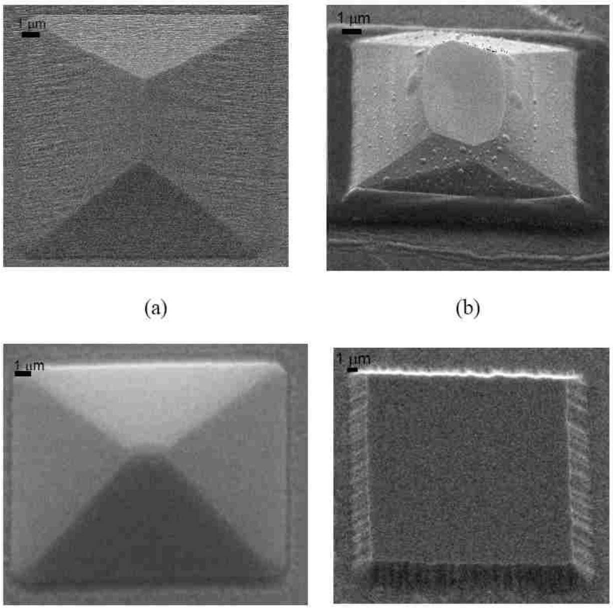

(a) (b)

(c) (d)

Figure 4.9: Scanning electron micrograph (SEM) images of 24 μm x 24 μm mesa of InAs/GaSb SLS LWIR FPA obtained after (a) optimized chemical etch (H_2O_2:HCl:H_2O = 1:1:4), (b) diluted HCl-based etch (H_2O_2:HCl:H_2O = 1:1:10), (c) citric acid ($C_6H_8O_7$) based etch, and (d) phosphoric acid (H_3PO_4) based etch.

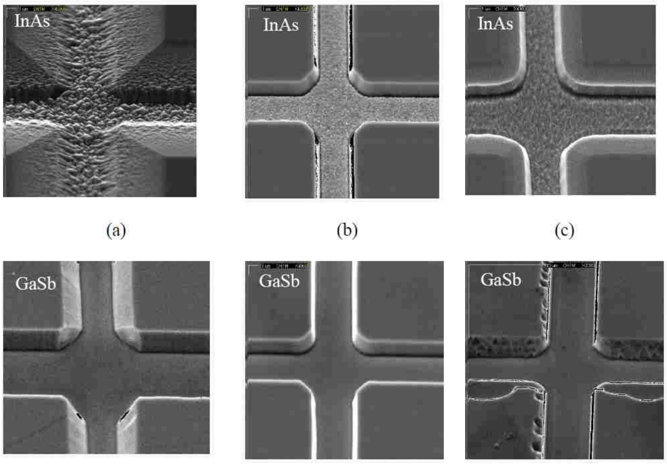

(a) (b) (c)

(d) (e) (f)

Figure 4.10: SEM images of FPA with 30 μm pitch fabricated on InAs (a-c) and GaSb (d-f) substrates by HCl-based chemical etch only (a and d); plasma-assisted (ICP) etch only (b and e); and combination of plasma assisted and chemical etch (c and f). Mesa size is 24 μm x 24 μm.

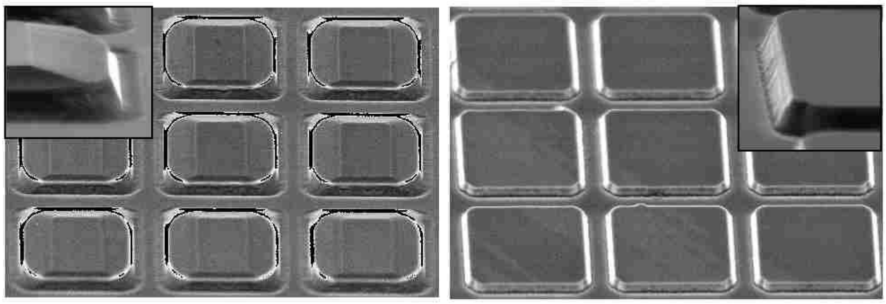

(a) (b)

Figure 4.11: SEM images of InAs/GaSb SLS LWIR FPA with 30 μm pitch obtained after (a) combination of plasma assisted (ICP) and HCL-based etches (H_2O_2:HCl:H_2O (1:1:4)) and (b) ICP etch only. Insets show the sidewall profile of 24 μm x 24 μm FPA mesa.

Chapter 5

Electrical Characterization of Passivated InAs/GaSb SLS Detectors

How to quantify passivation? The first answer would be to passivate a device surface and measure the results electrically. This is the objective of the study in this chapter. The second, more complicated answer would be to look at its material properties: (a) as an entity by itself and (b) its interaction with the complex surface of InAs/GaSb superlattice.

In this chapter, we study the functioning of the device with passivant as one unit and not as InAs/GaSb/passivant individually. During the course of the following study we search to establish a passivation technique that satisfies all the criteria laid out in Chapter 3, section 3, where in it states that an ideal technique must be (i) an excellent encapsulant that is to prevent interaction between the semiconductor surface and ambient atmosphere; (ii) a good chemical passivant i.e. eliminate the formation of surface states by forming covalent bonds with the semiconductor surface itself; (iii) an excellent insulator i.e. it must serve as an energy barrier so that the carriers from the semiconductor surface must not be lost in the passivant; (iv) stable for the long term and able to perform with the same efficiency through-out the lifetime of the detector; (v) thermally stable, so as to operate well from 77K-300K; (vi) forming uniform layers on the semiconductor surface as non-uniform deposition can lead to stress at the interface of passivant and semiconductor; (vii) easy to implement into the FPA fabrication.

5.1 Growth and Fabrication of InAs/GaSb SLS Detectors

The detector structures were grown on n-type (Te-doped) GaSb (100) epi-ready substrates using a solid source MBEVG-80 system equipped with valved cracker sources for the group V Sb_2 and As_2 fluxes, and Ga/In SUMO®cells. Growth details have been reported elsewhere [87]. The pin detector structure was formed by 2.8 μm (395 periods) 14 MLs InAs/7 MLs GaSb SLS non-intentionally doped (n.i.d.) absorber grown on top of a 690 nm thick n-type (1 x 10^{18} cm^{-3}) contact layer (formed by SLS with the same thickness and composition as absorbing region with Te-doped InAs layers). The structure was capped by a 100 nm thick GaSb p-type (4 x 10^{18} cm^{-3}) top contact layer. In order to improve carrier transport in the detector structure, 25 periods of top part of SLS absorber were p-type doped with the lower doping concentration (1 x 10^{17} cm^{-3}). With the same purpose doping was gradually changed in 25 periods of bottom and top parts of SLS absorber.

The pBiBn detector structure had 630 nm thick (90 periods)14 ML InAs/9 ML GaSb SLS p-type contact layer doped with Be (p = 2.8 x 10^{18} cm^3) followed by non-intentionally doped (n.i.d.) electron blocking (EB) layer consisting of 295 nm thick 6 ML InAs/10 ML GaSb SLS (60 periods). Then a 1.8 μm thick (312 periods) n.i.d absorber region of 13 ML InAs/6 ML $In_{0.15}Ga_{0.85}Sb$ GaSb SLS was grown.

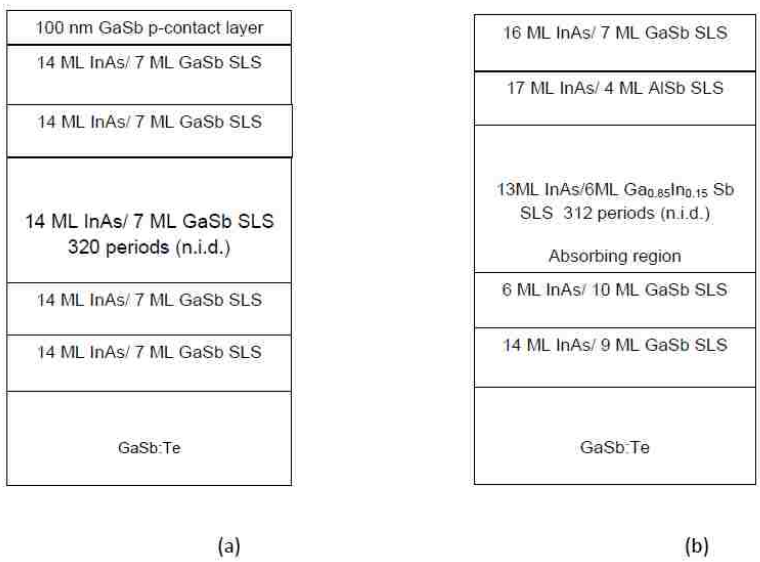

Figure 5.1: Heterostructure schematic of InAs/GaSb SLS detector structure with (a) p-i-n and (b) pBiBn designs.

Next, n.i.d 255 nm (40 periods) thick hole blocking (HB) layer made of 17 ML InAs/4 ML AlSb SLS was deposited and 100 nm (15 periods) thick n-type contact layer made of 16 ML InAs/7 ML GaSb doped with Te (n = 3 x 10^{18} cm^{3}) completed the structure. In both detector structures SLSs were grown with imposed InSb interfaces in order to balance strain. The heterostructure schematics of p-i-n and PbIbN detectors are shown in Figure. 5.1 (a) and (b), respectively.

The structural quality of as-grown material was assessed by high-resolution x-ray diffraction (HRXRD) performed with a Philips double-crystal X-ray diffractometer using the Cu-K1 line and all measurements were carried out at 300K. The HRXRD spectra of the InAs/GaSb SLS LWIR pin and pBiBn detectors at (004) reflection are shown in Fig. 5.2 (a) and (b), respectively. The lattice mismatch of SLS to the GaSb substrate is equal to 0.13% (pin) and 0.06% (pBiBn). Low lattice mismatch enables the growth of SLS diodes with large number of periods without

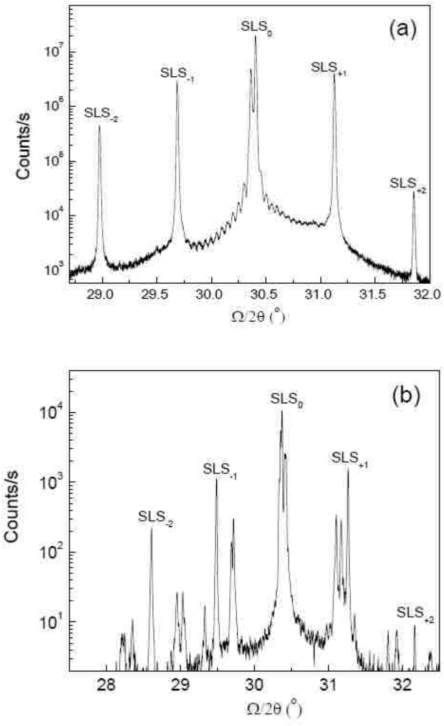

Figure 5.2: High-resolution (004) X-ray diffraction pattern of the InAs/GaSb SLS detector structure with (a) pin and (b) pBiBn designs.

degrading its quality. Furthermore, observation of the sample surface under Nomarski microscope reveals good surface quality without growth defects. The full width at half maximum (FWHM) of the first-order satellite peak of SLS is found to be 36 arcsec (p-i-n) and 28 arcsec (pBiBn); several orders of SLS satellite peaks were observed indicating good crystalline quality of the material.

Device fabrication was initiated using standard optical photolithograpy to define 410 μm x 410 μm square mesa devices with apertures ranging from 25-300 μm and a variable area diode array (VADA) patterns with areas ranging from 30 μm x 30 μm to 400 μm x 400 μm. Etching was performed using inductively coupled plasma (ICP) reactor with BCl_3 gas. Sample was physically clamped to

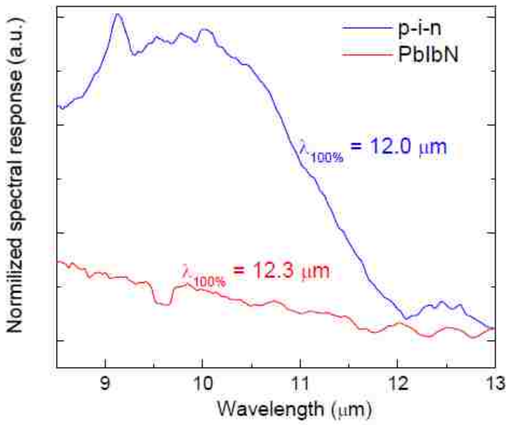

Figure 5.3: Spectral response of InAs/GaSb SLS detectors with pin and pBiBn designs at 0.1 V of applied bias and 77 K.Reprinted from [89]

the substrate electrode in order to reduce lateral etching. The flow of He to the backside of the wafer maintains its temperature at 25C. The resulting etch depth corresponded to the middle of the bottom contact layer of the detector. Next, ohmic contacts were evaporated on the bottom and top contact layers using 50 nm Ti/ 50 nm Pt/300 nm Au in both cases. It has to be noted that depending on the type of passivation treatment utilized, passivation was applied at different stages of device fabrication and this is explained further in this chapter and Appendix A.

The normalized spectral response of the pin and pBiBn detectors was measured with a glow-bar source within the Fourier Transform Infrared (FTIR) spectrometer and shown in Fig. 5.3. The 100%-cut-off wavelength was equal 12.0 μm for the pin detector and 12.3 μm for the pBiBn detector (at 77 K and V_b = -0.1 V). The spectral response has been shown for wavelengths higher than or equal to 8.4 μm since a longwave bandpass filter (8.4 - 11.5) μm was used for the radiometric measurements.

5.2 PIN Device Passivation

First, several passivation treatments were applied to a SLS detector with the pin design. Details of each passivation are described below. Immediately before every passivation treatment except ammonium sulfide passivation, the native oxide was removed by placing samples in a phosphoric acid based solution (H_3PO_4:H_2O_2:H_2O = 1:2:20) for 30 seconds. In case of $(NH_4)_2S$ passivation the native oxides are etched by $(NH_4)OH$ formed in aqueous solution of ammonium sulfide.

5.2.1 Dielectric Passivation

Silicon nitride (as shown in Fig 5.4) and silicon di-oxide (as shown in Fig 5.5) were applied on etched mesa sidewalls after the definition of individual devices with inductively coupled plasma (ICP) etch. A 200 nm thick SiN_x layer with nominal composition of Si_3N_4 was deposited on etched sidewalls in plasma enhanced chemical vapor deposition (PECVD) system at 300°C. The Si_3N_4 layer was removed from the aperture and top and bottom metal contact regions by reactive ion etcher (RIE) using CF_4 gas for six minutes and at RT. Silicon di-oxide with a thickness of 200 nm was deposited in an e-beam evaporator at 170°C. The SiO_2 layer was removed from the aperture and top and bottom metal contact regions by reactive ion etcher (RIE) using CF_4 gas for four minutes and at RT. It should be noted that the typical temperature of SiO_2 deposition in a PECVD system is 320°C [59]. Special care was taken to develop a low temperature process of high-quality SiO_2 deposition to prevent SLS period intermixing.

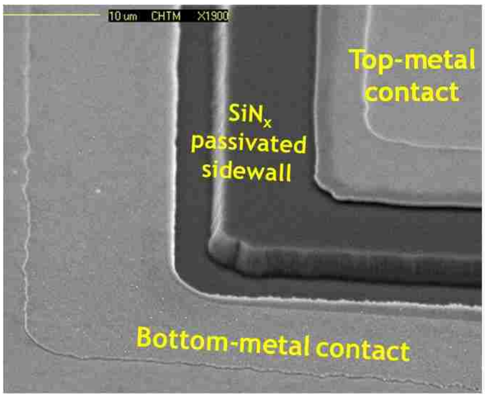

Figure 5.4: SEM images of SiN$_x$ passivated InAs/GaSb SLS detectors with pin design.

5.2.2 Organic material based passivation: SU-8 Deposition

SU-8 passivation was applied to the completely processed detector structures as a last step in a processing sequence. SU-8 consists of a bisphenol-A novolak epoxy

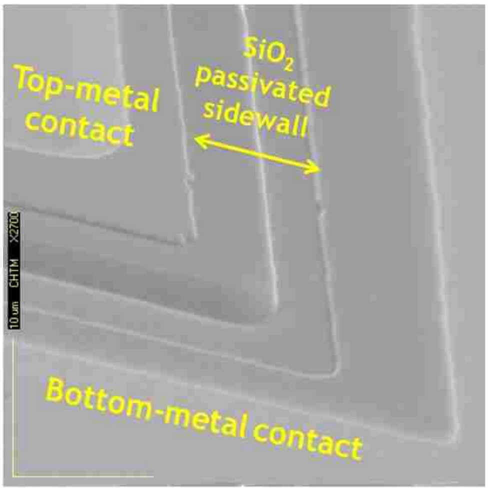

Figure 5.5: SEM images of SiO$_2$ passivated InAs/GaSb SLS detectors with pin design.

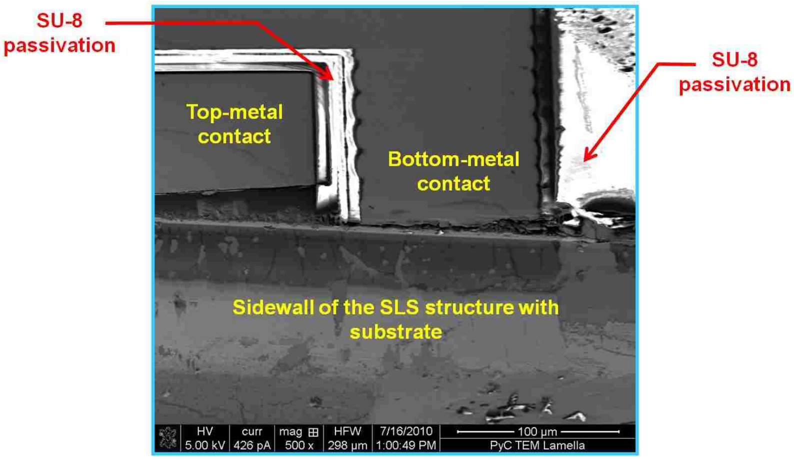

Figure 5.6: SEM images of SU-8 passivated InAs/GaSb SLS detectors with pin design.

resin, a photo initiator, and solvent - butyroalectone [116]. The photo initiator is easily broken down and changes into strong acid ($HSbF_6$) upon exposure of UV. This acid causes a high cross-link density in the SU-8 film, thereby leading to an increase in its chemical resistance to the developer. Photo-polymerized SU-8 is mechanically and chemically stable after a hard bake. Application of SU-8 was performed at room temperature and followed the processing guidelines found elsewhere [1]. The resulting thickness of the SU-8 passivation film was approx. 1.5 μm. The fabrication of SU-8 passivated detectors in described in Appendix A.

5.2.3 Chalcogenide Passivation

Ammonium Sulfide

Ammonium sulfide passivation was applied to the completely processed detector structures as a last step in a processing sequence. Passivation layer is not removed from the aperture, top and bottom contact regions and this is seen in the

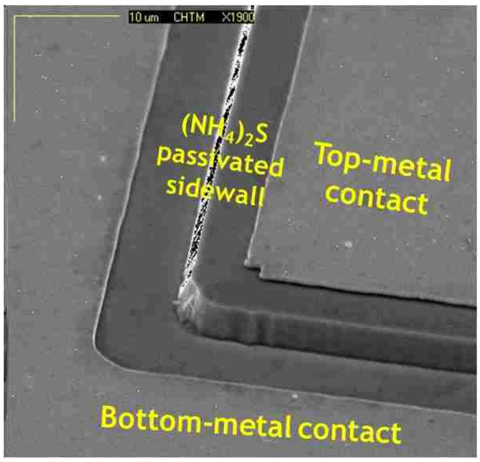

Figure 5.7: SEM images of an ammonium sulfide passivated InAs/GaSb SLS detectors with pin design.

SEM image of a $(NH_4)_2S$ passivated device shown in Fig 5.7. To perform $(NH_4)_2S$ passivation the completely processed detector structures were immersed in a passivation solution that contained 20% ammonium sulfide diluted in four parts of water for 2 hours. The thickness of the resulting passivation film was 10nm.

Zinc Sulfide

This passivant was applied on etched mesa sidewalls after the definition of individual devices with inductively coupled plasma (ICP) etch. A 200 nm thick ZnS film was deposited on etched mesa sidewalls in an dielectric electron-beam evaporator at room temperature. The ZnS was removed from regions of the aperture and top and bottom metal contact regions and these regions are indicated in Fig 5.8. For this removal a wet etch solution of HCl:H_2O (1:10), was used at etch time of two minutes and at room temperature.

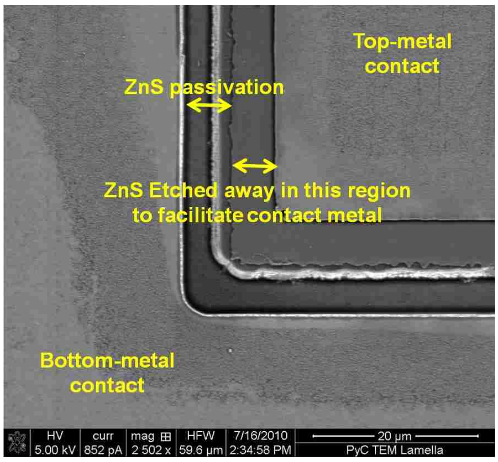

Figure 5.8: SEM images of a ZnS passivated InAs/GaSb SLS detectors with pin design.

5.2.4 Electrochemical Sulfur Passivation (ECP)

This passivant was applied on etched mesa sidewalls after the definition of individual devices with inductively coupled plasma (ICP) etch. Passivation treatment was the last step in this device fabrication process just as in the case of $(NH_4)_2S$ passivation. Here too passivation layer is not removed from the aperture, top and bottom contact regions and this is indicated in Fig 5.9. The electrochemical cell for the sulfur passivation consisted of the sample (anode), a platinum mesh electrode (cathode) and the electrolyte in a glass beaker at room temperature. The electrolyte was 0.1 M Na_2S in ethylene glycol. A square-shaped constant DC current with a magnitude of 33 μA was supplied from the programmable current source to the back of the sample for a limited amount of time (5 min). The samples were then rinsed with isopropanol and blow dried with N_2. The resulting thickness of the sulfur layer was $\sim$ 5 nm [91].

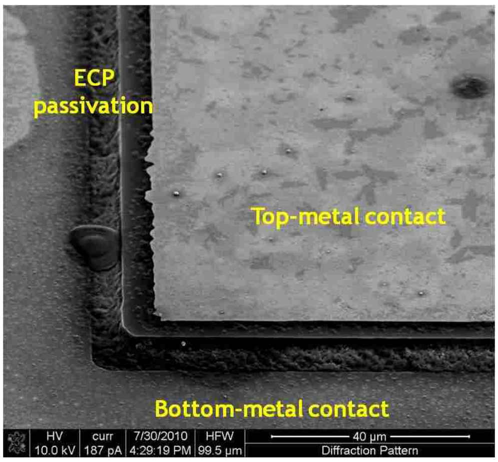

Figure 5.9: SEM images of an ECP passivated InAs/GaSb SLS detectors with pin design. It can be seen that ECP not only covers the side wall of the device but is also present on the top and bottom contact regions.

5.2.5 Results of comparison of passivation techniques on PIN device

Passivation efficacy was evaluated by measuring current-voltage (I-V) dependence at 77 K for VADA detectors. All I-V measurements were conducted on variable-temperature Janis ST-500 micromanipulated probe station under zero field of view. The responsivity measurements were carried out at the same temperature using a calibrated black-body source at 800 K.

Fig. 5.10 shows the dark current density of pin SLS detectors unpassivated and passivated by various treatments measured at 77 K as a function of VADA mesa area. Table 5.1 summarizes out the comparison of dark current densities measured at -0.1 V of applied bias, R_0A product, and surface resistivity $r_{surface}$ for utilized passivation schemes.

The dielectric and photoresist passivation treatments (SiN_x, SiO_2, and SU-8)

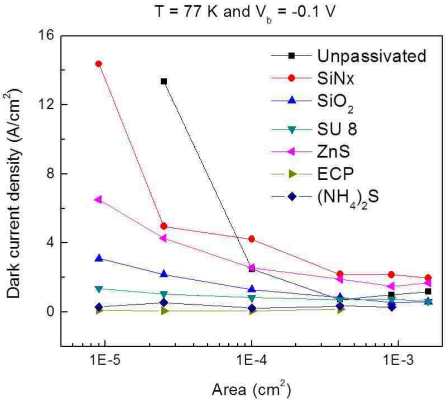

Figure 5.10: Dark current density vs mesa area of unpassivated and passivated by various treatments SLS detector with pin design.

resulted in improvement of dark current density by factors of ~ 2.5, 6, and 13, respectively, compared with the unpassivated device with the same area. We attribute this to the band bending at the semiconductor surface caused by the nature of band alignment at the pasisivant-semiconductor interface and the presence of fixed charges inside the passivation layer. The fixed charge density in electron-beam evaporated ZnS is expected to be lower than in SiN_x deposited under a plasma environment [8]. In addition, ZnS facilitates saturation of surface states by formation of sulphur bonds by constituent atoms of InAs/GaSb SLS. Both of these factors should result in better passivation efficacy of ZnS. However, we found improvement of dark current density in ZnS passivated devices by a factor of 3, which is comparable with that obtained by using SiN_x passivation. This may be the result of the inferior quality of deposited ZnS film, and development of a high-quality ZnS deposition procedure is currently under development in our group.

The electrochemical sulphur (ECP) deposition and ammonium sulfide treatment appeared to be the best passivants, reducing dark current density of 50 μm x 50 μm devices by factors of ~ 200 and 25, respectively. Both of these passivants saturate the surface states by sulfur and create an ordered layer of sulfur adatoms on the semiconductor surface [51, 91].

5.2.6 Study of Long term Stability of ECP in PIN device

To evaluate the long-term stability of ECP passivation, we measured I-V characteristics of the pin detector treated with ECP right after the passivation and four weeks later. The results are presented in Fig. 5.11 (left) and it indicated that the detector performance did not degrade significantly for the large area device (400 μm x 400 μm), whereas the dark current density of ECP had degraded over time with J_d being 0.09A/cm^2 right after passivation and 2.18A/cm^2 after 4 weeks of passivation for the smallest area device (30 μm x 30 μm) [89]. We attribute it to the reaction of sulphur with oxygen in the air to form SO_2 gas. Thus, the encapsulation with some type of dielectric or photoresist material (e.g. SiN_x, SiO_2, or SU-8) is required to prevent the ECP passivation from degradation. In the next experiment we spun SU-8 over an ECP passivated device and found that this device degraded heavily for all the mesa areas except for the 400 μm x 400 μm device as seen in Fig. 5.11(right). The fact that dark current density degrades maximum on smallest mesa area device as compared to the largest mesa area, indicates to us that the very thick 1.5μm of SU-8 must be peeling away 50Å of ECP from the surface and hence ruining the sulphur- InAs/GaSb bonds.

5.3 pBiBn Device Passivation

For the passivation of pBiBn LWIR InAs/GaSb SLS detector structure we utilized only the electrochemical sulfur (ECP) deposition and ammonium sulfide treat-

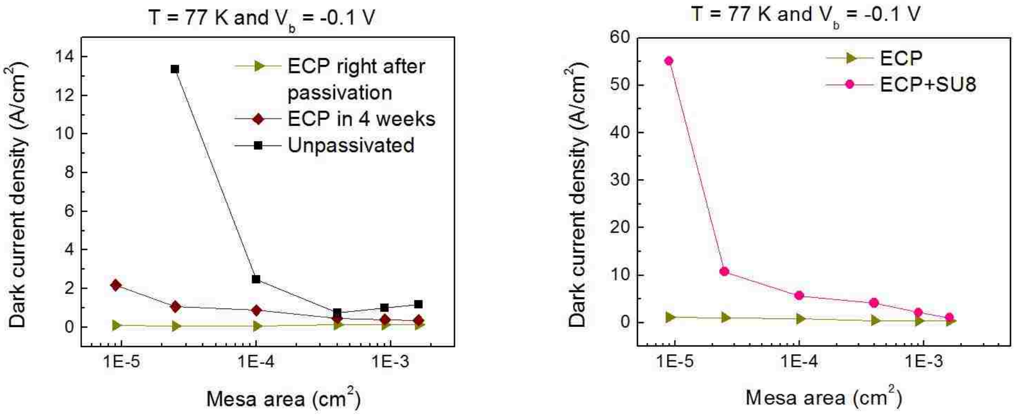

Figure 5.11: (Left)Dark current densities of unpassivated and ECP passivated pin detector measured at 77 K right after passivation and in four weeks.(Right) Dark current density vs. mesa area of ECP by itself vs ECP with SU-8 passivation.

ment, since they resulted in best quality passivation of pin SLS LWIR detectors (as presented in Section 5.2). Fig. 5.12(Top) presents the dark current density vs VADA mesa area of unpassivated and passivated by ammonium sulfide and ECP treatments for SLS detector with pBiBn design measured at 77 K. The dark current

Table 5.1: Performance comparison of pin SLS LWIR detectors passivated by various treatments.

Passivation Technique	J_d, A/cm^2 (at - 0.1 V)	R_0A, Ωcm^2	$r_{surface}$, Ωcm
Unpassivated	1.39	0.09	6.50
SiN_x	2.21	0.07	6.81
SiO_2	1.40	0.06	14.24
ZnS	1.67	0.03	16.05
SU-8	0.83	0.04	27.85
$(NH_4)_2S$	0.30	0.27	65.88
ECP	0.09	0.28	1479.22

density of 30 μm x 30 μm detector was reduced by factors of $\sim$ 3 and 54 for the $(NH_4)_2S$ and ECP treatments, respectively.

The inverse of the dynamic resistance area product (R_0A) at zero bias as a function of the perimeter-to-area ratio at 77 K for unpassivated, $(NH_4)_2S$ and ECP passivated detectors is shown in Fig. 5.12(Bottom)

Surface resistivity $r_{surface}$ values equal to 6, 29, and 2717 Ωcm for the unpassivated, the $(NH_4)_2S$ passivated, and ECP passivated detectors, respectively, revealing three orders of magnitude improvement of $r_{surface}$ for ECP treated devices at 77 K. As was shown by Gautam et al. [39] the typical operating voltage of pBiBn detectors is 50-250 mV (negative bias). We found that the measured responsivity of unpassivated, $(NH_4)_2S$ and ECP passivated pBiBn detectors at 250 mV was equal 0.8 A/W (77 K, 10 μm).

The shot noise limited specific detectvity D* was calculated at 10 μm using the equation

$$D^* = \frac{R}{\sqrt{2qJ + \frac{kT}{R_d A_d}}} \tag{5.1}$$

where R is the responsivity, q is the electronic charge, T is the temperature of the device, k is Boltzmanns constant, J is the current density, R_d is the dynamic resistance, and A_d is the diode area. The D^* was improved by a factor of two and ten for $(NH_4)_2S$ and ECP passivated detectors, respectively.

5.4 Comparison of Various Sulfide Passivants

The comparisons of wet-chemical (including ECP) depositions of passivants as against dry methods of deposition (vacuum coating techniques) of the same passivants need to be worked out. The detector material used in this study was grown by solid source MBE on n-type (Te-doped) epiready (100) GaSb substrate at Intelligent Epitaxy Technology, Inc. (IntelliEPI). Detector heterostructure utilized the graded-bandgap W-design SLS proposed by Aifer et al. [6] The band gap of such n-on-p structure is increased in a series of steps from that of the lightly p-type IR-absorbing region to a value typically two to three times larger. The grading steps (W-SLS) were formed by InAs/GaInSb/InAs/AlGaInSb period structure, with various composition and thickness of barrier, electron and hole wells. Absorbing region with total thickness of 4 μm formed by p-type InGaSb/InAs SLS (p = 4 x 10^{15} cm^{-3}) was surrounded by n and p-type contacts composed of InAs (n = 4 x 10^{17} cm^{-3}) and GaSb (p = 3 x 10^{18} cm^{-3}), respectively. Further design details were reported elsewhere [6].

The detector material was processed into a VADA arrays of square and circular mesa diodes with the size of diode mesa sides (diameters) ranging from 25 to 400 μm using standard optical photolithography techniques. For radiometric characterization, the material was processed as single element detectors with 410 μm x 410 μm square mesas having apertures ranging from 25 to 300 μm. The processing was initiated by an inductively coupled plasma (ICP) etch to the middle of the bottom contact layer with total etch depth of 4.9 μm. Next, 50 nm Ti/ 50 nm Pt/ 300 nm Au was deposited as the bottom and top contact metallization. Finally, detectors were passivated with different passivation schemes with details of each described below and summarized in Table 5.2. All passivation treatments, except $(NH_4)_2S$, were preceeded by short (20 sec) dip in H_3PO_4:H_2O_2:H_2O (1:2:20) solution. In Table 5.2, the nomenclature TAM 1 and TAM 2 stands for acid-based and base-based thioacetamide (TAM) passivation solutions, respectively.

To perform TAM passivation the samples were immersed in a 0.18M CH_3CSNH_2 solution for 40 minutes at 70C. The pH of TAM solution was adjusted to be acidic or basic by adding an acetic acid (10%) or NH4OH(30%), respectively.

Table 5.2: Summary of chalcogenide-based passivation treatments carried out on graded bandgap W-design structure.

Passivation	Deposition technique	Temperature	Thickness
TAM 1.	Wet Bath	55C	~ 10 nm
TAM 2	Wet Bath	55C	~ 10 nm
ZnTe:Cl	MBE	250C	200 nm
$(NH_4)_2S$	$(NH_4)_2S:H_2O$ (1:4) 70 min	RT	5-10 nm
ECP	Na_2S:ethylene glycol	RT	~ 5 nm

The electrochemical cell for the sulfur passivation consisted of the sample (anode), a platinum mesh electrode (cathode) and the electrolyte in a glass beaker at room temperature. The electrolyte was 0.1 M Na_2S in ethylene glycol. A square-shaped constant DC current with a magnitude of 33 μA was supplied from the programmable current source to the back of the sample for a limited amount of time (5 min). The samples were then rinsed with isopropanol and blow-dried with N_2.

The 100%-cut-off wavelength of fabricated detectors was determined through spectral response measurements performed using a Nicolet 670 Fourier transform infrared (FT-IR) spectrometer with a glow-bar black body source and was found to be equal 9.8 μm at 77 K (V_b = -0.1 V). Figure 5.13 shows the representative normalized spectral response curves for various temperatures measured at -0.1V of applied bias at various temperatures.

Passivation efficacy was evaluated by measuring current-voltage (I-V) dependence at 77 K for VADA detectors. All I-V measurements were conducted on variable-temperature Janis ST-500 micromanipulated probe station under zero field of view. Fig. 5.14 shows a comparison between dark current densities of as-etched and treated by different passivations devices with perimeter-to-area ratio

(P/A) of 1600 cm^{-1}. Under typical value of operational bias, -0.1 V, the dark current density decreased from ~ 0.8 A/cm^2 for unpassivated samples to ~ 0.3 A/cm^2 and 0.04 A/cm^2 for acidic and base solutions TAM treatments, respectively, and to ~ 2.7 x 10^{-3} A/cm^2 for ECP treatment.

Fig. 5.15 presents a plot of R_0A versus the perimeter-to-area ratio (P/A) for unpassivated and passivated by various treatments SLS detectors measured at 77 K. The nearly linear dependence of $1/R_0A$ (P/A) curve for ECP treated sample indicates the negligible surface leakage currents. Contradictory to our expectations the basic TAM passivation demonstrated superior performance compared to acidic TAM treatment. Reasons of this phenomenon is currently under investigation.

Fig. 5.16 presents the shot-noise limited D^* as a function of applied bias for as-fabricated and treated by various passivations detectors evaluated at liquid nitrogen temperature. At operational bias value, -0.1 V, the ECP treatment resulted in improvement of shot-limited D^* by factor of 5 compared to unpassivated device. The corresponding value of quantum efficiency (QE) was equal ~ 12% at the same value of applied bias for unpassivated detector.

5.5 Novel chlorine-doped Zinc Telluride (ZnTe: Cl) Passivation

In the previous section, we compared various sulfide passivations most of which such as ZnS, $(NH_4)_2S$ are chalcogenide passivants. But among all chalcogenides, and sulfides, ECP came out on top with the lowest dark current. There of establishing that it was not any sulfide compound would do, but the very thin film of pure sulfur terminated the dangling bonds and eliminates formation of native oxides most efficiently. The problem with ECP is that its structural stability degrades over time as seen in Section 5.3. For that reason we looked for a replacement that would be also close in family of chalcogenides to mimic sulfide properties and decided upon Zinc Telluride (ZnTe).

Zinc Telluride (ZnTe) is a wide-bandgap (E_g= 2.23-2.26eV) compound semiconductor belonging to the II-VI semiconductor material family. It has been widely used in various solid state devices such as laser diodes, blue light emitting diodes, solar cells and a important emerging compound for devices operating in the terahertz regime [13, 56, 106, 98, 99]. ZnTe has a zinc-blende crystal structure with a lattice constant of a_{ZnTe}=6.1034Å which is lattice matching to GaSb and close to that of InAs and AlSb. Hence ZnTe would be a suitable material to use as passivant coating on InAs/GaSb based SLS structures. Also, ZnTe can be epitaxially grown by MBE ensuring uniform deposition and high quality material with minimal defects. Due to the robust nature of the ZnTe layer, we can expect no peeling as in ECP indicating long term stability of the passivant. Since ZnTe can be etched, conforming to any mesa size/shape and since it can withstand post processing, ZnTe is ideally suited for FPA fabrication.

To investigate the performance of ZnTe as a passivation technique on T2SLS, it was epitaxially grown on the same p-i-n detector heterostructure as employed in the comparison of various passivations in Section 5.2. The ZnTe was MBE grown in University of Michigan, Ann Arbor by Prof. J.D. Phillips and Dr. W. Wang [104]. About 150nm-160nm thick ZnTe was epitaxially grown at 250°Cwith a short thermal clean at 300°C. The SEM images a fully fabricated detector structure with ZnTe is shown in Fig. 5.17. The figure shows a clean and uniform surface at the sidewalls of the detector indicating uniform, defect free deposition. The fabrication process is the same as detailed in Appendix A. For the passivation etch where ZnTe is etched away at the areas where contact metal need to be deposited, we implemented a dry etch technique of ICP with BCl_3 plasma.

When I-V dark currents were measured on these diodes, they were all shorts. This indicated that the ZnTe passivant was conducting forming an alternative path for the charge carriers to migrate. This is because ZnTe is an intrinsically p-type material even without impurity doping due to native defects inherent in the material [102]. This inherent p-type property arises due the offset in stoichiometry by way of Zn-deficiency and thereby having Zinc vacancies [V(Zn)] which act as acceptors. To make the compound insulating i.e. have higher resistivity, Zn-excess rather than Te-excess conditions need to be achieved during growth [55]. Furthermore, halogen impurities such as Cl, Br, and I can help retain higher resistivity since halogen occupies Te-lattice sites, acting as donor impurity and compensates for Zn-vacancy.

In order to compensate for the highly conductive ZnTe passivation, we doped the compound with chlorine$\sim$10E18cm^{-3}. The final thickness of ZnTe:Cl layer was 200nm and it was epitaxially grown by the MBE at 250°C. For this second round of experiments we used two detector structure, (i) p-i-n detector heterostructure same as employed in round 1 and (ii) the detector heterostructure utilizing the graded-bandgap W-design SLS [6] as employed in the comparison of various sulfide passivations in Section 5.4. As established in Section 5.4, the graded-gap W-design SLS detector structure was grown at IntelliEPI. The fabrication process for both were performed same as in round 1.

The second round of ZnTe:Cl passivation on the pin architecture of InAs/GaSb SLS heterostructure showed chlorine doped ZnTe has the dark current density (J_d) of 0.21A/cm^2 at mesa area=1E-4cm^2 and T=77K, V=-0.1V whereas in unpassivated J_d=5.02A/cm^2. Figure 5.18 indicates that ZnTe:Cl passivation shows minimal change of dark current density over mesa area. This implies that the passivation was successful in reducing surface leakage currents and the device dark current is bulk limited not surface limited anymore. On the graded-gap W-design SLS heterostructure, Cl_2 doped ZnTe showed an improved $(R_0A)_{max}$ of 67.64Ω-cm^2 compared to the (R_0A)max of 21.97Ω-cm^2 of the unpassivated device. When ECP was compared with Cl_2 doped ZnTe on the graded-gap W-design SLS heterostructure, ZnTe:Cl showed a surface resistivity ($r_{surface}$) of 6700.51 Ω-cm where as ECP had a $r_{surface}$ of 10^5 Ω-cm and unpassivated had a $r_{surface}$ = 155.89Ω-cm. Figure 5.19 clearly shows this scheme of improvement of ECP over Cl_2 doped ZnTe over unpassivated.

Next we investigated the long term stability of the Cl_2 doped ZnTe and the results are shown in Figure 5.20. We can learn from this plot that Cl_2 doped ZnTe passivation technique show minimal change in dark current density over varying periods of time i.e. from the initial measurement right after the passivation fabrication and 4 weeks after. On the graded-gap W-design SLS heterostructure. ZnTe:Cl showed a J_d of 0.07Å/cm^2 right after passivation and J_d of 0.04Å/cm^2 at mesa area =1E-4cm^2, T=77K and V=-0.1V,4 weeks after passivation. Whereas, on pin architecture of InAs/GaSb SLS heterostructure, ECP showed a J_d of 0.5Å/cm^2 right after passivation and J_d of 1.0Å/cm^2 at mesa area =1E-4cm^2, T=77K and V=-0.1V,4 weeks after passivation. This is a clear indication when it comes to long term stability and FPA fabrication, Cl_2 doped ZnTe is preferable over ECP.

To the best of our knowledge, no other team has worked on ZnTe as passivant in T2SLS or any other IR technology. Cl_2 doped ZnTe seems to satisfy all the 7 criteria we set in the introduction of this investigation. Hence from the results these initial experiments, we can confidently predict that Cl_2 doped ZnTe seems like a possible alternative to ECP. Further trials have to be performed to improve its performance efficiency and optimize the material such as (i) varying the thickness of the ZnTe:Cl layer; (ii) varying the Cl_2 doping; (iii) varying Zn to Te ratio; (iv) study the effects of post annealing after doping; (v) investigate the effects of changes in temperature. The higher surface leakage currents in ZnTe: Cl_2 passivation can be due to the offset in stoichiometry. T.Ishizaki et. al. [55] reported that in their electrochemically deposited ZnTe, when the Zn concentration is reduced, the resistivity of the ZnTe films decreases although Zn:Te ratio is maintained nearly 1:1. This indicates that the Zn-vacancies are acting as acceptors to lower resistivity. The same argument can be extended to MBE grown ZnTe films as well and Zn-excess conditions i.e. (1+x)Zn:1Te can be maintained during growth. A second option would be to generate a multi-layer passivant by depositing Si_3N_4 encapsulating the passivating layer of ZnTe. Using ZnTe:O which has shown higher resistivity than ZnTe [104] may also be another option.

5.6 Conclusions

In conclusion, first we have investigated different passivation treatments for the improved performance of type-II InAs/GaSb SLS detectors with pin and pBiBn designs operating in the LWIR spectral region (100% cut-off wavelength of ~ 12 μm at 77K). The ammonium sulfide passivation and electrochemical sulfur passivation (ECP) showed superior performance, improving the dark current density by factors of 200 and 25 (pin detector) and ~ 3 and 54 (pBiBn detector), respectively (T = 77 K, -0.1 V of applied bias). The specific detectivity D^* was improved by a factor of two and by an order of magnitude for $(NH_4)_2S$ and ECP passivated pBiBn detectors. The reported improvement of device performance suggests that the $(NH_4)_2S$ and ECP passivation techniques have promising implications for the practical realization of FPAs based on type-II InAs/GaSb SLS.

In the next experiment, we compared efficacy of various sulfur-based treatment on performance of LWIR InAs/GaSb SLS detector with graded-bandgap design [6]. We found values of $r_{surface}$ equal to 1.7 x 10^2, 6.8 x 10^2, ~ 3 x 10^3, and 1.4 x 10^5 Ωcm for the unpassivated, TAM acidic, TAM basic, and ECP passivated detectors, respectively, revealing three orders of magnitude improvement of $r_{surface}$ for ECP treated devices at 77 K. The typical values of $r_{surface}$ are ~ 10^4 Ωcm, 204 Ωcm, and 196 Ωcm for polyimide [50], SU-8 [57], and SiN_x [8] passivations, respectively, applied to InAs/GaSb SLS detectors with LWIR cut-off wavelengths. Passivation of LWIR SLS detectors by other sulfidization schemes yields $r_{surface}$ values of 29 Ωcm (ammonium sulfide-based passivation) [50] and 2.5 x 10^3 Ωcm (ZnS treatment) [8]. ECP improved J_d compared to unpassivated, by factor of 15 in InAs/GaSb SLS heterostructure and by a factor of two in InGaSb/InAs SLS heterostructure. This could be due to the formation of InO_x which helps in reducing surface conduction as stated in J. Nolde et al [77]. This observation has to be further investigated by performing systematic surface material characterization such as XPS measurements.

In the long term stability study of ECP on InAs/GaSb SLS based LWIR detector with pin design, detector performance for the smallest area device (30 μm x 30 μm) degraded from the measurements taken right after passivation to 4 weeks later, were we see the dark current density increased by factor of 5.

Finally, we concluded the chapter with a novel passivation technique of that of chlorine doped ZnTe. Even though ECP had lower dark current density than ZnTe:Cl, chlorine doped ZnTe had better long term stability and better integration into FPA fabrication.

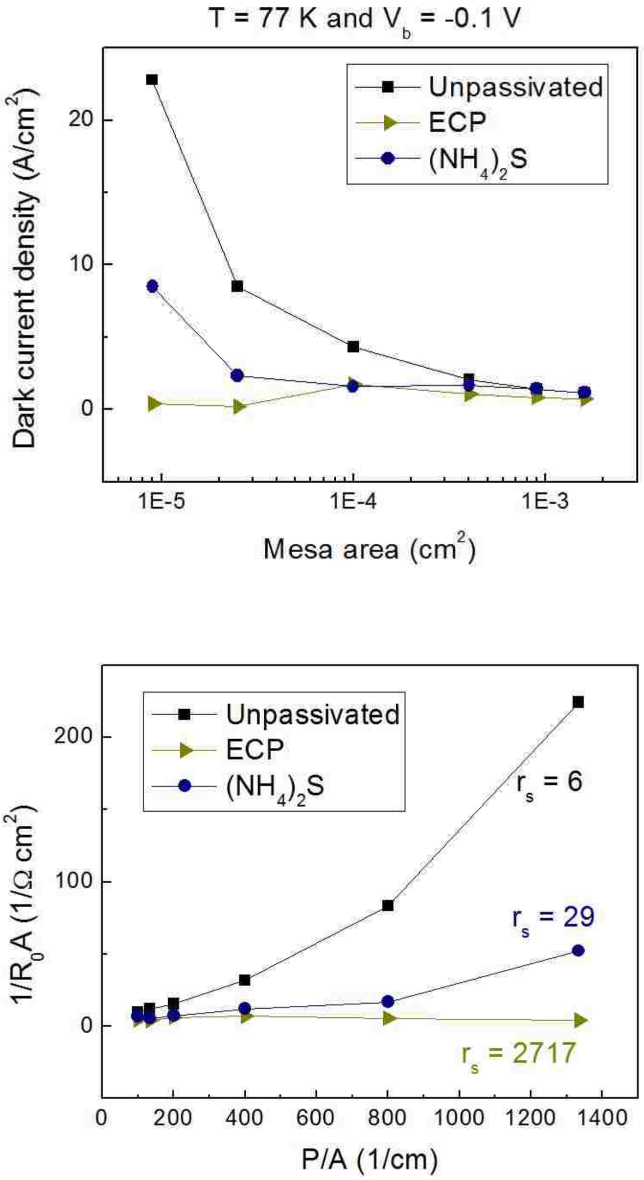

Figure 5.12: (Top) Dark current density vs mesa area of unpassivated and passivated by ECP and ammonium sulfide SLS detector with pBiBn design measured at 77 K. (Bottom) Dependence of dynamic resistance-area product at zero bias vs (P/A) ratio for unpassivated, $(NH_4)_2S$ and ECP passivated variable area diodes at 77 K of pBiBn detector.

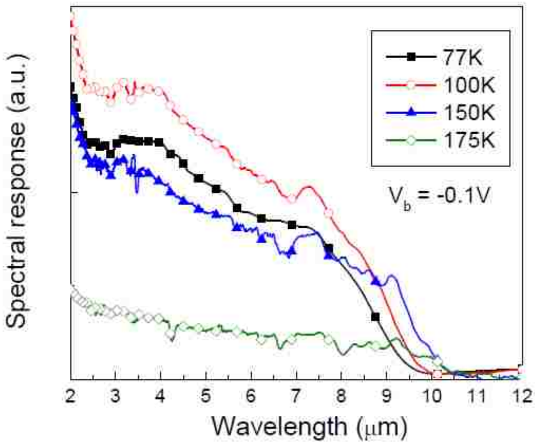

Figure 5.13: The representative normalized spectral response curves for various temperatures measured at -0.1V of applied bias at various temperatures.

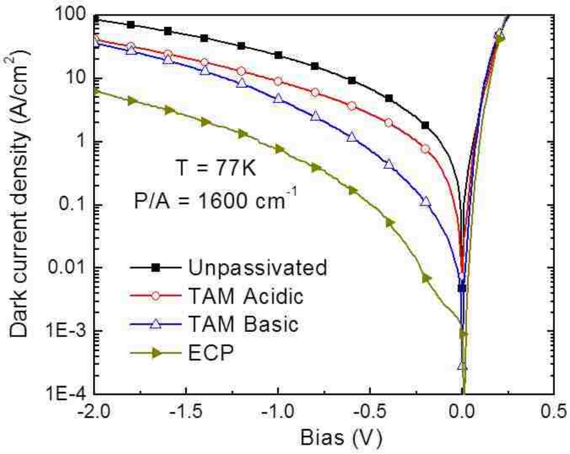

Figure 5.14: Comparison between dark current densities of as-etched and treated by different passivations devices with perimeter-to-area ratio (P/A) of 1600 cm^{-1}.

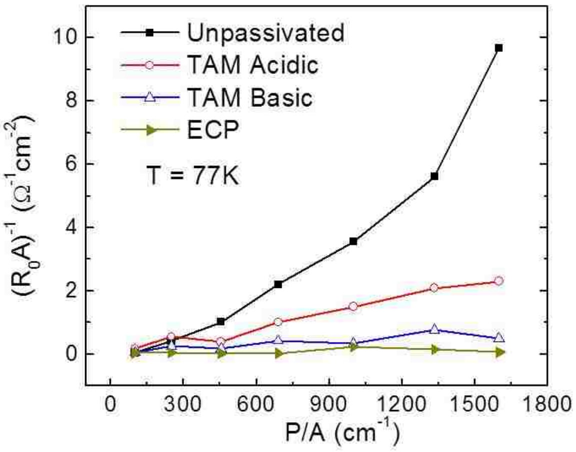

Figure 5.15: Plot of R_0A vs. the perimeter-to-area ratio (P/A) for unpassivated and passivated by various treatments SLS detectors measured at 77 K.

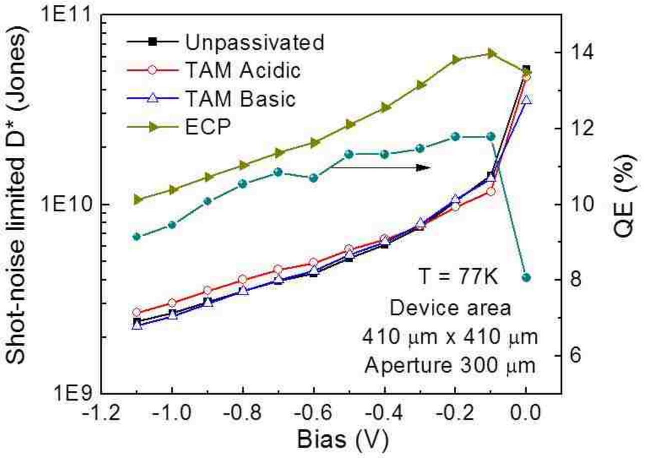

Figure 5.16: The shot-noise limited D* as a function of applied bias for as-fabricated and treated by various passivations detectors evaluated at 77K

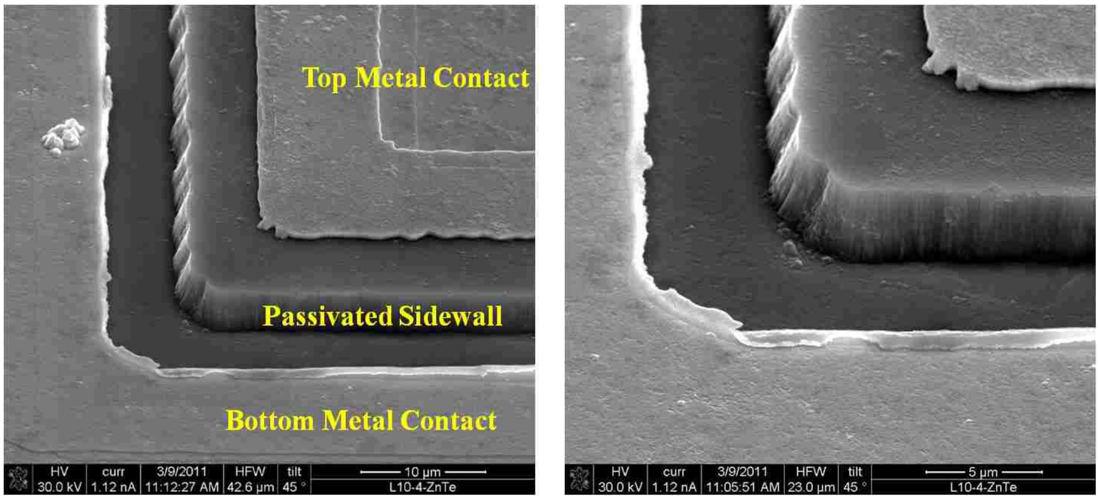

Figure 5.17: SEM images of ZnTe passivated InAs/GaSb SLS detectors showing the highly uniform deposition of ZnTe.

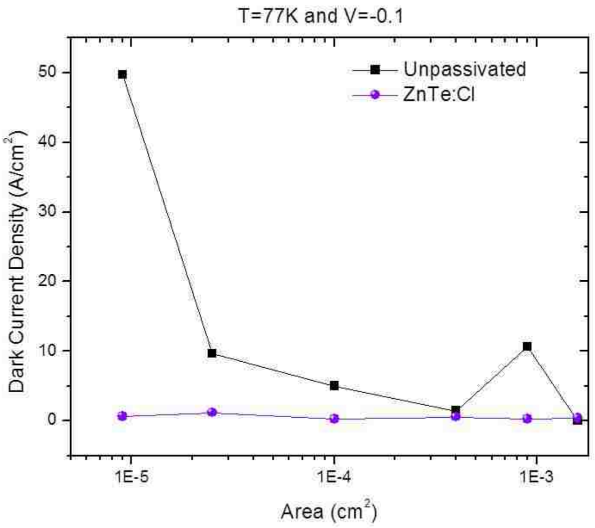

Figure 5.18: Dark current density vs. mesa area of unpassivated and ZnTe passivated on pin architecture of InAs/GaSb SLS heterostructure.

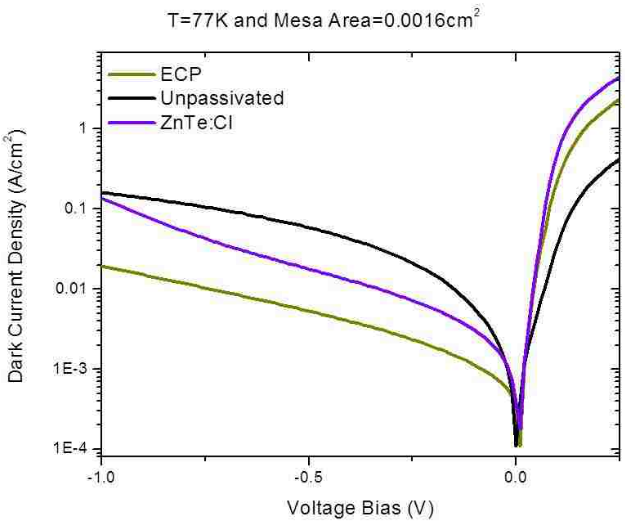

Figure 5.19: Dark current density vs. voltage bias of unpassivated, ECP and ZnTe passivated on graded-gap W-design SLS heterostructure.

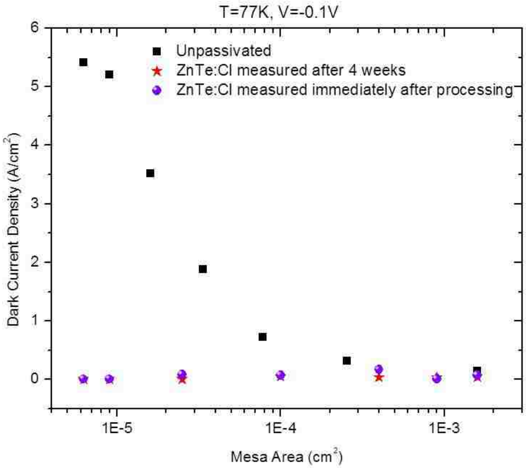

Figure 5.20: Dark current density vs. mesa area of unpassivated and ZnTe passivated on graded-gap W-design SLS heterostructure at T=77K and V=-0.1V.

Chapter 6

Conclusions

The main objective of this work is the investigation of surface chemistry of InAs/GaSb SLS and development of effective mesa delineation and passivation techniques for IR single-element detectors and FPAs based on this material system. SLSs have gained a lot of interest in the past two decades due to the inherent advantages over present-day detection technologies. In particular, the type-II InAs/GaSb SLS are characterized by large electron effective mass which leads to smaller leakage currents and higher detectivity; higher quantum effciciency originates in inter-miniband transitions stipulating normal incidence absorption; adjustable bandgap provide tunable cut-off wavelength and, in turn, multicolor capacity of FPAs based on InAs/GaSb SLs. Moreover, by appropriate variation of layer thickness and composition it is possible to tailor the light-hole and heavy-hole band separation to suppress Auger recombination with consequent increase in carrier lifetime.

In chapter 1 of this dissertation the general concepts of IR detection were introduced followed by the brief description of IR detector types (photon and thermal). Pros and cons of competitive IR technologies based on interband and intersubband detectors were described and compared with alternative technology for IR detection based on type-II InAs/GaSb SLS. The next section in the chapter established the motivation behind the research work presented in this dissertation. Lastly, the chapter summarizes the contributions made in the dissertation.

Chapter 2 briefly describes the three different architectures of Type-II SLS LWIR detectors used during the course of this work and they are (i) p-i-n design, (ii) pBiBn design, and (iii) graded bandgap 'W' structure. The second part of chapter briefly introduces the characterization techniques used in this work, namely (1) Material characterization and (2) Electrical characterization. The material characterization saw two Categories: (i) Bulk material quantification methods such as HR-XRD, TEM and (ii) Surface material characterization such as AFM, SEM, EDX and XPS. The electrical characterization section explained the principles behind spectral response measurements, dark current densities, surface resistivities, responsivity measurements, quantum efficiency and specific detectivity calculations.

Chapter 3 reviewed mechanisms of surface oxide formation on exposed sidewalls of InAs/GaSb SLS detectors as well as various passivation techniques of SLS detectors operating in different regions of IR spectrum reported by various research groups. The extensive analysis of available literature on passivation of SLS detectors showed that there are various passivation techniques developed for passivation of MWIR and LWIR InAs/GaSb SLS detectors. However, there is no universal approach developed yet that would treat equally efficiently the SLS detectors with different cut-off wavelengths. Moreover, more studies have to be conducted on interface quality between SLS detector sidewall and passivation coating in order to better understand the chemistry underlying various passivation schemes. Finally, since passivation needs to be successfully integrated into FPA fabrication procedure, more research on compatibility of various passivations, especially sulfur-based, with FPA fabrication, has to be performed.

Chapter 4 was devoted to our efforts on development of an optimized etch for the mesa delineation of SLS detectors. We have examined the surface of etched mesa sidewalls of InAs/GaSb LWIR (50% cutoff wavelength is 14 μm) detectors after conventional BCl_3-based plasma assisted etch, chemical etch (H_2O_2:HCl:H_2O= 1:1:4), and a combination of both the etches. Contradictory to our expectations, we found that the smoothest sidewall profile with reasonable undercut was obtained after chemical etch alone. Plasma-assisted etch generated a lot of damage; in particular, etch residues and a two-step sidewall profile were observed.

Next, we have studied sidewall profiles of 24 μm x 24 μm mesas etched on InAs/GaSb SLS LWIR (50% cutoff wavelength is 14 μm). The optimized chemical etch (H_2O_2:HCl:H_2O= 1:1:4) showed significant lateral etch (9 μm each side) and hence rendering itself unpractical for FPA fabrication. Plasma-assisted etch resulted in smooth vertical sidewalls of individual FPA pixels free from any etch residuals with no undercut (with respect to mask) observed. Application of chemical etch subsequent to the plasma assisted etch was expected to further smooth the sidewalls; however, it resulted in undercut estimated to be 8 μm on each side of FPA mesa, which is not acceptable for the subsequent FPA fabrication steps. Thus, we found that the plasma-assisted etch is the only acceptable method for fabrication of small dimension mesa structures in high fill-factor FPAs based on InAs/GaSb SLS.

The objective of chapter 5 was to understand the effect surface modifications make on performance of InAs/GaSb SLS MWIR and LWIR detectors utilizing the common IR detectors figures of merit, i.e., responsivity, quantum efficiency, dynamic impedance area product, surface resistivity and specific detectivity. We found that the sulfur-based passivations, the ammonium sulfide passivation and electrochemical sulfur passivation (ECP), significantly improved performance of pin and pBiBn LWIR (100% cut-off wavelength of $\sim$ 12 μm at 77K) SLS detectors.

The dark current density was decreased by factors of 200 and 25 (pin detector) and $\sim$ 3 and 54 (pBiBn detector), respectively, compared to the unpassivated devices (T = 77 K, -0.1 V of applied bias). The specific detectivity D^* was improved by a factor of two and by an order of magnitude for $(NH_4)_2S$ and ECP passivated pBiBn detectors.

Application of sulfur-based passivation on graded-bandgap LWIR detectors resulted in values of $r_{surface}$ equal to 1.7 x 10^2, 6.8 x 10^2, $\sim$ 3 x 10^3, and 1.4 x 10^5 Ωcm for the unpassivated, TAM acidic, TAM basic, and ECP passivated detectors, respectively, revealing three orders of magnitude improvement of $r_{surface}$ for ECP treated devices at 77 K.

The drawback of ECP is that, due to its delicate 50Å thick sulfur deposition, it peels-off over time, hence degrading the performance of the device. Also, due to its delicate nature, ECP is impractical to be incorporated into FPA fabrication. Hence we proposed and implemented a novel ZnTe:Cl passivation in this dissertation. ZnTe being a chalcogenide behaves similarly to sulfide passivation by forming covalent bonds with the abruptly terminated InAs/GaSb SLS crystal lattice. On the graded-bandgap \`W´design, ECP showed a superior surface resistivity (r_s) of 10^5 Ω -cm over ZnTe:Cl passivation with r_s =6700 Ω-cm and unpassivated r_s=156 Ω -cm at 77K. Then, during the course of a month, ZnTe:Cl passivation showed almost no degradation, where as dark current density of ECP at 77K and applied bias=-0.1V, went from 0.5A/cm^2 to 1A/cm^2 in on a 1E-4cm^2 device in 4weeks. Since these are our initial experiments with ZnTe:Cl passivation, further calibration experiments need to be run in order to improve quality of the passivant and then its performance can probably surpass that of ECP.

In conclusion, we developed optimized etch procedure for the single-element large-area InA/GaSb SLS detectors and showed that plasma-assisted etch is only alternative for the fabrication of SLS FPAs. Performance of LWIR detectors with pin, pBiBn, and graded-bandgap designs passivated by dielectric, organic, and chalcogenide-based passivation were investigated and compared. We found that electrochemical sulfur passivation (ECP) effectively passivated SLS detectors with all investigated designs and was superior compared to other passivation treatments. Finally, to find an alternative to long-term unstable ECP, we implemented novel ZnTe:Cl passivation in the InAs/GaSb SLS LWIR detectors. This MBE grown technique is robust, uniform deposition, that can be incorporated into FPA fabrication and gives the detectors long term stability that can take these type-II SLS based LWIR detectors to commercialization.

Chapter 7

Future Work

We have in the past chapters explored the options of implementing existing technology such as SiO_2, SiN_x, SU-8, ECP passivation schemes into our studies, but also pushed the envelope with novel etch techniques and passivation schemes such as ZnTe:Cl onto SLS heterostructure. Regardless of the various advantages the SLS technology offers over existing InSb, QWIP, MCT IR technologies, such as normal incidence absorption, uniform and economical material growth, multicolor operation, reduced tunneling currents and suppressed Auger recombination, they have yet to fulfill their promise of superior performance [107]. The SLS still demonstrate dark current densities significantly higher than that of bulk MCT detectors especially in the MWIR regime. After decades of research, the search for the ideal passivation scheme still remains elusive. Hence, in this dynamic field of research new innovations to improve the performance of SLS bulk system and to reduce surface effects are always around the corner. In this chapter we describe a few experiments that were carried out as a part of this research that pushes the envelope a little bit by exploring the charge carrier mechanisms at the surface of InAs/GaSb SLS LWIR detectors along with an investigation into the passivation mechanisms at the interface of passivant and the InAs/GaSb SLS LWIR detector surface. We hope these studies can there-of lay a path out to develop new solutions to existing problems.

In this chapter we first look at an alternative IR device architecture called the gated or the 3-terminal architecture. This structure gives us the access to manipulate interface between the passivation layer and semiconductor surface by introducing charge carrier into it by a metal contact on the passivant. In the second half of this chapter, we will look at a few of the emerging techniques to study the surface material and mechanism of the passivant, the exposed surface and sidewall of the InAs/GaSb based SLS and the interface of the passivant and InAs/GaSb based SLS.

7.1 IR detector with Gated/3-Terminal Architecture

The ultimate objective of our work presented here is to reduce the surface leakage currents such that it does not overwhelm the crucial bulk dark current mechanisms. Previously we have looked at various etch and passivation techniques for LWIR SLS mesa-isolated IR detectors to reduce surface roughness, residual by-products and deterrent native oxides, there by suppressing surface leakage currents. Presented here is a technique first proposed by F. Fuchs et al in 1998 [37] wherein they deposited a gate metal on their dielectric layer that passivated the large-area InAs/(GaIn)Sb SL photo-diodes as shown in Fig 7.1. As seen in the graph of Fig 7.2, they reported a significant change in the current density by varying the gate voltage. At gate voltage of -1.25V they observed the maximum suppression of tunneling currents by 4 orders of magnitude. The authors attribute this to the compensation of the work function of gate metal and the semiconductors (InAs/(GaIn)Sb SL) at V_G=-1.25V.

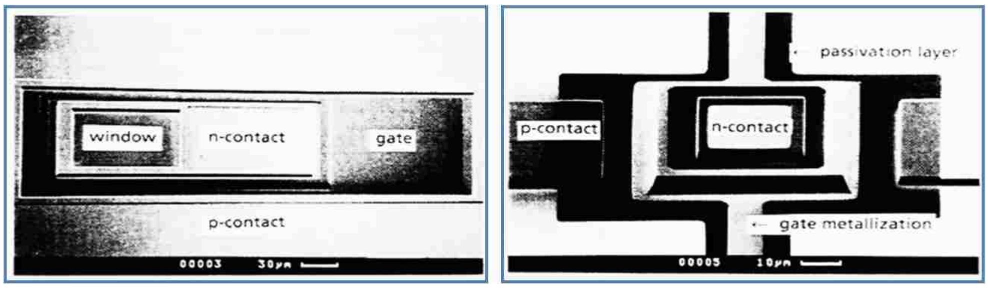

Figure 7.1: SEM images of the gate metalized diodes. The gate metal can be seen surrounding the n-contact in left image and on the sidewalls on the right image. Images are reproduced from [37].

G. Chen et al [22, 24] applied the gated diode technique to their SiO_2 passivated MWIR T2SLS p-π-M-n heterojunction Fig. 7.3. Figure 7.4 depicts the electrical performance reported by the authors. They indicate that at V_G=0V, the gated diodes (GDs) are leakier than the unpassivated diodes (UPDs) and ungated diodes (UGDs). The authors infer that this could be due to the difference in workfunction

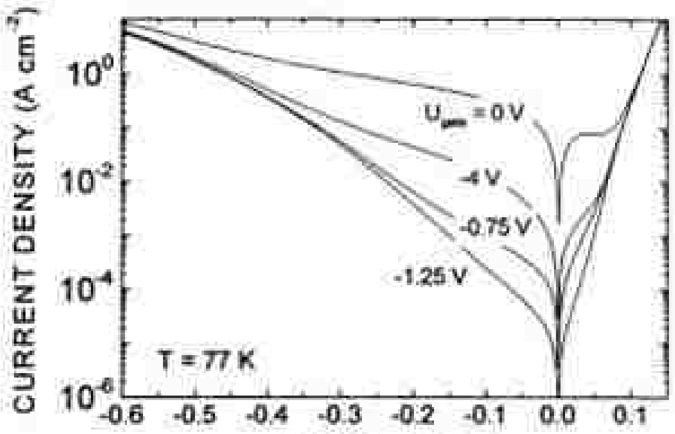

Figure 7.2: The I-V characteristics of a gated InAs/(GaIn)Sb SL photo-diode . Image is reproduced from [37].

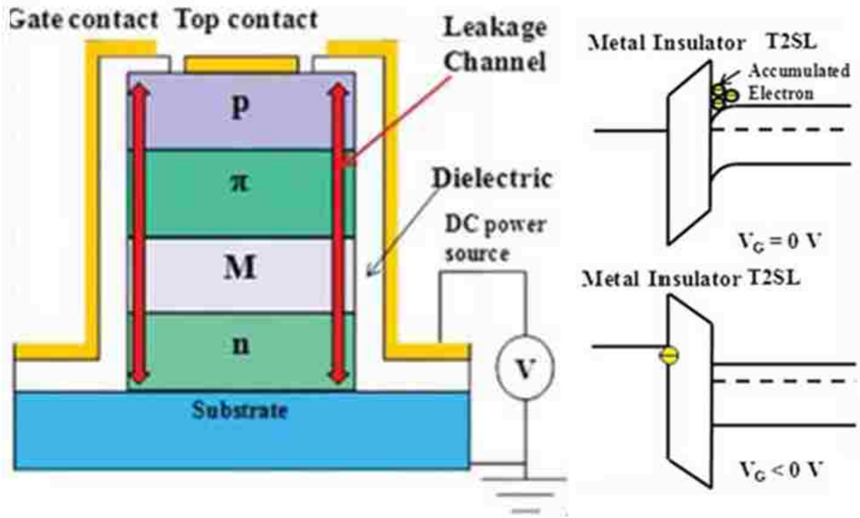

Figure 7.3: (Left side) Schematic of a gated diode fabricated on MWIR T2SLS p-Π-M-n heterojunction. (Right side) Band diagram indicating charge transport mechanism at the SiO_2-T2SLS interface. Images are reproduced from [22, 24].

of the metal and semiconductor causing band bending at the interface leading to additional electron accumulation (as seen in Fig. 7.3) and hence increased surface leakage currents. Now when a negative gate bias is applied to these diodes, they see a significant improvement in performance and saturates at V_G=-40V. At this gate voltage they ascertain that all accumulated electrons at the SiO_2-SLS interface are repelled thus establishing flat band condition at the mesa sidewalls and suppressing surface leakage currents.

7.1.1 Growth and Fabrication of SiO_2 passivated IR detectors with 3-Terminal architecture

We implemented the gated diode technique on our pBiBn detector structure Fig 7.5. The detector structure has 800 nm thick (200 periods) 9 ML InAs/4 ML GaSb SLS

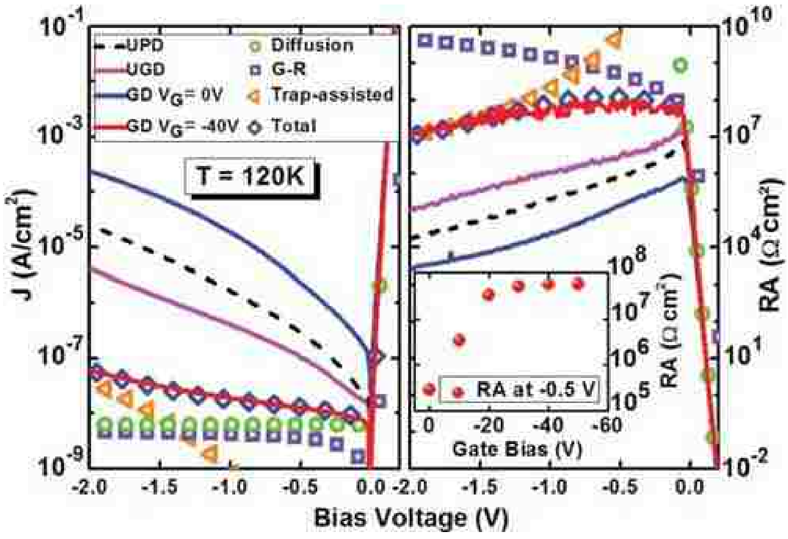

Figure 7.4: Electrical characteristics of ungated, gated and unpassivated diodes at T=120K. Images are reproduced from [22].

n-type contact layer doped with Te (n = 3 x 10^{18} cm^3) followed by non- intentionally doped (n.i.d.) hole blocking (HB) layer consisting of 275 nm thick 16 ML InAs/4 ML AlSb SLS (45 periods). Then a 1.94μm thick (300 periods) p-doped (p=1E16cm^3) absorber region of 14ML InAs/7ML GaSb SLS is grown. Next, n.i.d 149 nm (45 periods) thick electron blocking (EB) layer made of 7ML GaSb/4ML AlSb SLS is deposited and 130 nm (38 periods) thick p-type contact layer made of 5 ML InAs/8ML GaSb doped with Be (p = 2.8 x 10^{18} cm^3) completed the structure. In the detector structure SLSs were grown with imposed InSb interfaces in order to balance the strain. The normalized spectral response of the pBiBn detector was measured with a glow-bar source within the FTIR spectrometer and is shown in Fig 7.6. It shows a cut-off wavelength of 11μm.

In order to fabricate IR detectors with 3-terminals, we designed a new mask set as shown in Fig 7.7.The fabrication process of the SiO_2 passivated gated diodes is similar to the processing of passivated 2-terminal devices except for the last

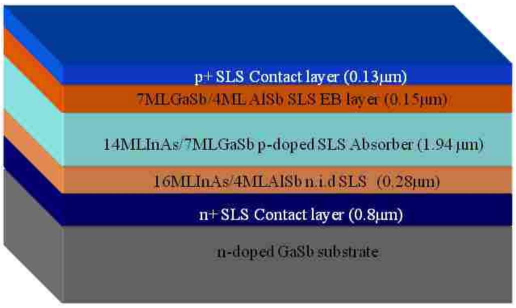

Figure 7.5: Schematic of the pBiBn structure.

step of depositing passivation metal of Ti/Au (detailed in Appendix C). Figure 7.8 shows a cross-sectional schematic of a completed 3-terminaled SiO_2 passivated gated diodes. Figure 7.9 shows the SEM image of a completed 3-terminaled SiO_2 passivated gated diodes. It indicates a complete coverage of the passivated sidewall by the passivation contact metal along with the clear areas of where SiO_2 is removed and hence inferring ideal fabrication of the 3-terminaled SiO_2 passivated

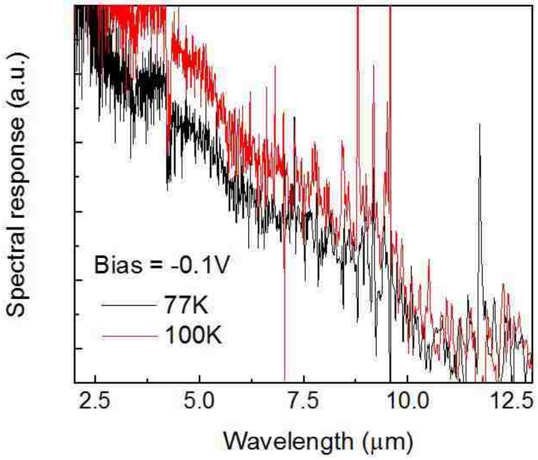

Figure 7.6: Spectral response of the pBiBn detector measured at 77K and 100K at a applied bias of -0.1V.

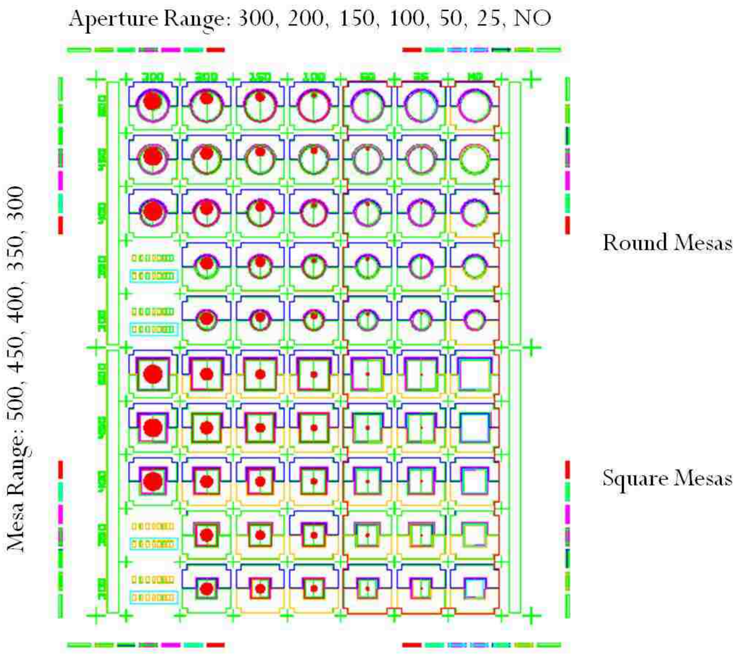

Figure 7.7: CAD-screen shot image of the mask set implementing the 3-Terminal architecture.

gated diodes.

7.1.2 Performance of SiO_2 passivated IR detectors with 3-Terminal architecture

The I-V measurements were then performed on the variable temperature Janis ST-500 micromanipulated probe station at 77K and under zero field of view. A third probe was used to contact the gate contact and it was connected to an Agilent power supply to provide the gate voltage. The microscope images taken in the probe station, with and without the probes are shown in Figures 7.10 and 7.11.

The results of the electrical characterization are shown in Figures 7.12 and 7.13.

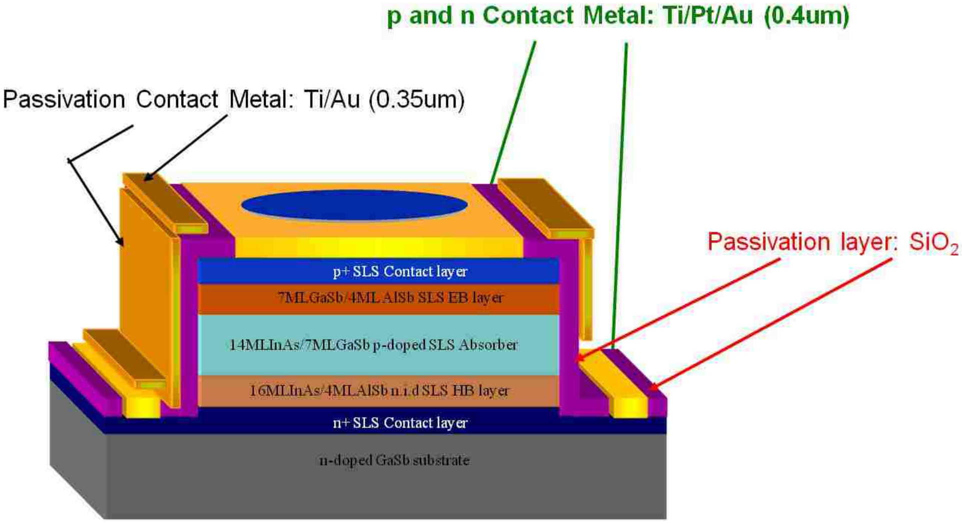

Figure 7.8: Cross-sectional schematic of a completed 3-terminaled SiO$_2$ passivated gated diodes.

In Fig 7.12, we see the results of a 3-terminal SiO$_2$ passivated gated diode with

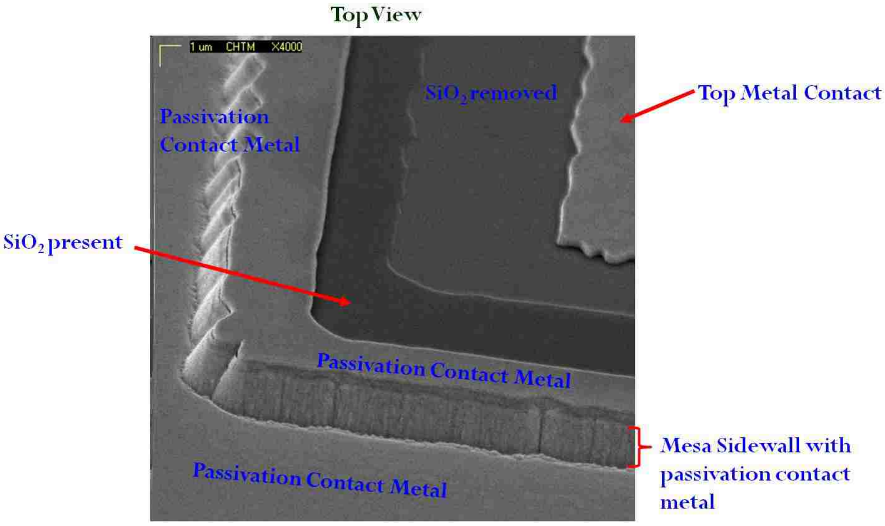

Figure 7.9: SEM image of a completed 3-terminaled SiO$_2$ passivated gated diodes.

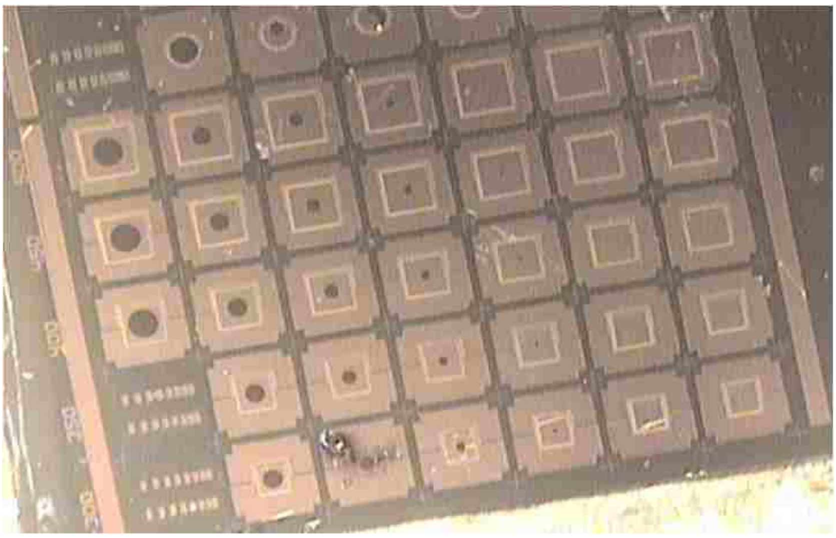

Figure 7.10: A top view probe-station microscope image of a completed 3-terminaled SiO_2 passivated gated diodes with square mesas.

square mesa size of 500μm and no aperture. It was subjected to gate bias from -10V to +10V and under ungated condition. Under ungated condition wherein the gate probe was not connected and a regular 2 probe diode I-V measurement was carried out. It should be noted that when V_G=0V, the 3rd probe is connected but the voltage supplied is zero. Fig. 7.12 indicates that ungated condition had the lowest dark current density (J_d) of 0.0136 Å/cm^2 at applied bias of -0.1V and applying gate bias seems to worsen the device performance. Moreover, negative gate bias performed worse (with V_G=-10V having the highest J_d of 0.0163 Å/cm^{2}at applied bias of -0.1V) than positive gate bias. Additionally all the positive gate bias data are gathered together along with V_G=0V at J_d 0.02 Å/cm^2 at applied bias of -0.1V, indicating there was no change on varying the positive gate bias.

Fig 7.13 shows the results of a 3-terminaled SiO_2 passivated gated diode with square mesa size of 400μm and no aperture along with J_d of unpassivated device. This device was subjected to gate bias of 0V to -14V. Here we clearly see the

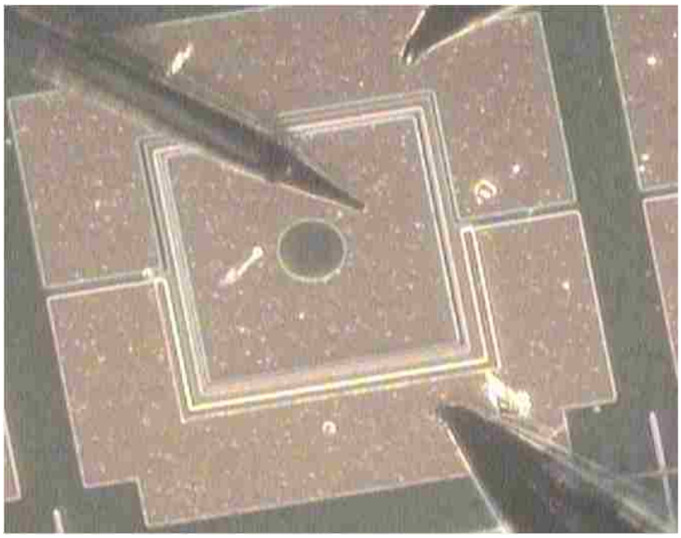

Figure 7.11: A top view probe-station microscope image of a completed 3-terminaled SiO_2 passivated gated diode (square mesa size of 400μm and aperture diameter of 100μm) with all three probes attached.

advantage of SiO_2 passivation as unpassivated device had the highest J_d. Once again the ungated condition showed the lowest J_d of 0.0139 Å/cm^2 at applied bias of -0.1V and applying gate bias seems to worsen the device performance. Both devices overloaded at V_G=-15V and was irreversible due to the damage to the gate contact Fig 7.14.

In our case, the unpassivated devices showed worse J_d than gated, hence we can deduce that our devices did not have any difference in work function between metal and semiconductor. Our goal for this experiment was not just to reduce surface leakage currents but also to investigate the charge transport mechanism at the interface of a passivant. G. Chen et al [22, 24] have indicated that there is an accumulation of electrons at the interface and if it is indeed so, then do they get neutralized by the trap states in a SiO_2 passivation? We have not seen evidence of that. In our devices, positive gate biases do not make a change, but negative biases

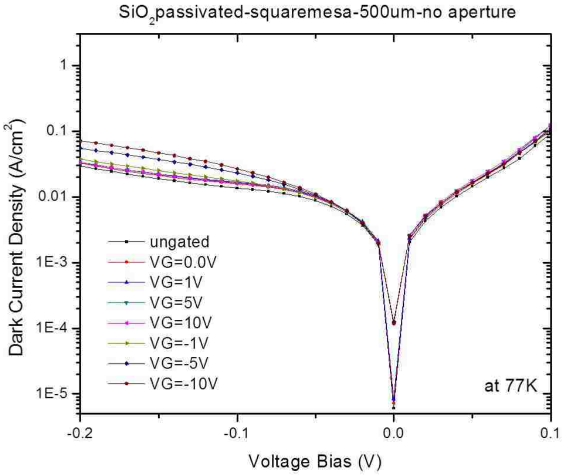

Figure 7.12: Dark current density vs. voltage bias under gate bias from -10V to +10V and under ungated condition of a 3-terminaled SiO_2 passivated gated diode (square mesa size of 500μm and no aperture). All measurements performed at 77K and zero field of view.

do. As more and more negative gate voltage is applied, there is further increase in surface leakage currents; this means there is more accumulation of charge carriers at the interface of SiO_2 and semiconductor. This condition can happen when the SLS is behaving as a p-type semiconductor and the charge carriers are holes. This goes against the conclusion of G. Chen et al [22, 24] and hence has to be further studied.

Moreover, our devices never reached flat band conditions and the reasons for these observations need to be further investigated. It could be that pBiBn is too complicated a system to make accurate inferences as each layer could function as a semiconductor entity in itself. Also the mesas sizes available to us in this mask were from 500μm to 300μm, which are too large to accurately infer surface effects. In our future work, we intend to make a new mask set with smaller mesas than 300μm. Also the thickness and quality of SiO_2 must be optimized.

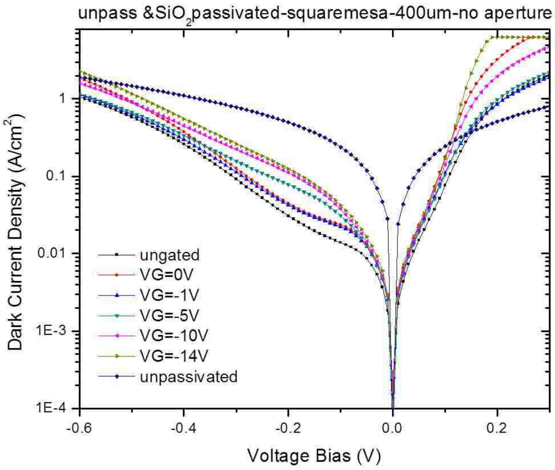

Figure 7.13: Dark current density vs. voltage bias under gate bias from 0V to -14V, under ungated condition and unpassivated. All gated bias measurements performed of a 3-terminaled SiO_2 passivated gated diode with square mesa size of 400μm and no aperture and at 77K with zero field of view.

7.2 Surface Material Characterization

In this section, we once again come back to the question of how to quantify passivation? The complication arises because, the choice of a passivant is dependent not only on the function of making a surface passive (inactive), but also on the material being passivated/surface states/dangling bonds/defects it has to interact with. This raises the question of the mechanism of passivation-if a passivant simply envelopes a surface, hence depriving its interaction with atmosphere or if it has to form chemical bonds hence becoming the part of the structure itself? Additionally, if both cases are possible, then which is a better passivant- an encapsulant or a chemically bonding passivant?

In the chapter 5, we explored the path of electrically quantifying a passivation. This section explores our attempt to answer these fundamental questions posed

Figure 7.14: A top view probe-station microscope image of a completed 3-terminaled SiO_2 passivated gated diode (square mesa size of 400μm and no aperture) under overload condition, with all three probes attached.

above by taking a closer look at the interface of a passivant and the InAs/GaSb superlattice structure. Here we study the material make up of each passivant available to us along with their interactions with GaSb, InAs, InSb individually and with SLS material as one whole entity. The accessibility to material characterization techniques such as X-ray photoelectron spectroscopy (XPS) and Energy Dispersive X-Ray spectroscopy (EDX) have give us determinable data to recreate the atomic interaction of each passivant with the InAs/GaSb SLS structure.

7.2.1 Energy Dispersive X-Ray spectroscopy (EDX) measurements on various passivation techniques on InAs/ GaSb SLS devices

Energy Dispersive X-Ray spectroscopy (EDX/EDS) is an analytical tool found on most Scanning Electron Microscopy (SEM) instruments that is used for chemical or elemental analysis of a specimen. This tool operates under the assumption that each element has its own unique atomic make-up and hence this allows the X-rays emitted which are a distinguishing feature of an element's atomic structure and would be unique to the element and hence identifiable. During the emission of X-rays from the sample as it stops the streaming electron beam, the ``balloon-shaped´´primary volume of excitation (i.e. the Brehmsstrahlung sphere volume) within the sample expands with increasing the energy of the e-beam by higher voltages applied on the cathode source. The size of the primary volume of excitation varies from 0.5 to 3μm in diameter as well as in depth within the sample. Since the X-rays are emitted as a result of the loss of kinetic energy of the electron beam at this ``expanding volume-element´´, the differences in the EDX peak intensities for the constituent chemical elements point to compositional heterogeneity between the near-exterior (sub-surface) region as compared to the deeper regions of the specimen(SLS). It must be noted that the EDX spectrum presented in this section is plotted with X-ray energy (in keV) on the X-axis and the intensity (in counts) on the Y-axis. For the purpose of our measurements we used the JEOL 5800LV SEM, equipped with an Oxford Analytical ultrathin-window EDS and an Oxford Isis 300 X-ray analyzer attached to the microscope. It must be noted that we used automated analyses feature on tool and its analytical software provides semi- to fully quantitative EDS analysis down to boron.

The SLS samples utilized had 14ML InAs and 7 ML GaSb per period with the p-i-n design. The complete description of this structure is given in Section 5.2, as we employed the same specimens used for the comparison of various passivation techniques on pin design of the SLS detector. The different passivation techniques along with their fabrication details are summarized in Table 7.1. The results of the electrical characterization are shown in Fig 7.15. During the course of progression of this section we will use a few terminologies to describe different regions in our structures and they are illustrated in Figures 7.16, 7.17 and 7.18. Structure A shown in Fig 7.16 is an unpassivated InAs/GaSb SLS detector, whereas Structure B (shown in Fig 7.17) is passivated with passivant removed at the aperture and from the metal contacts. Finally, Structure C (shown in Fig 7.17) is where the passivation is applied at the end of the fabrication process and hence is present throughout the sample.

In the aperture region in all cases, where there is no passivant, the EDX spectrum have the dominance of Ga and As peaks at lower excitation voltages(e.g. 5keV) whereas the intensities of In and Sb peaks are the highest for the 30keV spectra in all the cases. The terminating part of the specimen towards the surface has dominance of Ga and As, considering the EDX of the aperture region registered at 5keV for all the cases, as compared to the conspicuous In and Sb peaks along with those of Ga and As in lesser prominence at 30keV.

1. InAs/GaSb SLS device passivated by Silicon Nitride

   The first passivation technique we measured under the EDX is the silicon nitride (SiN_x) and the resulting structure is Structure B. The plots at the aperture are shown in Fig 7.19 for X-ray energies 5kev (left side) and 30keV (right side). In the unpassivated aperture region, the EDX peaks of Ga & As are dominant with no Si- peak at 5keV excitation. This indicates that the EDX can distinguish the regions without the passivant. At high excitation voltage (30keV), the X-ray emission peaks from the bulk constituents dominate i.e.

Table 7.1: Summary of all the passivation techniques which were characterized under the EDX.

Passivation Technique	Pre-Passivation Treatment	Deposition Technique	Temperature of deposition	Final Thickness
SiN_x	H_3PO_4:H_2O_2:H_2O (1:2:20)-20sec dip	PECVD	300°C	2000Å
SiO_2	H_3PO_4:H_2O_2:H_2O (1:2:20)-20sec dip	E-beam-evaporator	170°C	2000Å
ZnS	H_3PO_4:H_2O_2:H_2O (1:2:20)-20sec dip	E-beam-evaporator	RT	2000Å
SU-8	H_3PO_4:H_2O_2:H_2O (1:2:20)-20sec dip	Spun	RT	1.5μm
$(NH_4)_2S$	-	Wet bath -20% $(NH_4)_2S$:H_2O (1:4)-120 min dip	RT	50-100Å
ECP	H_3PO_4:H_2O_2:H_2O (1:2:20)-20sec dip	Wet bath-Na_2S in Ethylene glycol-charged	RT	50Å

Ga, In, Sb and As with no Si-peak. Presence of N and/or O peaks (closely spaced) of lower intensities persist at the aperture region due to surface reactions while handling the specimens.

The plots at the passivated mesa sidewall are shown in Fig. 7.20 for excitation X-ray energies 5kev (left side) and 30keV (right side). It must be noted that the EDX plots for passivated top, side-wall and the bottom regions of the mesas at excitation voltages 5keV and 30keV are all similar. The total coverage of SiNx as a passivant is evident from the dominant peaks of Si and N at the passivated top, side-wall and the bottom regions of the mesas at lower

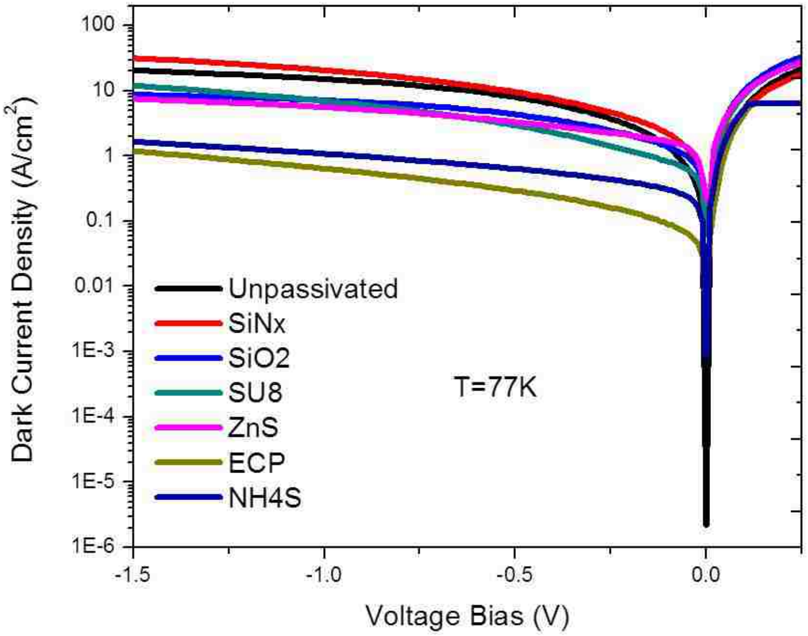

Figure 7.15: Dark current density vs. applied voltage of various passivation techniques carried-out on pin design of the SLS detector.

excitation voltage (5keV). The marking of Au very close to the Si peak arises from the very-thin film of gold coating on insulator often used for avoiding the charging effects.

The predominance in intensities of In and Sb peaks indicates that these constituents have higher contents in the interiors of the SLS specimens used in the present EDX studies. More significantly, the peaks of Si and N, discernible in the 30keV EDX from the top, bottom or side-wall of mesa, do not have constant ratio in relative intensities. In all these regions, the peak intensity of Si is higher than that of N which is in contrast to the EDX of Si_3N_4 (bulk) with higher intensity for N- peak than that of Si. The stoichiometric ratio of

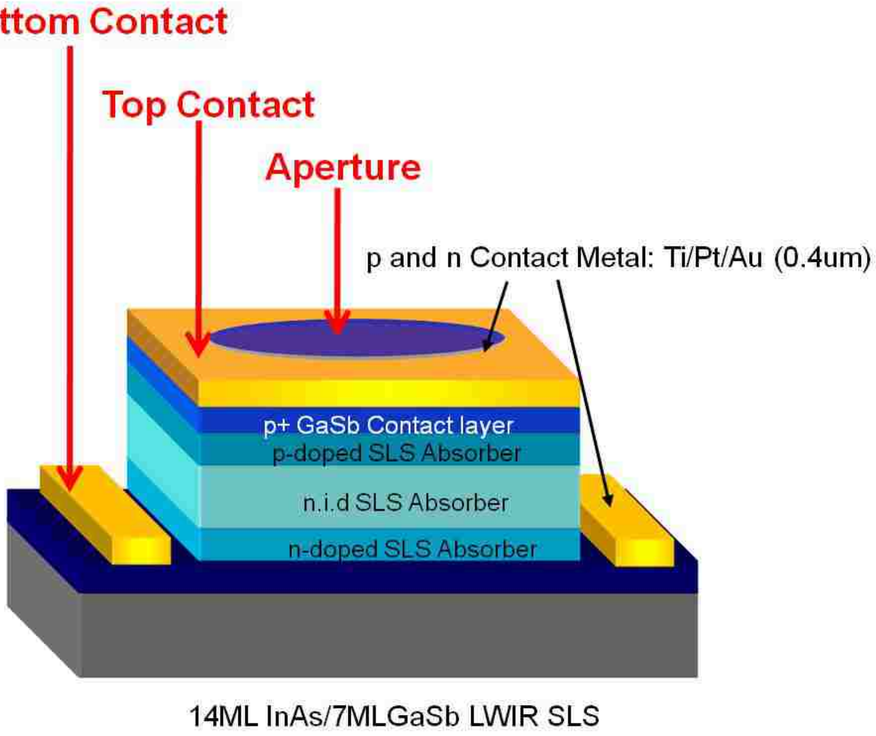

Figure 7.16: Heterostructure schematic of InAs/GaSb SLS detector with p-i-n architecture with no passivation and we call it as `structure A´.

the two chemical constituents, therefore, does not correspond to 1: 1.33 (i.e. of Si_3N_4) .The passivant layers are more of SiN_x where x<1.33.Prevalence of non-stoichiometry in silicon nitride thin films are reported in literature wherein the films are either amorphous or partially-crystalline. The structural disorder caused by increasing nitrogen content on silicon network is accompanied by changes in electrical properties from semiconductor to insulator behavior.

Considering the dielectric films of Si-N compounds as the passivant layer, minor compositional deviations arise from the formation of point-defects, i.e. atomic vacancies or interstitials. The point defects can trap electrons

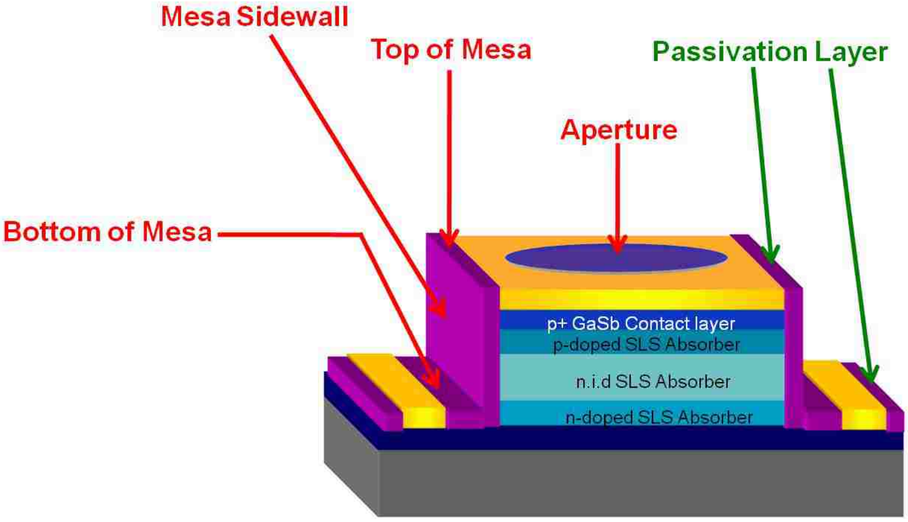

Figure 7.17: Heterostructure schematic of InAs/GaSb SLS detector structure with p-i-n architecture with passivation and we call it as `structure B´.

(or holes) to retain electro-neutrality. In the present case, the N-vacancies (anion vacancies) can trap electrons. As a result, accumulation of electrons at the insulator-semiconductor (SLS) interface is possible leading to band bending as talked about in the previous section. The performance of SiN_x as a passivant can be judged from the surface leakage currents i.e. in comparison to the dark currents with other passivants and this is seen in Fig 7.15. It shows SiN_x having poor dark currents and this could be due to the non-uniform SiN_x deposition leading to large presence of N-vacancies.

2. InAs/GaSb SLS device passivated by Silicon dioxide

The next passivation technique we measured under the EDX is the silicon di oxide (SiO_2) and the resulting structure is again Structure B. It must be noted that the EDX of the aperture region as well as the SiO_2 passivated top, sidewall and bottom regions of the mesa were all registered under the same condition of 30keV and they were all similar. The plots at the aperture (left

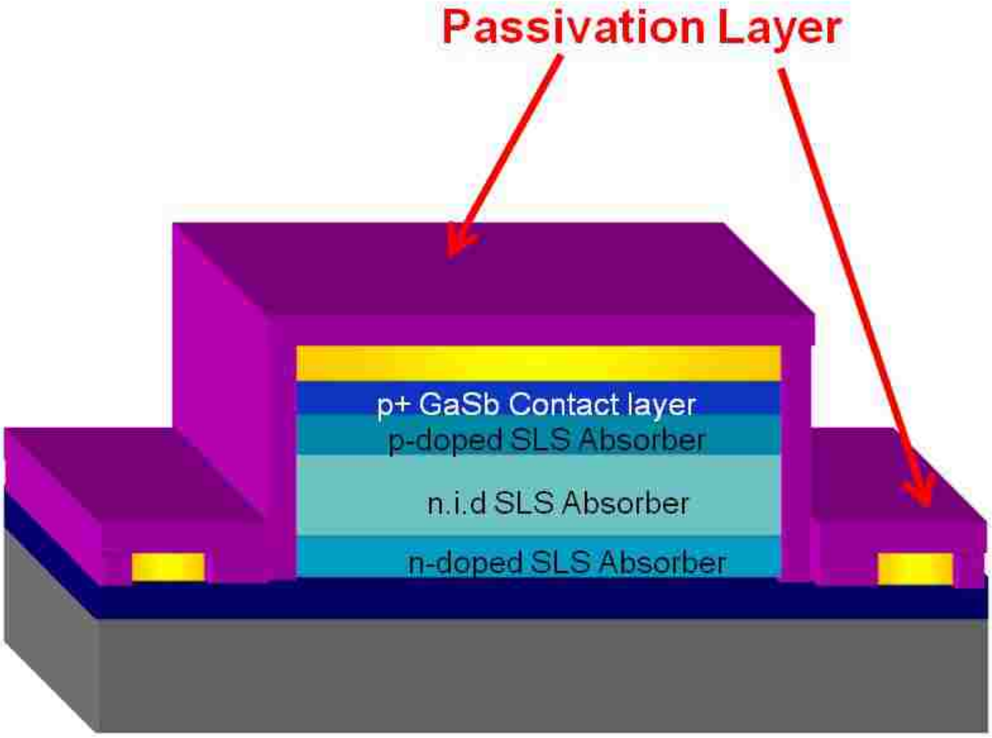

Figure 7.18: Heterostructure schematic of InAs/GaSb SLS detector structure with p-i-n architecture with passivation and we call it as `structure C´.

side) and sidewall (right side) are shown in Fig 7.21 for x-ray energy 30keV. The EDX of SiO_2 passivation layers is apparently more complex because of the possible surface chemical reaction between the passivant and the SLS under the conditions of SiO_2 deposition particularly the oxygen partial pressures. At the aperture region without the passivant, there is no indication of the presence of Si although O-peak of minor intensity is observed. The latter arises from the incipient formation of native oxide film. The presence of the high intensity peaks of In, Sb, Ga and As along with the Si and O peaks of medium weak intensities indicates the robustness of silicon oxide of thickness ∼200 nm. This is because of the higher stability of the passivant

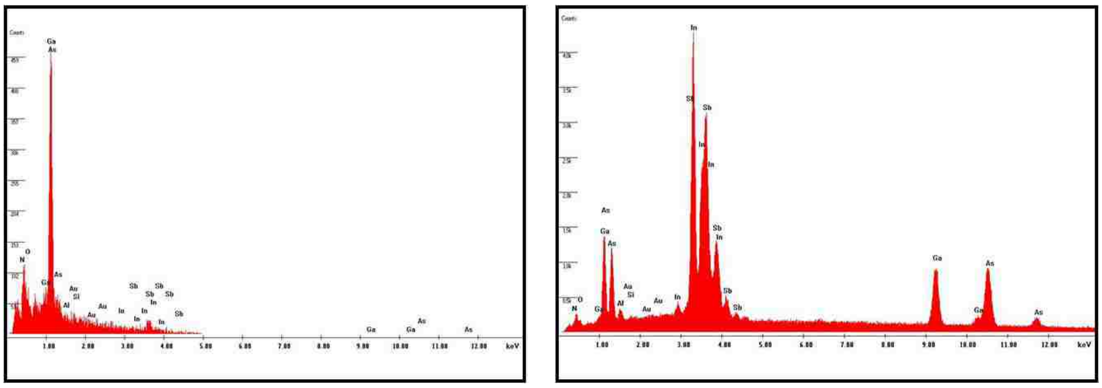

Figure 7.19: EDX plots of SiNx passivated InAs/GaSb SLS detector structure with p-i-n architecture at the aperture of the device and at x-ray energy (left side) 5keV, (right side) 30keV.

oxide having different Si: O ratios. Of these, silicon monoxide of apparent chemical composition, SiO, and silicon dioxide, SiO_2, are the two well known phases. In the early stages of the oxide deposition, Si: O ratio is quite off-set from the 1:2 as in SiO_2. This is very evident from the higher relative intensity of the Si- peak as compared to the O-peak intensity in the EDX spectra from

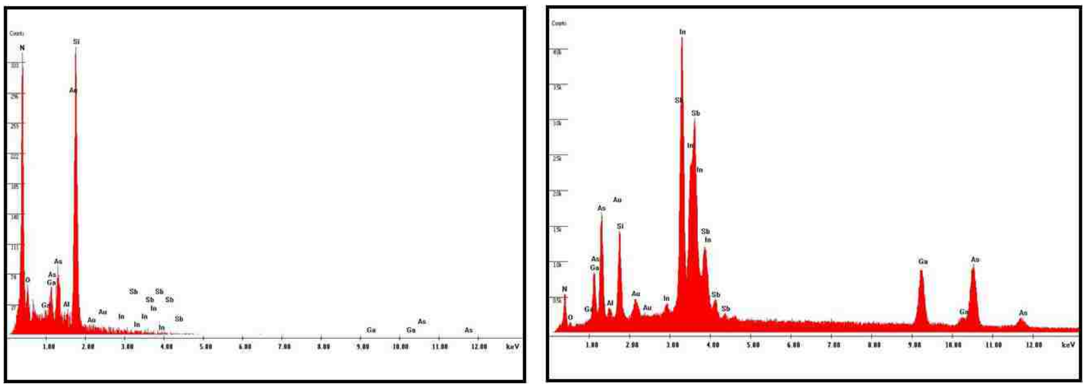

Figure 7.20: EDX plots of SiNx passivated InAs/GaSb SLS detector structure with p-i-n architecture at the sidewall of the mesa and at x-ray energy (left side) 5keV, (right side) 30keV.

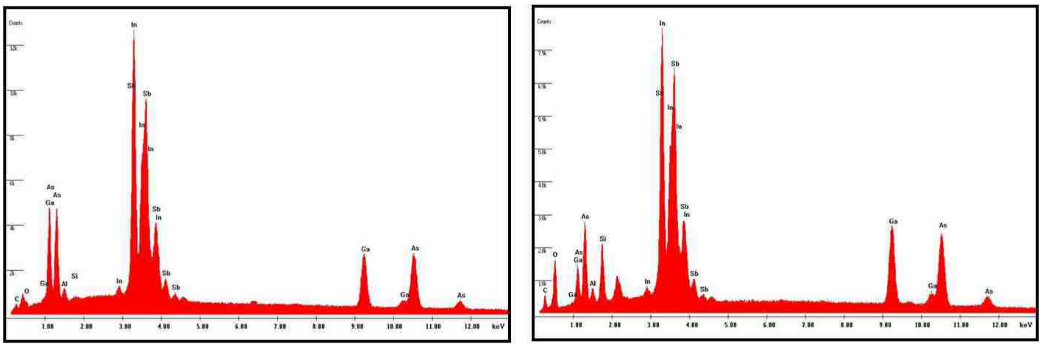

Figure 7.21: EDX plots of SiO_2 passivated InAs/GaSb SLS detector structure with p-i-n architecture at the aperture (left side) and sidewall (right side) at x-ray energy of 30keV.

all the passivated regions. Higher intensity of Si in comparison to that of O peak is not usual for the EDX of SiO_2 (bulk). Formation of oxygen-vacancy related electron traps is envisaged whose role in modifying the electrical properties of the insulator-semiconductor interface can be accounted for, on the same line as of SiNx proposed above. However, the difference is that the sub-oxide of silicon has definite field of stability and may have preferential formation due to the catalytic effects on the surfaces of T2SL layers as well as on other Group-III antimonides. It has to be noted from Fig 7.15, that SiO_2 passivation behaved better than SiN_x and unpassivated. This shows that SiO_2 deposition was more uniform and did not have the formation of oxygen-vacancy related electron traps as seen in SiN_x. It has to be noted that non-stoichiometric silicon oxide deposited at low gaseous pressures show semi-insulating properties and that SiO_x non-stoichiometric films having x<2 formed by low pressure chemical reaction.

3. InAs/GaSb SLS device passivated by SU-8

   In our next study, we measured EDX on SU-8 passivated InAs/GaSb SLS detector structure with p-i-n architecture and the resulting structure is again

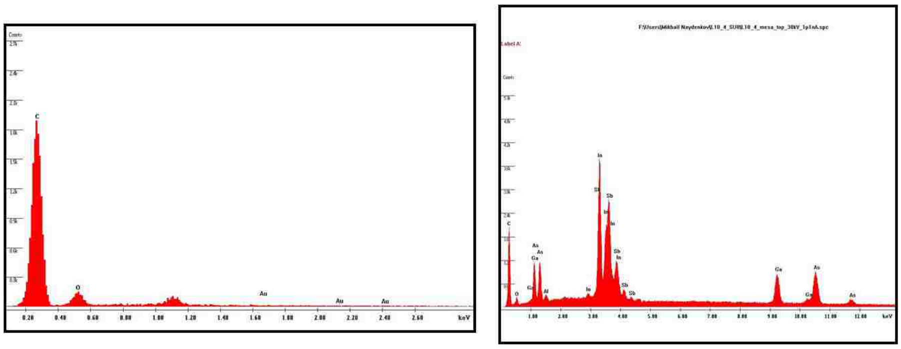

Figure 7.22: EDX plots of SU-8 passivated InAs/GaSb SLS detector structure with p-i-n architecture at the top of mesa and at x-ray energy (left side) 5keV, (right side) 30keV.

Structure B. The results are plotted in Fig 7.22 that shows EDX measurements of SU-8 passivated InAs/GaSb SLS detector structure with p-i-n architecture at the top of mesa and at x-ray energy (left side) 5keV, (right side) 30keV. The passivation with SU-8 photoresist involves much thicker films (1500 nm, in the present case) than those of the previous passivants. The peaks of C and O are persistent in all the EDX spectra recorded at 5 as well as 30keV as also from different location, i.e. top, side-wall or bottom of the mesa. As expected for the epoxy resin polymers, the intensity of C-peak is very strong as compared to that of O-peak. If fluorine is indeed present in the structure, then F-peak is not discernible since the concentration of the photo-acid generator (SbF_5 giving rise to $HSbF_6$, in this case) is only a few percentage by weight. Significantly, the C: O peak intensity ratio remained unchanged in all these cases indicating that the chemical composition of the cured polymer is the same at the interface or in the interior region of the passivation layer.

The EDX spectra of the aperture region as seen in Fig 7.23 have no C or O peak even when registered at 30keV. The EDX of the top, side-wall and the

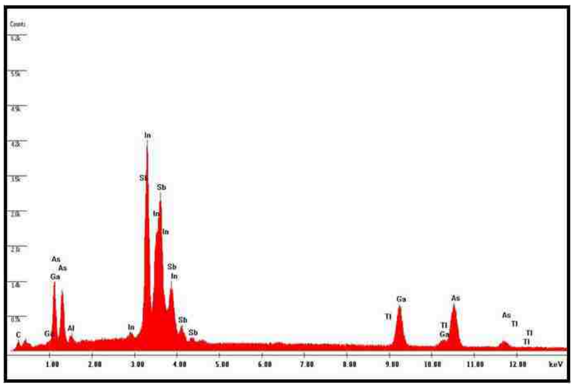

Figure 7.23: EDX plots of SU-8 passivated InAs/GaSb SLS detector structure with p-i-n architecture at the aperture and at x-ray energy of 30keV.

bottom of the mesa at 30keV have total identity to the EDX of the aperture at 30keV barring the C and O peaks for the former. These results point to the fact that SU-8 photoresist is more of an encapsulant than a chemical passivant.It has to be noted from the J_d graph of Fig 7.15, that SU-8 performs better than SiNx and unpassivated and on par with SiO_2 passivation on our devices. This brings to wonder the effectiveness of dielectric passivants. We can conclude in more finality only after more EDX is carried out on varied thicknesses of these 3 passivation techniques.

4. InAs/GaSb SLS device passivated by ZnS

   In our next experiment, we measured EDX of ZnS passivated InAs/GaSb SLS detector p-i-n architecture and the resulting structure is once again Structure B. It is evident from Fig 7.24, that there is very small peak of sulfur and no sign of Zn at all. This indicates that we were successful in removing all traces of ZnS from the aperture area and the remaining sulfur presence is due to the compounds that sulfur forms with the T2SLS structure to form complex sulfides. The EDX results indicate the robustness of ZnS as a passivant since the peaks of Zn and S persist at 5keV as well as 30keV excitation in Figures 7.24 and 7.25. However the relative intensity of S is much lower than that of Zn peak in the 5keV excitation of top, side- wall or bottom of the mesa. The intensity of S-peak has slightly increased in all the EDX spectra registered at 30keV, yet much lower than that of Zn. It is evident that Zn/S ratio is not uniform throughout the specimen. The Zn-excess films of ZnS have more S-vacancies which act as electron trap centers. The unique feature in this case is that both Zn (p-type) and S (n-type) are active dopants in III-V semiconductors and can compensate mutually the charge- trapping centers at the insulator-semiconductor interface. This makes the situation with ZnS as passivant different from that of SiN_x and SiO_2. It also emphasizes the distinctiveness between encapsulant and chemical passivation of sulfides/chalcogenides. It has to be noted from the J_d graph of Fig 7.15, that ZnS performs better than unpassivated and SiN_x, but on par with SiO_2 and SU-8 passivation techniques on our devices. Another feature of ZnS films is their degree of crystallinity since the amorphous as well as crystalline films are reported [8], [118]. These films are known to have variable Zn: S ratios being modified by the post-depositional annealing in suitable atmospheres. Another feature of ZnS films is their degree of crystallinity since the amorphous as well as crystalline films are reported in the electroluminescent (EL) devices based on ZnS. These films are known to have variable Zn: S ratios being modified by the post-depositional annealing in suitable atmospheres.

5. InAs/GaSb SLS device by Ammonium Sulphide [$(NH_4)_2S$]

   In our 5th investigation, we measured EDX of ($(NH_4)_2S$ passivated InAs/GaSb SLS detector structure with p-i-n architecture and the resulting structure is Structure C. Here the passivant deposition is the last step in the fabrication process and the passivant is not removed from the aperture are and is present on top of metal contacts. Hence the EDX of aperture, top of mesa, mesa sidewall and mesa bottom regions are all the same. Ammonium sulfide

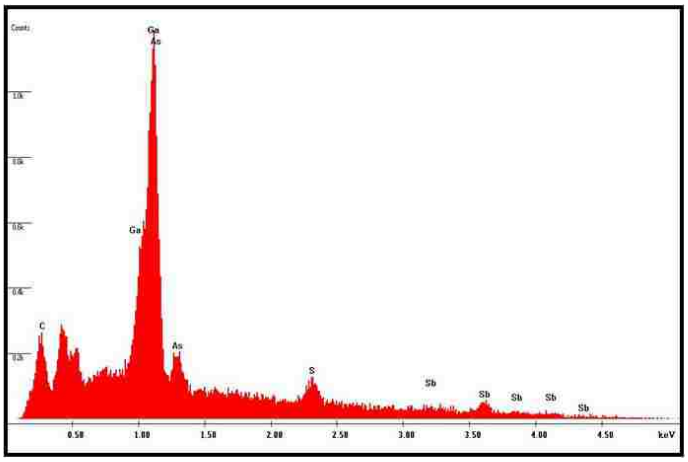

Figure 7.24: EDX plots of ZnS passivated InAs/GaSb SLS detector structure with p-i-n architecture at the aperture and at x-ray energy of 30keV.

as a passivant for SLS under the suitable solvent media is expected to result in: (i) removal of native oxide layer from the surface and (ii) formation of a chemisorbed passivating layer of sulfur atoms that are coherently bonded to In and/or Ga atoms on the surface. The EDX results as seen in Figures 7.26 and 7.27 do not show the presence of the O-peak whereas the low intensity

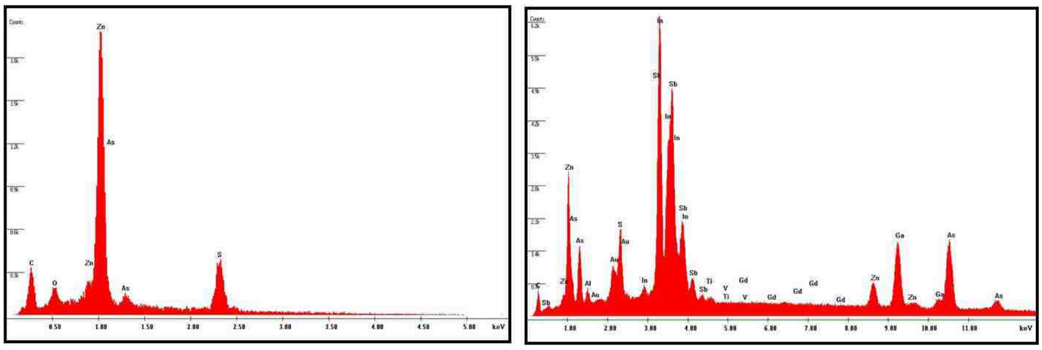

Figure 7.25: EDX plots of ZnS passivated InAs/GaSb SLS detector structure with p-i-n architecture at mesa sidewall and at x-ray energy of (left side) 5keV, (right side) 30keV

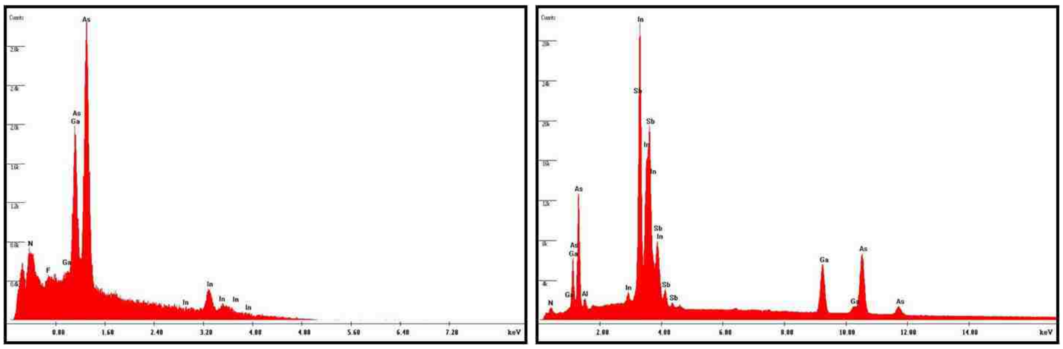

Figure 7.26: EDX plots of $(NH_4)_2S$ passivated InAs/GaSb SLS detector structure with p-i-n architecture at the aperture and at x-ray energy of (left side) 5keV, (right side) 30keV.

N-peak is discernible. The S-peak is conspicuously absent indicating that a continuous coherent sulphur layer is not stabilized within the apparently thin layer, 5 to 10nm, of passivation.

The EDX spectrum of the aperture region as seen in Fig 7.26 has the same features as in the cases of previous passivants under both 5keV as well as 30keV excitation. This indicates to the accuracy of the EDX registry. The presence of N-peak is indicative of either strong chemisorptions of NH_4^+ cation or its dissociation leading to the incorporation of N-atoms in the surface region. Ammonium sulfide treatment seemingly tends to etch the SLS rather than deposit the sulfide layer. Yet another possibility is the instability of thin sulfide layer under the vacuum conditions used for EDX observations.From the J_d graph of Fig 7.15 we can infer that $(NH_4)_2S$ performs better than unpassivated and SiN_x, SiO_2, SU-8 and ZnS passivation techniques on our devices. The next question that still arises is why a wet bath based $(NH_4)_2S$ works better than an e-beam evaporated ZnS? It could be that the non-uniformity of ZnS deposition is a significant factor than we had previously assumed. This can be established only by further comparative study of EDX and electrical

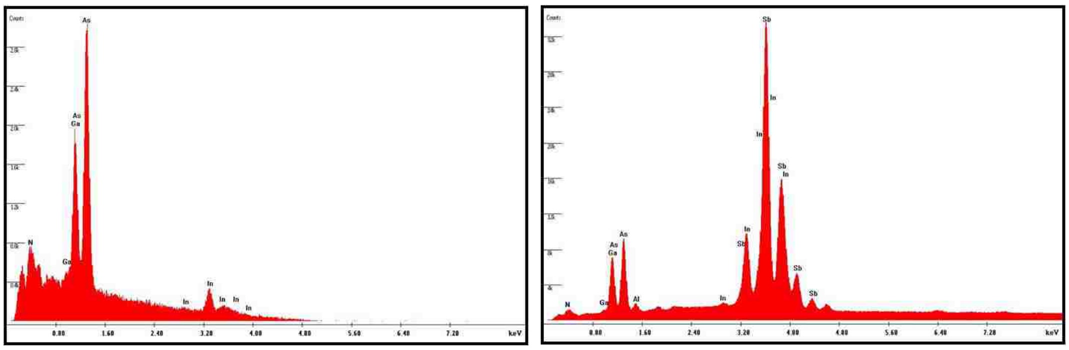

Figure 7.27: EDX plots of $(NH_4)_2S$ passivated InAs/GaSb SLS detector structure with p-i-n architecture at the bottom of the mesa and at x-ray energy of (left side) 5keV, (right side) 30keV.

measurements of wet and dry deposited ZnS and $(NH_4)_2S$.

6. InAs/GaSb SLS device by Electrochemical passivation (ECP)
   In our last experiment, we measured EDX of ECP passivated InAs/GaSb SLS detector structure with p-i-n architecture and the resulting structure is once again Structure C. Wherein the passivant is not removed from the aperture are and is present on top of metal contacts. Hence the EDX of aperture, top of mesa, mesa sidewall and mesa bottom regions are all the same. On this device, the EDX was performed on the mesa sidewall at excitation x-ray energies (i)5kev (ii)10keV and (iii) 30keV as seen in Fig 7.28. Electrochemical passivation is carried out in the ethylene glycol medium using sodium sulfide, Na_2S, as the electrolyte at pH >10 and may contain the polysulfide such as Na_2S_2, Na_2S_3 and so on, in very low concentrations. In this process, the SLS specimens are placed on the anode and together with the inert cathode (usually Pt) are dipped into the electrolyte. Under the constant current densities (galvanostatic conditions), the passivant layer of sulfur (element) or sulfide (compound) will be deposited on the anode. Electrochemical oxidation may proceed partially at least depending on the current density used. Unlike in

aqueous solutions, the electrolyte dissociation is limited in organic solvents, Na_2S in ethylene glycol in the present case, and thereby requiring higher voltages to attain the desirable current densities. Changes in oxidation state takes place of sulfide ions as also of the elemental constituents present at the near interface region of SLS. The products so formed need not be dissolving into the electrolyte medium particularly in the organic solvents due to limited solubility. The EDX spectra of specimens exposed to the electrochemical passivation (ECP) have to be studied from these perspectives. The EDX of mesa regions subjected to ECP have strong peaks of Na and O whereas the S- peak has lower intensity at different electron excitation voltages. These results point not only to the diminished concentration of sulphur but also the increased presence of O and Na. The latter being a strongly electropositive element ought to be present as cations. The electrochemical product such as sodium dithionite($Na_2S_2O_4$) is formed by the anodic oxidation reaction involving sulfide,S^{2-}, ions and the intermediate sulfite, ${SO_3}^{2-}$, ions and deposit along with the sulfur layer during the electrochemical passivation in ethylene glycol . Sodium dithionite is a stable compound at totally solvent-free, vacuum conditions. This could explain how a 50-100Åof ECP passivation is able to so successfully suppress surface leakage currents. The residual solvent and the pyrolysis thereof in a vacuum will account for the C-peak of low intensity in the EDX of mesa side- walls. This effectiveness of suppressing surface leakage currents is established from the J_d graph of Fig 7.15 that shows ECP performs better than unpassivated and SiN_x, SiO_2, SU-8, ZnS and $(NH_4)_2S$ passivation techniques on our devices.

In summarizing this section, the EDX results point to the thin film formation of non-stoichiometric SiN_x or SiO_x on the SLS devices as passivation layers. The compositions of these films need to be optimized by controlling the thin film deposition conditions to attain the lowest surface leakage currents. The extended compositions thereof such as SiN_xO_y or SiAlON may function as passivant layers. The sulfur treatments particularly $(NH_4)_2S$, leads to etching and thereby removing the native oxides and satisfy the surface bonds with chemisorbed sulfur atoms. However this does not lead to long term stability. The ECP generates more complex surface products from the organic solvent based sulfides. Future experiments on EDX study must be carried out meticulously to study the effects of varying passivant thicknesses, passivant deposition conditions and other types of passivation techniques.

7.3 Conclusions

In this chapter we first explored the charge carrier mechanisms at the surface of InAs/GaSb SLS LWIR detectors by fabricating a 3-terminal SiO_2 passivated InAs/GaSb LWIR SLS with pBiBn design. The goal of this experiment was to obtain ideal passivation effect i.e. reach flat band conditions at the surface by manipulating the charge carrier transport using the metal contact on the passivation layer. This structure forms a metal/oxide/ semiconductor (InAs/GaSb SLS) region. But our devices do not reach flat band conditions at the application of the gate voltage, therefore further investigation must be carried out to improve the quality of SiO_2, re-design the mask and utilize a simpler bulk material such as InAs/GaSb LWIR SLS with pin design.

The second half of this chapter delved into the investigation of passivation mechanisms at the interface of passivant and the InAs/GaSb SLS LWIR detector surface by surface material characterization method of EDX. Here we performed EDX measurements on InAs/GaSb LWIR SLS with pin design passivated with (i) SiN_x, (ii) SiO_2, (iii) SU-8, (iv) ZnS, (v) $(NH_4)_2S$ and (vi) ECP. These experiments show that non-stoichiometric SiN_x, and SiO_2 form effective passivants only when they are substantially thick layers. EDX shows that SU-8 seems to behave as an encapsulant, and its superior performance than the dielectrics must be further investigated by varying all three thicknesses. ZnS is certainly a chemical passivant but its Zn to S ratio was not uniform throughout the sample and that may explain it poor performance compared to other chalcogenides. We could also infer that $(NH_4)_2S$ passivation is effective due to mild etching at the surface leading to removal of native oxides and chemisorbed S-atoms lead to termination of dangling bonds. But EDX on $(NH_4)_2S$ passivant showed S-peak conspicuously absent indicating that a continuous coherent sulphur is not stabilized with the 5-10nm thin passivation layer. Finally EDX on ECP lead to the inference that there is the formation of sodium dithionite ($Na_2S_2O_4$) along with deposition of sulphur layer at the surface of InAs/GaSb SLS device. Sodium dithionite is a solvent-free, stable compound even under vacuum conditions and this could explain the effectiveness of ECP, but further material study has to be carried out to confirm these propositions.

Looking back at chapters 5 and 7,there can be many forms of tests to study the surface of a complex structure of InAs/GaSb LWIR SLS, such as images by HR-SEM/TEM; compositional data from EDX, XPS, AFM, HR-XRD, device characterization. As this is ongoing research, there are bound to be many more techniques worked on by other groups. In conclusion, there is no one shibboleth, in the end, our complete understanding of the physics and chemistry of SLS surfaces can be determined only by a combination of results from many catechisms and analyses. Finally, on a larger scale, the penultimate contribution of this body of work is that it shows the complex mechanisms existing on surfaces of compound structures such as InAs/GaSb LWIR SLS and that they cannot be further ignored as we scale down in device/component and hence instrument sizes. In conclusion, we end this oeuvre by stating that the research for high-efficiency, affordable IR detectors with state of the art bulk material continues as does the quest for an ideal surface.

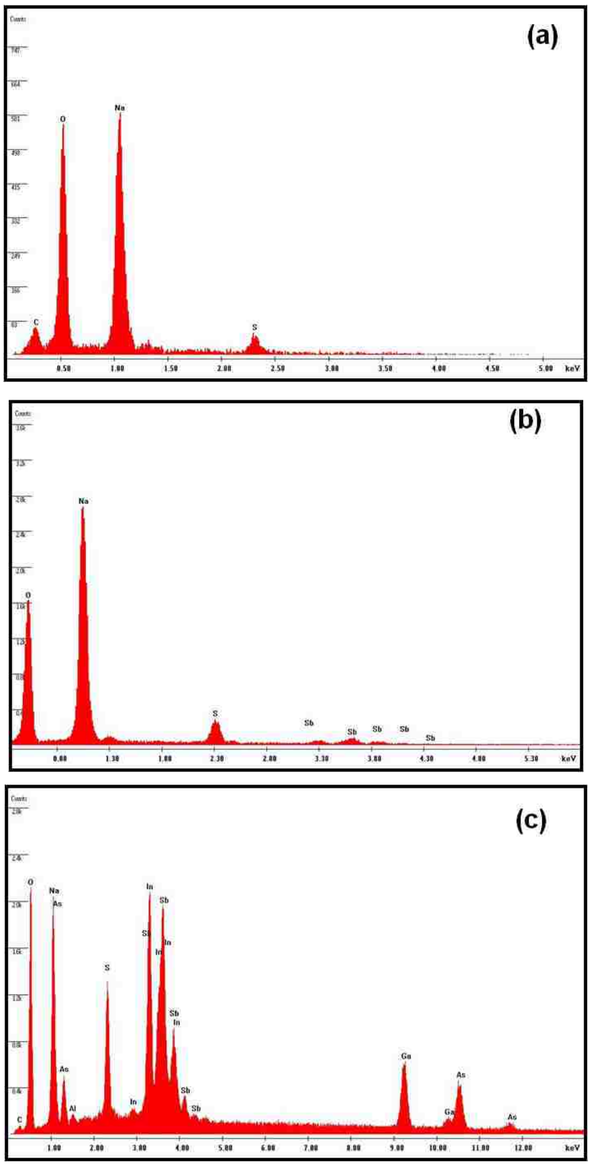

Figure 7.28: EDX plots of $(NH_4)_2S$ passivated InAs/GaSb SLS detector structure with p-i-n architecture at the mesa sidewall and at x-ray energy of (a) 5keV, (b) 10keV and (c) 30keV.

Appendices

Appendix A

Fabrication Procedure of a single pixel InAs/GaSb SLS Detector

The following fabrication procedure was utilized for single pixel InAs/GaSb SLS based detectors with p-i-n, pBiBn and graded-W structure designs. The fabrication process for the single-pixel InAs/GaSb SLS detectors includes following steps: (1) mesa isolation etch, (2) top and bottom contact metallization, and (3) passivation. Each of processing steps is described below in details.

1. Mesa isolation etch
    (a) **Post-MBE Growth/Pre-Mesa Etch Treatment:** The wafer must typically be pretreated before resist application in order to obtain a smooth, uniform coverage of the photoresist to the wafer. The first step in the pretreatment is the cleaning and a dehydration bake.
        i. The wafer is cleaned consecutively in acetone, isopropanol (IPA) and de-ionized (DI) water (5 minutes each) and then blow-dried with nitrogen (N_2).

    ii. The dehydration bake is performed at 150°Cduring 6 minutes. This step is intended to drive off most of the adsorbed water on the surface of the wafer. A dehydration bake is also effective in volatilizing organic contaminants, further cleaning the substrate. At 150°C, it is estimated that about one monolayer of water remains on the surface.

  (b) **Application of Photoresist:** We used light sensitive photoresist to lay down the pattern for our mesa etch which defines the size of the detector.

    i. Immediately following the bake the wafer is primed with hexamethyldisilazane (HMDS), which acted as an adhesion promoter. Liquid HMDS is applied directly to the wafer by dispensing a fixed volume and spinning the wafer to spread out the liquid to a very thin uniform coating. For spinning on the HMDS wafer is mounted on a vacuum chuck. Torque is applied to the chuck to rapidly accelerate in with rotational speed of 5000 rpm during 30 seconds. One monolayer of HMDS bonded with the surface of the wafer, even if it is partially hydroxylated. The other side of the HMDS layer bonds readily with the resist.

    ii. After HMDS application the wafer undergo a soft-bake at 150°Cfor 30 seconds. Soft-bake is required to promote HMDS adhesion.

    iii. Then positive resist (PR) AZ4330 is spun on the wafer with rotational speed of 4000 rpm for 30 seconds. At 4000rpm, as per the MSDS, a PR thickness ~3.3μm is formed on the wafer after spinning.

    iv. The photoresist was dried out at 90°Cfor 90 seconds (hard bake).

    v. Now the single detector mesa etch definition mask is loaded on to the MJB- 3 mask aligner. Then wafer is exposed for 6 seconds at 200 mJ/cm^2 on the mask aligner to transfer the mask pattern onto the PR deposited surface of the wafer.

vi. The wafer is then developed in AZ400K developer diluted with four parts of water for 60-90 sec. Then the wafer is rinsed in DI water bath for two minutes and blow-dried with N_2.

vii. Finally, patterns are examined under Nomarski microscope and measured by an Alfa-step profilometer. The resulting PR thickness is typically equal to 3.2 μm.

(c) **Mesa definition Etch:** Various etching methods such as a wet chemical etch or Plasma based dry etch may be utilized for the SLS mesa definition. The experiments on these are carried out in Chapter 4 of the dissertation.

i. For example, wet chemical etching based on phosphoric acid (eqn. A.1) with etch rate equal to 0.08 μm/min may be utilized.

$$H_3PO_4 : H_2O_2 : H_2O = 1 : 2 : 20 \tag{A.1}$$

ii. Plasma assisted etch with combination of BCl_3, CH_4, and Ar gases provides nearly vertical profiles and clean sidewalls of InAs/GaSb SLS detector free from etch residues. Hence in all of our devices fabricated and utilized in Chapters 5 and 7 we used the PlasmaTherm SLR 770 ICP Cl2 Etcher with BCl_3 gas. The etch rate in this recipe was about 0.2-0.3μm/min of InAs/GaSb based structures.

2. **Passivation Techniques**

Passivation coating is usually applied on pre-cleaned and post-mesa etched surface. The passivation techniques applied on the InAs/GaSb based SLS detectors are different and are discussed in detail in Chapters 3 and 5 of this thesis.

(a) **Passivation Deposition Step:** The passivation techniques of SiO_2, SiN_x,

ZrO_2, ZnTe:Cl and ZnS, passivation deposition are performed before the contact metal is deposited. The following steps are for SiO_2, SiN_x, ZrO_2, ZnTe:Cl and ZnS passivation techniques.

i. **Post-Mesa Etch/ Pre-Passivation Deposition Treatment:** After the wafer is etched it surface may contain residues.
   A. Hence the wafer is first cleaned in acetone, IPA and DI water (5 minutes each) and then blow-dried with N_2.
   B. Then dehydration bake is performed at 150°Cfor 7-10 minutes.
ii. **Pre-Passivation Deposition Treatment:** In order to remove native oxides that are formed on the device surface, we treat the PR patterned post-mesa etched surface in either of the following treatments:
   A. Phosphoric Acid Technique: In this technique, the wafer is dipped in H_3PO_4: H_2O_2: H_2O (1:2:20) solution for 10-20sec.
   B. Hydrochloric Acid Technique: In this technique, the wafer is dipped in HCl: H_2O (1:10) solution for 10-20sec.

   It has to be noted that the time duration between mesa etch, pre-passivation treatment and loading it into passivation deposition apparatus must be kept as minimal as possible. In our fabrication procedure this time was no more that 60min for SiO_2, SiN_x, and ZnS passivation techniques. But for ZrO_2, and ZnTe:Cl passivation techniques the wafer had to be sent out.
iii. **Passivation Deposition:** SiO_2, SiN_x, ZrO_2, ZnTe:Cl and ZnS passivation techniques were all carried out in vacuum systems and hence ensure good quality deposition with uniformity and exact thickness of the passivation layer. Further details of deposition are provided in chapters 3, 5 and 7.

(b) **Passivation Removal Step:** It has to emphasized that in SiO_2, SiN_x, ZrO_2, ZnTe:Cl and ZnS passivation techniques of thicknesses 2000Å, the passivation layer is removed from area of the aperture, top and bottom metal contact regions.

  i. **Post-Mesa Etch/ Pre-Passivation Deposition Treatment:** After the wafer is etched it surface may contain residues.

    A. Hence the wafer is first cleaned in acetone, IPA and DI water (5 minutes each) and then blow-dried with N_2.

    B. Then dehydration bake is performed at 150°Cfor 7-10 minutes.

  ii. **Application of Photoresist:** For passivation removal step we utilized light sensitive photoresist to lay down the pattern for the passivation layer etch which defines the size of the detector.

    A. Immediately following the bake, the wafer is primed with hexamethyldisilazane (HMDS), and for spinning on the HMDS, the wafer is mounted on a vacuum chuck. Torque is applied to the chuck to rapidly accelerate in with rotational speed of 5000 rpm for 30 seconds.

    B. After HMDS application the wafer undergo a soft-bake at 150°Cfor 30 seconds. Soft-bake is required to promote HMDS adhesion.

    C. Then positive resist (PR) AZ4330 is spun on the wafer with rotational speed of 4000 rpm for 30 seconds.

    D. The photoresist was dried out at 90°Cfor 90 seconds (hard bake).

    E. Now the single detector passivation removal/Top and Bottom metal contact mask is loaded on to the MJB- 3 mask aligner. Then wafer is exposed for 6 seconds at 200 mJ/cm^2 on the mask aligner to transfer the mask pattern onto the PR deposited surface of the wafer.

F. The wafer is then developed in AZ400K developer diluted with four parts of water for 60-90 sec. Then the wafer is rinsed in DI water bath for two minutes and blow-dried with N_2.

G. Finally, patterns are examined under Nomarski microscope and measured by an Alfa-step profilometer. The resulting PR thickness is typically equal to 3.2 μm.

iii. **Passivation Removal Etch:** Each of the SiO_2, SiN_x, ZrO_2, ZnTe:Cl and ZnS passivation techniques are etched differently. These techniques are explained in Chapter 3, 5 and 7. In the end of the passivation removal process, all passivation is removed from aperture and metal contact regions, but passivation remains intact on the device sidewalls and all other regions.

3. **Top and bottom contact metallization**

   (a) **Post Mesa Etch/ Post-Passivation Treatment:** After the wafer is etched and/or passivated, its surface may contain residues.

      i. Hence the wafer is first cleaned in acetone, IPA and DI water (5 minutes each) and then blow-dried with N_2.

      ii. Then dehydration bake is performed at 150 °Cfor 7-10 minutes.

   (b) **Application of Photoresist:**

      i. After the wafer has been through the surface preparation treatment, it is primed with HMDS with rotational speed of 5000 rpm for 30 seconds.

      ii. Following the spinning on of HMDS, a soft bake at 150 °C
      for 30 seconds is performed.

      iii. The wafer is coated with AZ5214E-IR photoresist after it is primed. Photoresist is spun on the wafer with a rotational speed of 5000rpm for 30 seconds. These conditions verified negative wall profiles needed for the lift-off of evaporated metal.

    iv. After resist application, the wafer is baked at 90°Cfor 90 seconds. The function of this step is to eliminate most of the solvent in the resist and to establish the exposure characteristics.
    v. After bake, the wafer is exposed for 3.5 seconds at 200 mJ/cm^2 on MJB-3 mask aligner. It must be noted that for this step, the single detector top and bottom contact metal mask is loaded on to the MJB-3 mask aligner.
    vi. For the image reversal of the photoresist, the most critical parameter is reversal-bake temperature (it should not exceed 125°C). The exposed wafer is baked for duration of one minute at 112°C.
    vii. Then flood exposure (without mask) for one minute at the same light intensity is applied earlier to the wafer.
    viii. Finally, wafer is developed in AZ400K developer diluted in five parts of water for ~30 sec. Then the wafer is rinsed in DI water bath for two minutes and blow-dried with N_2.
    ix. Patterns are examined under Nomarski microscope and measured by alfa-step profilometer. The resulting thickness of the resist is typically equal to 1.3 μm.

(c) **Pre-Contact Metal Deposition Treatment:** In order to remove native oxides that are formed on the device surface, we treat the PR patterned post-mesa etched surface in any of the following treatments:

    i. Phosphoric Acid Technique: In this technique, the wafer is dipped in H_3PO_4: H_2O_2: H_2O (1:2:20) solution for 10-20sec.
    ii. Hydrochloric Acid Technique: In this technique, the wafer is dipped in HCl: H_2O (1:10) solution for 10-20sec.

    iii. Oxygen Plasma treatment: Here the wafer is placed in O_2 Asher set-up, were ionized O_2 bombards the surface of the wafer to remove remnants of PR left behind.

    It has to be noted that none of these treatments are carried out for long periods of time as they might etch away at the InAs/GaSb SLS material itself.

  (d) **Deposition of Contact Metal:** After the completion of the photolithography process, metals are deposited. For both p and n-type contacts, 50 nm Ti/ 50 nm Pt/ 350 nm Au is used. This composition provided good ohmic behavior of contacts for the n-type GaSb and p-type SLS contacts without annealing. Metals are thermally evaporated in e-beam thermal evaporator. Finally, lift-off process is performed by soaking of the samples in acetone for 2 hours with subsequent acetone-brush treatment. Resulting thickness of metal patterns is verified by an alfa-step profilometer.

4. **Other Passivation Techniques:**

  (a) $(NH_4)_2S$, TAM and ECP Passivation techniques are all applied after the top and bottom contact metal deposition and are not removed from the aperture and contact metal regions.

  (b) SU-8 is applied after the top and bottom contact metal deposition and it is removed from the aperture and contact metal regions. SU-8 is a photoresist that polymerizes under UV light exposure. SU-8 passivation procedure is as follows:

    i. The post top and bottom contact metal deposition surface is cleaned by first cleaning in acetone, IPA and DI water (5 minutes each) and then blow-dried with N_2.

    ii. Then dehydration bake is performed at 150°Cfor 7-10 minutes

iii. An oxide removal step is performed by dipping the sample in H_3PO_4: H_2O_2: H_2O (1:2:20) solution for 20-40 sec.

iv. After the wafer has been through the surface preparation treatment, it is primed with HMDS with rotational speed of 5000 rpm for 30 seconds.

v. Following the spinning on of HMDS, a soft bake at 150°Cfor 30 seconds is performed.

vi. The wafer is coated with SU-8 photoresist after it is primed. SU-8 is spun on the wafer with a rotational speed of 3000rpm for 30 seconds.

vii. After resist application, the wafer is soft-baked in two subsequent steps: (1) 65°Cfor 1minute and (2) 95°Cfor 2 minutes. The function of this step is to eliminate most of the solvent in the resist and to establish the exposure characteristics.

viii. After bake, the wafer is exposed for 3.6 seconds at 200 mJ/cm^2 on MJB-3 mask aligner. It must be noted that for this step, the single detector passivation mask is loaded on to the MJB- 3 mask aligner.

ix. After the passivation pattern exposure, once again two subsequent soft-bake steps are carried out: (1) 65°Cfor 1minute and (2) 95°Cfor 2 minutes.

x. The wafer is developed in SU-8 developer for ~80sec. Then the wafer is rinsed in DI water bath for two minutes and blow-dried with N_2.

xi. Finally, the wafer is subjected to a hard-bake at 150°Cfor 5 minutes. Photo-polymerized SU-8 is mechanically and chemically stable after a hard bake.

xii. Patterns are examined under Nomarski microscope and measured by alfa-step profilometer. The resulting thickness of the resist is typically equal to 1.5 μm.

5. **Passivation Contact Metal** This fabrication step was utilized during the making of the detector with 3-T device architecture only and the device results are discussed in Chapter 7.

    (a) **Post-Passivation Treatment:** After the wafer passivated with SiO_2 or ZrO_2, and contact metal is deposited, the detector surface may contain transference residues.

        i. Hence the wafer is first cleaned in acetone, IPA and DI water (5 minutes each) and then blow-dried with N_2.
        ii. Then dehydration bake is performed at 150°Cfor 7-10 minutes.

    (b) **Application of Photoresist:** For our passivation contact metal deposition step we once again utilize image reversible photoresist to lay down the pattern.

        i. After the wafer has been through the surface preparation treatment, it is primed with HMDS with rotational speed of 5000 rpm for 30 seconds.
        ii. Following the spinning on of HMDS, a soft bake at 150°Cfor 30 seconds is performed.
        iii. The wafer is coated with AZ5214E-IR photoresist after it is primed. Photoresist is spun on the wafer with a rotational speed of 5000rpm for 30 seconds. These conditions verified negative wall profiles needed for the lift-off of evaporated metal.
        iv. After resist application, the wafer is baked at 90°Cfor 90 seconds. The function of this step is to eliminate most of the solvent in the resist and to establish the exposure characteristics.

v. After bake, the wafer is exposed for 3.5 seconds at 200 mJ/cm^2 on MJB-3 mask aligner. It must be noted that for this step, the single detector contact metal mask is loaded on to the MJB-3 mask aligner.

vi. For the image reversal of the photoresist, the most critical parameter is reversal-bake temperature (it should not exceed 125°C). The exposed wafer is baked for duration of one minute at 112°C.

vii. Then flood exposure (without mask) for one minute at the same light intensity is applied earlier to the wafer.

viii. Finally, wafer is developed in AZ400K developer diluted in five parts of water for ~30 sec. Then the wafer is rinsed in DI water bath for two minutes and blow-dried with N_2.

ix. Patterns are examined under Nomarski microscope and measured by alfa-step profilometer. The resulting thickness of the resist is typically equal to 1.3 μm.

(c) **Pre-Contact Metal Deposition Treatment:** It has to be noted here that no pre-contact metal deposition treatment is carried out here as these wet chemical etches could potentially etch away the passivation layer.

(d) **Deposition of Contact Metal:** After the completion of the photolithography process, contact metals are deposited on the SiO_2 or ZrO_2 passivation layer. For both passivation techniques we deposited, 50 nm of Ti/ 300 nm Au. This composition provided good ohmic behavior of contacts for the dielectric passivation layers without annealing. These metals are thermally evaporated in e-beam thermal evaporator. Finally, lift-off process is performed by soaking of the samples in acetone for 2 hours with subsequent acetone-brush treatment. Resulting thickness of metal patterns is verified by an alfa-step profilometer and microscopic measurements.

Appendix B

Typical Fabrication Procedure of SLS-based FPA

The processing sequence we utilize for fabrication of an InAs/GaSb SLS FPA with the pin or pBiBn designs can be summarized as follows:

1. Mesa Etch definition, Passivation process and the top and bottom contact metal deposition:

    (a) Etch is commonly performed with inductively coupled plasma using BCl_3 gas. The etch procedure, including cleaning and photoresist deposition, is identical to the etch of single-pixel detectors described in Appendix A.

    (b) The passivation deposition and removal process depends on the chosen technique. In FPA fabrication this step is carried out after mesa etch definition and before contact metal deposition. Typically implemented passivation technique for FPA fabrication are SiO_2, SiN_x and SU-8. E-beam deposited ZnS, ZnTe:Cl and ZrO_2 can seamlessly be incorporated into FPA fabrication.

(c) The top and bottom metal contact deposition process is as described in Appendix A.

2. Under bump metallization (UBM)

   The Under Bump Metal (UBM) is the first step to connect the semiconductor device to the read-out integrated circuit (ROIC). Therefore, the UBM layer serves as (i) a seed layer for subsequent indium bump deposition, (ii) the adhesion layer in order to achieve low contact resistance, and (iii) the diffusion barrier for the bump material. Typically we use Ti (50nm) / Ni (150 nm)/Au (50 nm) as an under bump metal.

3. Bump (indium) depositions

   Indium is known as a material with good plasticity and high thermal conductivity. Moreover, molten indium (with a melting point of 156°C) has superior adhesion to a variety of surfaces at low temperatures, leading to compliant soldering processing. In addition, low temperature solidification of indium can reduce the thermal stress caused by lattice mismatch between SLS FPAs and ROICs. These properties make indium the best candidate for the bump metal.

4. Reflow process

   The purpose of the re-flow process is to change the shape of the In-pads deposited on the UBM layer into a spherical shape, using indium flux, which makes FPA-ROIC bonding easier. Wafers with the deposited In pads are heated to 200°Cfor a few minutes to form balls. The ball formation is held due to surface tension in the liquid-phase. The total volume of the ball depends on the wettable UBM layer size and the volume of the indium deposited by thermal evaporation.

5. Hybridization with Read-Out Integrated Circuit (ROIC)

   The direct electrical connection of an FPA with a ROIC is known as flip-chip bonding. This technique enables the smallest packaging with the high speed performance of the FPA, by eliminating the need for wire bonding while achieving great flexibility of input / output connections with very robust interconnections from adhesive underfill processing. Flip-chip bonding of an SLS detector grown and fabricated on a GaSb substrate with a Si based ROIC is presently performed with a FC-150 flip-chip bonder. After mounting the SLS FPA chip on the upper arm and the ROIC on the lower chuck stage of the flip-chip bonder, an optical stage with a bi-directional optical microscope is positioned between the SLS FPA and the ROIC for visual alignment. The image of both chips can be seen with a microscope or displayed on a monitor. After the horizontal, vertical, and rotational alignment and parallelism adjustment, the optical stage is retreated. Then the upper chip and lower chip are pressed together with a predefined pressure and temperature.

   During the bonding cycle, the temperature and pressure were set to 200°Cand 200 Newtons (N), respectively, to melt the indium and bond the two chips. The performance of the FPA can be greatly degraded (possible electrical disconnection) if the two bonded chips have mismatched parallelism. Therefore, approximately 10μm thick indium bumps should be fabricated during the indium deposition process to compensate for possible variations in parallelism between the FPA and ROIC.

   The space not filled with Indium between the ROIC and FPA should be filled with a nonconductive adhesive material to increase chip strength and long term reliability. The underfill epoxy can protect the indium bumps from humidity, vibration and chemical contamination providing additional mechanical bonding strength for the hybrid FPA.

6. Substrate removal

   After hybridization with indium bumps and underfill epoxy, substrate removal is a standard processing step performed with abrasive polishing, dry etching, or wet chemical etching. Substrate removal is beneficial for operation of hybridized FPA chips firstly, because it reduces thermal stress developed between the FPA and ROIC from multiple thermocycles due to cooling. Secondly, completely removing the substrate eliminates optical cross talk between neighboring pixels of the FPA. Finally, GaSb substrates absorb nearly 50% of infrared light at 77 K, causing up to 50% reduction in quantum efficiency for the FPA. Therefore, substrate removal enables SLS FPA devices to have enhanced optical quantum efficiency by reducing substrate absorption during operation with back side illumination.

   Presently, we use mechanical polishing with different lapping film grades for substrate removal. The backside of samples is finished to mirror-like conditions by using lapping films with a 0.3 μm grade.

References

[1] http://www.microchem.com/products/su_eight.htm.

[2] Nist x-ray photoelectron spectroscopy database, version 3.5. http://srdata.nist.gov/xps/ (2003).

[3] US Patent No 4882245, 1989.

[4] A. Rogalski. Third-generation infrared photon detectors. *Opt. Eng.*, 42(12):3498–3516, 2003.

[5] A. Agirregabiria, F. J. Blanco, J. Berganzo, M. T. Arroyo, A. Fullaondo, K. Mayora, and J. M. Ruano-Lopez. Fabrication of SU-8 multilayer microstructures based on successive CMOS compatible adhesive bonding and releasing steps. *Lab on a Chip*, 5:545–552, 2005.

[6] E. H. Aifer, J. H. Warner, C. L. Canedy, I. Vurgaftman, E. M. Jackson, J. G. Tischler, J. R. Meyer, S. P. Powell, K. Olver, and W. E. Tennant. Shallow-etch mesa isolation of graded bandgap structured type-ii superlattice photodiode. *J. Electron. Mater.*, 39:1070–1079, 2010.

[7] E. H. Aifer, J. G. Tischler, J. H. Warner, I. Vurgaftman, W. W. Bewley, J. R. Meyer, J. C. Kim, L. J. Whitman, C. L. Canedy, and E. M. Jackson, W-structured type-II superlattice long-wave infrared photodiodes with high quantum efficiency *Appl. Phys. Lett.*, 89, 053519, 2006.

[8] K. Banerjee, S. Ghosh, S. Mallick, E. Plis, and S. Krishna. Electrical characterization of different passivation treatments for long-wave infrared InAs/GaSb strained layer superlattice photodiodes. *J. Electron. Mater.*, 38:1944–1947, 2009.

[9] K. Banerjee, S. Ghosh, E. Plis, and S. Krishna. Study of short- and long-term effectiveness of ammonium sulfide as surface passivation for InAs/GaSb superlattices using x-ray photoelectron spectroscopy. *J. Electron. Mater.*, 39:2210–2214, 2010.

[10] K. Banerjee, J. Huang, S. Ghosh, R. Xu, C. G. Takoudis, E. Plis, S. Krishna, S. Ketharanathan, and M. Chriss. Surface study of thioacetamide and zinc sulfide passivation long wavelength infrared type ii strained layer superlattice. *Proc. of SPIE*, 8012:801243–801251, 2011.

[11] S. Basu and P. Barman. Chemical modification and characterization of Te-doped n-GaSb (111) single crystals for device application. *J. Vac. Sci. Technol. B*, 10(3):1078–1080, 1992.

[12] V. N. Bessolov and M. V. Lebedev. Chalcogenide passivation of III-V semiconductor surfaces. *Semiconductors*, 32:1141–1156, 1998.

[13] R Bhargava (ed) Properties of Wide bandgap II-VI Semiconductors *Inspec. London*,1997.

[14] V. N. Bessolov, M. V. Lebedev, E. B. Novikov, and B. V. Tsarenkov. Sulfide passivation of III-V semiconductors: Kinetics of the photoelectrochemical reaction. *J. Vac. Sci.Technol. B*, 11:10–14, 1993.

[15] V. N. Bessolov, Y. V. Zhilyaev, E. V. Konenkova, and M. V. Lebedev. Sulfide passivation of III-V semiconductor surfaces: role of the sulfur ionic charge and of the reaction potential of the solution. *J. Tech. Phys.*, 43:983–985, 1998.

[16] V.N. Bessolov, E.V. Konenkova, and M.V. Lebedev. Sulfidization of GaAs in alcoholic solutions: a method having an impact on efficiency and stability of passivation. *Mater. Sci. Eng. B*, 44:376–379, 1997.

[17] Bhattacharya, , Singapore, 1997. Semiconductor Optoelectronic Devices. 2nd edition, chapter 8, page 346, Pearson Education, Inc.

[18] G. J. Brown. Type-ii inas/gainsb superlattices for infrared detection: an overview. *Proc. of SPIE*, 5783:65–77, 2005.

[19] C. Cervera, I. Ribet-Mohamed, R. Taalat, J. P. Perez, P. Christol, and J. B. Rodriguez. Dark current and noise measurements of an InAs/GaSb superlattice photodiode operating in the midwave infrared domain. *J. Electron. Mater.*, 41:2714–2718, 2012.

[20] C. Cervera, J. B. Rodriguez, R. Chaghi, H. Ait-Kaci, and P. Christol. Characterization of midwave infrared inas/gasb superlattice photodiode. *J. Appl. Phys.*, 160:024501–024505, 2009.

[21] R. Chaghi, C. Cervera, H. Ait-Kaci, P. Grech, J. B. Rodriguez, and P. Christol. Wet etching and chemical polishing of inas/gasb superlattice photodiodes. *Semicond. Sci. Technol.*, 24:065010–065015, 2009.

[22] G. Chen, B.-M. Nguyen, A. M. Hoang, E. K. Huang, S. R. Darvish, and M. Razeghi. Elimination of surface leakage in gate controlled type-II InAs/GaSb mid-infrared photodetectors. *Appl. Phys. Lett.*, 99:183503–1–183503–3, 2011.

[23] Y. Chen, A. Moy, S. Xin, K. Mi, and P. P. Chow. Improvement of r0a product of type-ii inas/gasb superlattice mwir/lwir photodiodes. *Inf. Phys. Technol.*, 52:340–343, 2009.

[24] G. Chen, B.-M. Nguyen, A. M. Hoang, E. K. Huang, S. R. Darvish, and M. Razeghi. Suppression of surface leakage in gate controlled type-II InAs/GaSb mid-infrared photodetectors. *Proc of SPIE.*,Vol.8268, 826811, 1-7, 2012.

[25] P. Y. Delaunay, A. Hood, B. M. Nguyen, D. Hoffman, Y. Wei, and M. Razeghi. Passivation of type-ii inas/gasb double heterostructure. *Appl. Phys. Lett.*, 91:091112, 2007.

[26] P. Y. Delaunay, B. M. Nguyen, D. Hoffman, A. Hood, E. K. Huang, M. Razeghi, and M. Z. Tidrow. High quantum efficiency two color type-II InAs/GaSb n-i-p-p-i-n photodiodes. *Appl. Phys. Lett.*, 92:111112–111114, 2008.

[27] P. Y. Delaunay and M. Razeghi. Spatial noise and correctability of type-II InAs/GaSb focal plane arrays. *IEEE J Quant Electron*, 46:584–588, 2010.

[28] E.L. Dereniak, and G.D. Boreman. Infrared Detector Systems. chapter 3, page 87, John Wiley and Sons, Inc., New York, 1996.

[29] S. dip Das, S. L. Tan, S. Zhang, Y. L. Goh, C. H. Ting, and J. David. Development of LWIR photodiodes based on InAs/GaSb type-II strained layer superlattices. page B7. 6th EMRS DTC Technical conference- Edinburgh, 2009.

[30] D.L. Smith and C. Mailhiot. Proposal for strained type II superlattice infrared detectors. *J. Appl. Phys.*, 62:2545–2548, 1987.

[31] P. S. Dutta, H. L. Bhat, and V. Kumar. The physics and technology of gallium antimonide: An emerging optoelectronic material. *Journal of Applied Physics*, 81, 1997.

[32] P. S. Dutta, K. S. Sangunni, H. L. Bhat, and V. Kumar. Sulphur passivation of gallium antimonide surfaces. *Appl. Phys. Lett.*, 65:1695–1697, 1994.

[33] Jr E. A. DeCuir, J. W. Little, and N. Baril. Addressing surface leakage in type-ii inas/gasb superlattice materials using novel approaches to surface passivation. *Proc. of SPIE*, 8155:815508–1–815508–8, 2011.

[34] L. Esaki. InAs-GaSb superlattices-synthesized semiconductors and semimetals. *J. Cryst. Growth*, 52:227–240, 1981.

[35] J. W. Jr. Faust. *Compound Semiconductors, Preparation of III-V Compounds*, volume 1, chapter 50, page 445. Reinhold, Chapman and Hall, London, 1962.

[36] J. W. Jr. Faust and A. Sagar. Effect of the Polarity of the III-V Intermetallic Compounds on Etching. *Journal of Applied Physics*, 31:331, 1960.

[37] F.Fuchs, U. Weimar, E. Ahlswede, W. Pletschen, J. Schmitz, and M. Waither. InAs/Ga1-xInxSb infrared superlattice photodiodes for infrared detection. *Proc. SPIE* , Vol.3287,14, 1998.

[38] H.C. Gatos, M.C. Lavine, and E.P. Warekois. *J. Electrochem. Soc.*, 108, 645, 1961.

[39] N. Gautam, H. S. Kim, M. N. Kutty, E. Plis, L. R. Dawson, and S. Krishna. Performance improvement of longwave infrared photodetector based on type-II InAs/GaSb superlattices using unipolar current blocking layers. *Appl. Phys. Lett.*, 96:231107–231109, 2010.

[40] A. Gin, Y. Wei, J. Bae, A. Hood, J. Nah, and M. Razeghi. Passivation of type II InAs/GaSb superlattice photodiodes. *Thin Solid Films*, 447-448:489–492, 2004.

[41] A. Gin, Y. Wei, A. Hood, A. Bajowala, V. Yazdanpanah, M. Razeghi, and M. Tidrow. Ammonium sulfide passivation of type-II InAs/GaSb superlattice photodiodes. *Appl. Phys. Lett.*, 84:2037–2039, 2004.

[42] V. Gopal. A general relation between zero-bias resistance - area product and perimeter-to-area ratio of the diodes in variable-area diode test structures. *Semicond. Sci. Technol*, 11:1070–1076, 1994.

[43] C. H. Grein, M. E. Flatte, H. Ehrenreich, and R. H. Miles. Comment on "Temperature limits on infrared detectivities of InAs/InGaSb superlattices and bulk HgCdTe" [J. Appl. Phys. 74, 4774 (1993)]. *J. Appl. Phys.*, 77:4153–4155, 1995.

[44] C.H. Grein, H. Cruz, M.E. Flatte, and H. Ehrenreich. Theoretical performance of very long wavelength InAs/InGaSb superlattice based infrared detectors. *Appl. Phys. Lett.*, 65:2530–2532, 1994.

[45] S. D. Gunapala, D. Z. Ting, C. J. Hill, J. Nguyen, A. Soibel, S. B. Rafol, S. A. Keo, J. M. Mumolo, M. C. Lee, J. K. Liu, and B. Yang. Demonstration of a 1024 x 1024 pixel InAs–GaSb superlattice focal plane array. *IEEE Photon. Tech. Lett.*, 22:1856–1858, 2010.

[46] A. Haddadi, S. R. Darvish, G. Chen, A. M. Hoang, B. M. Nguyen, and M. Razeghi. High operability 1024 x 1024 long wavelength type-II superlattice focal plane array. *IEEE J. Quant. Electron.*, 48:221–228, 2012.

[47] C. Heinz. *International Journal of Electronics*, 75:285, 1993.

[48] M.A. Herman, and H. Sitter. Molecular Beam Epitaxy-Fundamentals and Current Status. Springer-Verlag (Berlin and New York), Volume 7, chapter 5, pg.206-207, 1989.

[49] G. Hollinger, R. Skheyta-Kabbani, and M. Gendry. *Phys. Rev.B*, 49, 11159, 1994.

[50] A. Hood, P. Y. Delaunay, D. Hoffman, B. M. Nguyen, Y. Wei, and M. Razeghi. Near bulk-limited R0A of long-wavelength infrared type-II InAs/GaSb superlattice photodiodes with polyimide surface passivation. *Appl Phys. Lett.*, 90:233513–233515, 2007.

[51] A. Hood, M. Razeghi, E.H. Aifer, and G.J. Brown. On the performance and surface passivation of type II InAs/GaSb superlattice photodiodes for the very-long-wavelength infrared. *Appl. Phys. Lett.*, 87:151113–15116, 2005.

[52] E. K. Huang, B. M. Nguyen, D. Hoffman, P. Y. Delaunay, and M. Razeghi. nductively coupled plasma etching and processing techniques for type-ii InAs/GaSb superlattices infrared detectors toward high fill factor focal plane arrays. *Proc. of SPIE*, 7222:72220Z–72220Z–08, 2009.

[53] E. K. W. Huang, S. Hoffman, B. M. Nguyen, P. Y. Delaunay, and M. Razeghi. Surface leakage reduction in narrow band gap type-II antimonide based superlatice photodiodes. *Appl. Phys. Lett.*, 94:053506–053508, 2009.

[54] Richard. D. Hudson. Infrared System Engineering. Chapter 4, John Wiley & Sons; New York, 1969. 94:053506–053508, 2009.

[55] T.Ishizaki, T. Ohtomo and A. Fuwa. Structural, optical and electrical properties of Znte thin films electrochemically deposited from citric acid aqueous solutions. *J.Physics D: Appl. Phys.*,37 (2) 255, 2004.

[56] M.Jain (ed). II-VI Semiconductor Compounds *World Scientific, Singapore*,1993.

[57] H. S. Kim, E. Plis, N. Gautam, S. Myers, Y. Sharma, L. R. Dawson, and S. Krishna. Reduction of surface leakage current in InAs/GaSb strained layer long wavelength superlattice detectors using SU-8 passivation. *Appl Phys. Lett.*, 97:143512–142514, 2010.

[58] H. S. Kim, E. Plis, A. Khoshakhlagh, S. Myers, N. Gautam, Y. D. Sharma, L. R. Dawson, S. Krishna, S. J. Lee, and S. K. Noh. Performance improvement of InAs/GaSb strained layer superlatticedetectors by reducing surface leakage currents with SU-8 passivation. *Appl. Phys. Lett.*, 96:033502–033504, 2010.

[59] Y. T. Kim, D. S. Kim, and D. H. Yoon. PECVD SiO_2 and SiON films dependant on the rf bias power for low-loss silica waveguide. *Thin Solid Films*, 475:271–274, 2005.

[60] M. Kinch. *J. Electron. Mater.*, 29:809–817, 2000.

[61] J. W. Lee, W. T. Lim, I. K. Baek, S. R. Yoo, M. H. Jeon, G. S. Cho, and S. J. Peatron. Etching of As- and P-based III–V semiconductors in a planar inductively coupled BCl3/Ar plasma. *J. Electron. Mater.*, 33:358–361, 2004.

[62] S. H. Lee, S. H. Bae, H. C. Lee, and C. K. Kim. urface treatment effects on the electrical properties of the interfaces between zns and lpe-grown hg0.7cd0.3te. *J. Electron. Mater.*, 27:684–688, 1998.

[63] Z. Lu, Y. Jiang, W.I. Wang, M.C. Teich, and R.M. Osgood Jr. *J. Vac. Sci. Technol.* B10, p.1856, 1992.

[64] Z. Y. Liu, A. A. Gokhale, M. Mavrikakis, D. A. Saulys, and T. F. Kuech. Modification of the electronic structure of GaSb surface by chalcogen atoms: S, Se and Te. *J. Appl. Phys.*, 96:4302–4307, 2004.

[65] Z. Y. Liu, B. Hawkins, and T. F. Kuech. Chemical and structural characterization of GaSb (100) surfaces treated by HCl-based solutions and annealed in vacuum. *J. Vac. Sci. Technol. B*, 21:71–77, 2003.

[66] M. Madou. *Fundamentals of Microfabrication*, page 1. CRC PRess LLC, 1997.

[67] S. Mallick, K. Banerjee, S. Ghosh, E. Plis, J. B. Rodriguez, S. Krishna, and C. Grein. Ultralow noise midwave infrared InAs–GaSb strain layer superlattice avalanche photodiode. *Appl. Phys. Lett.*, 91:241111–241113, 2007.

[68] S. Mallick, K. Banerjee, S. Ghosh, J. B. Rodriguez, and S. Krishna. Mid-wavelength infrared avalanche photodiode using InAs–GaSb strain layer superlattice. *IEEE Photon. Tech. Lett.*, 19:1843–1845, 2007.

[69] J.R. Meyer, C.A. Hoffman, F.J. Bartoli, and L.R. Ram-Mohan. Type-II quantum-well lasers for the mid-wavelength infrared Appl. Phys. Lett. 67, 757, 1995.

[70] M.N.Kutty, E.Plis, A. Khoshakhlagh, S. Myers, N. Gautam, S. Smolev, Y.D. Sharma, R. Dawson, S. Krishna, S.J.Lee, S.K.Noh Study of Surface treatments on InAs/GaSb superlattice LWIR detectors *J. Electron. Mater.*, Vol. 39, No. 10, pp.2203-2209 (2010).

[71] R. H. Miles, D. H. Chow, J. N. Schulman, and T. C. McGill. Infrared optical characterization of $InAs/Ga\_1 - xIn\_xSb$ superlattices. *Appl. Phys. Lett.*, 57:801–803, 1990.

[72] G. Nagy, R. U. Ahmad, M. Levy, R. M. Osgood, M. J. Manfra, and G. W. Turner. Chemically assisted ion beam etching of submicron features in GaSb. *Appl Phys. Lett.*, 72:233106–233109, 1998.

[73] B. M. Nguyen, D. Hoffman, E. K. Huang, P. Y. Delaunay, and M. Razeghi. Background limited long wavelength infrared type-II InAs/GaSb superlattice photodiodes operating at 110 K. *Appl. Phys. Lett.*, 93:123502–123504, 2006.

[74] B. M. Nguyen, D. Hoffman, P. Y. Delaunay, and M. Razeghi. Dark current suppression in type II InAs/GaSb superlattice long wavelength infrared photodiodes with M-structure barrier. *Appl. Phys. Lett.*, 91, 163511, 2007.

[75] B.-M. Nguyen, D. Hoffman, E. K. Huang, P. Y. Delaunay, and M. Razeghi. *Appl. Phys. Lett.*, 93:123502–123504, 2008.

[76] J. Nguyen, A. Soibel, D. Z. Y. Ting, C. J. Hill, M. C. Lee, and S. D. Gunapala. Low dark current long-wave infrared InAs/GaSb superlattice detectors. *Appl Phys. Lett.*, 97:051108–051110, 2009.

[77] J. A. Nolde, R. Stine, E. M. Jackson, C. L. Canedy, I. Vurgaftman, S. I. Maximenko, C. A. Affouda, M. Gonzalez, E. H. Aifer, and J. R. Meyer. Effect of the oxide-semiconductor interface on the passivation of hybrid type-ii superlattice long-wave infrared photodiodes. *Proc. of SPIE*, 7945:79451Y–1–79451Y–9, 2011.

[78] T. Ohno. Passivation of GaAs(001) surfaces by chalcogen atoms (S, Se and Te). *Surf. Sci.*, 225:229–236, 1991.

[79] T. Ohno and K. Shiraishi. First-principles study of sulfur passivation of GaAs (001) surfaces. *Phys. Rev. B*, 42:11194–11197, 1990.

[80] H. Oigawa, J.F. Fan, Y. Nannichi, H. Sugahara, and M. Osofhima. Universal passivation effect of $(NH\_4)\_2S\_x$ treatment on the surface of III-V compound semiconductors. *Jap. J. Appl. Phys.*, 30:L322–1–L322–5, 1991.

[81] A.P. Ongstad, R. Kaspi, C.E. Moeller, M.L. Tilton, D.M. Gianardi, J.R. Chavez, and G.C. Dente. Spectral blueshift and improved luminescent properties with increasing GaSb layer thickness in InAs-GaSb type-II superlattices. *J. Appl. Phys.*, 89:2185–2187, 2001.

[82] D. Paget, A. O. Gusev, and V. L. Berkovits. Sulfide-passivated GaAs (001). II. Electronic properties. *Phys. Rev. B*, 53:4615–4622, 1996.

[83] E. Papis-Polakowska Surface treatments of GaSb and related materials for the processing of mid-infrared semiconductor devices. *Electron Technol. Internet J.* ,37/38 (4), pgs 1-34, 2005/2006.

[84] M. Perotin, P. Coudray, L. Gouskov, H. Luquet, C. Linares, J.J. Bonnet, L. Soonckindt, and B. Lambert. Passivation of GaSb by sulfur treatment. *J. Electron. Mater.*, 23:7–12, 1994.

[85] D.Y. Petrovykh, M.J. Yang, and L.J. Whitman. Chemical and electronic properties of sulfur-passivated InAs surfaces. *Surf. Sci.*, 523:231–240, 2003.

[86] A.Y. Polyakov, M. Stan, A.G. Milnes and T.E. Schlesinger. *Mater. Sci. and Eng.*, B12, p.337, 1992.

[87] E. Plis, S. Annamalai, K.T. Posani, S. Krishna, R.A. Rupani, and S. Ghosh. Mid-wave infrared type-II InAs/GaSb superlattice detectors with mixed interfaces. *Journal of Applied Physics*, 100:014510, 2006.

[88] E.A. Plis , M.N. Kutty , S. Myers , A. Rathi , E.H. Aifer , I. Vurgaftman , S. Krishna Performance improvement of long-wave infrared InAs/GaSb strained-layer superlattice detectors through sulfur-based passivation *Inf. Phys. Technol.*, Volume 55, Issue 2, p. 216-219, 2012.

[89] E. Plis, M. N. Kutty, S. Myers, H. S. Kim, N. Gautam, L. R. Dawson, and S. Krishna. Passivation of long-wave infrared InAs/GaSb strained layer superlattice detectors. *Inf. Phys. Technol.*, 54:252–257, 2010.

[90] E. Plis, J. B. Rodriguez, H. S. Kim, G. Bishop, Y. D. Sharma, L. R. Dawson, S. Krishna, S. J. Lee, C. E. Jones, and V. Gopal. Type ii inas/gasb strain layer superlattice detectors with p-on-n polarity. *Appl Phys. Lett.*, 91:133512–133514, 2007.

[91] E. Plis, J. B. Rodriguez, S. J. Lee, and S. Krishna. Electrochemical sulphur passivation of InAs/GaSb strain layer superlattice detectors. *Electron. Lett.*, 42:1248–1249, 2006.

[92] Y. Qian, S. Kim, J. Song, and G. P. Nordin. Compact and low loss silicon-on-insulator rib waveguide 90 bend. *Opt. Express*, 14:6020–6028, 2006.

[93] K. Qui, A. C. S. Hayden, M. G. Mauk, and O. V. Sulima. Generation of electricity using InGaAsSb and GaSb TPV cells in combustion-driven radiant sources. *Sol. Energ. Mat.Sol. C*, 90:68, 2006.

[94] M. R. Ravi, A. DasGupta, and N. DasGupta. Silicon nitride and polyimide capping layers on InGaAs/InP PIN photodetector after sulfur treatment. *J. Cryst. Growth*, 268:359–363, 2004.

[95] R. Rehm, M. Walther, F. Fuchs, J. Schmitz, and J. Fleissner. Passivation of InAs/(GaIn)Sb short-period superlattice photodiodes with 10 μm cutoff wavelength by epitaxial overgrowth with Al_xGa_1xAs_ySb_1y. *Appl. Phys. Lett.*, 86:173501–171503, 2005.

[96] R. Rehm, M. Walther, J. Schmitz, J. Fleibner, F. Fuchs, J. Ziegler, and W. Cabanski. *Opt.-Electron. Rev.*, 14:19, 2006.

[97] Edited by J.C. Rivire, S. Myhra. Handbook of Surface and Interface Analysis-Methods for Problem Solving. *Marcel Dekker, Inc.*, New York, chapter 4, pages: 57-59 and 91-92, 1998.

[98] M. Schall, M. Walther, P. Uhd Jepsen. *Phys. Rev.*, B64, 94301, 2001.

[99] M. Schall, P. Uhd Jepsen. *Appl. Phys. Lett.*, 77, 2801, 2000.

[100] W. Shockley. Electrons and Holes in Semiconductors. van Nostrand, New York, p.381, 1950.

[101] G. P. Schwartz, G. J. Gualtieri, J. E. Griffiths, C. D. Thurmond, and B. Schwartz. Oxide-Substrate and Oxide-Oxide Chemical Reactions in Thermally Annealed Anodic Films on GaSb , GaAs , and GaP. /em J. Electrochem. Soc. 127, 2488, 1980.

[102] R.S.Title, G. Mande, and F.F. Morehead. *Phys. Rev.*, 136, 300, 1964.

[103] R. Rehm, M. Walther, J. Schmitz, J. Fleibner, S. Kopta, F. Fuchs, W. Cabanski, and J. Ziegler. Growth of InAs/GaSb short-period superlattices for high-resolution mid-wavelength infrared focal plane array detectors. *J. Cryst. Growth*, 278:150–161, 2005.

[104] W.Wang, A.Lin, and J.D. Phillips. Electrical Characteristics and Photoresponse of ZnO/ZnTe Heterojunction Diodes. *J. Electron. Mater*, 37, (8),1044-1048, 2008.

[105] W. Wang, A. Lin, J. D. Phillips, and W. Metzger. Generation and recombination rates at ZnTe:O intermediate band states. *Applied Physics Letters*, 95, page 261,107, 2009.

[106] Q.Wu, M. Litz, X.C.Zhang. Appl. Phys. Lett. 68 (21) 2924, 1996.

[107] D. R. Rhiger. Performance comparison of long-wavelength infrared type II superlattice devices with HgCdTe. *J. Electron. Mater.*, 40:1815–1822, 2011.

[108] J.B. Rodriquez, E. Plis, G. Bishop, Y.D. Sharma, H. Kim, L.R. Dawson, and S. Krishna. nBn structure based on InAs/GaSb type-II strained layer superlattices *Appl. Phys. Lett.*, 91, 043514, 2007.

[109] A. Rogalski. *New Ternary Alloy systems for Infrared Detectors*. SPIE, Bellingham, Washington, 1994.

[110] A. Rogalski. Infrared detectors: status and trends. *Prog. Quantum Electron.*, 27:59–210, 2003.

[111] G. A. Sai-Halasz, R. Tsu, and L. Esaki. A new semiconductor superlattice. *Appl. Phys. Lett.*, 30:651–653, 1977.

[112] A. Salesse, A. Joullie, P. Calas, J. Nieto, F. Chevrier, Y. Cuminal, G. Ferblantier, and P. Christol. Surface passivation of GaInAsSb photodiodes with thioacetamide. *Phys Stat Solidi (c)*, 4:1508–1512, 2007.

[113] C. J. Sandroff, M. S. Hegde, and C. C. Chang. Structure and stability of passivating arsenic sulfide phases on GaAs surfaces. *J. Vac. Sci. Technol. B*, 7:841–844, 1989.

[114] C. J. Sandroff, R.N. Nottenburg, C. J. Bischoff, and R. Bhat. *Appl. Phys. Lett.*, 51, p.33, 1987.

[115] G. P. Schwartz. Analysis of native oxide films and oxide-substrate reactions on III-V semiconductors using thermochemical phase diagrams. *Thin Solid Films*, 103:3–16, 1983.

[116] M. Shaw, D. Nawrocki, R. Hurditch, and D. Johnson. Improving the process capability of SU-8. *Microsyst. Technol.*, 10:1–6, 2003.

[117] C. J. Spindt, D. Liu, K. Miyano, P. L. Meissner, T. T. Chiang, T. Kendelewicz, I. Lindau, and W. E. Spicer. Vacuum ultraviolet photoelectron spectroscopy of (*NH*_4)_2)*S*-treated GaAs (100) surfaces. *Appl. Phys. Lett.*, 55:861–863, 1989.

[118] S. Sridaran, A. Chavan, and P. S. Dutta. Fabrication and passivation of GaSb photodiodes. *J. Cryst. Growth*,310, 15901594, 2008.

[119] J. Steinshnider, M. Weimer, R. Kaspi, and G. W. Turner. Visualizing Interfacial Structure at Non-Common-Atom Heterojunctions with Cross-Sectional Scanning Tunneling Microscopy. *Phys. Rev. Lett.*, 85:2953–2956, 2000.

[120] R. Stine, E. H. Aifer, L. J. Whitman, and D. Y. Petrovykh. Passivation of GaSb and InAs by pH-activated thioacetamide. *Appl. Surf. Sci.*, 255:7121–7125, 2009.

[121] M. Sundaram, A. Reisinger, R. Dennis, K. Patnaude, D. Burrows, J. Bundas, K. Beech, and R. Faska. Longwave infrared focal plane arrays from type-ii strained layer superlattices. *Inf. Phys. Technol.*, 54:243–246, 2011.

[122] F. Szmulowicz and G. J. Brown. Gasb for passivating type-ii inas/gasb superlattice mesas. *Inf. Phys. Technol.*, 53:305–307, 2011.

[123] D. Z. Y. Ting, C. J. Hill, A. Soibel, S. A. Keo, J. M. Mumolo, J. Nguyen, and S. D. Gunapala. A high-performance long wavelength superlattice complementary barrier infrared detector. *Appl. Phys. Lett.*, 95:023508 – 023510, 2009.

[124] I. Vurgaftman, E.H. Aifer, C.L. Canedy, J.G. Tischler, J.R. Meyer, J.H. Warner, E.M. Jackson, G. Hildebrandt, and G.J. Sullivan. Graded band gap for dark-current supression in long-wave infrared w-structured type-ii superlattice photodiodes. *Appl. Phys. Lett.*, 89:121114–121117, 2006.

[125] T. Wada and N. Kitamura. *Jpn. J. Appl. Phys.*, 27, 686 (1988).

[126] E. R. Weber. *Advances in Infrared Photodetectors*, volume 84 of *Semiconductors and Semimetals*, page 38. Elsevier, 2010.

[127] Y. Wei, A.Gin, M. Razeghi, and G. J. Brown. Type II InAs/GaSb superlattice photovoltaic detectors with cutoff wavelength approaching 32 μm. *Appl. Phys. Lett.*, 81:3675–3677, 2002.

[128] Y. Wei, A. Gin, M. Razeghi, and G. J. Brown. Advanced InAs/GaSb superlattice photovoltaic detectors for very long wavelength infrared applications. *Applied Physics Letters*, 80:3262–3264, 2002.

[129] Y. Wei, A. Hood, H. Yau, A. Gin, M. Razeghi, M. Z. Tidrow, and V. Nathan. Uncooled operation of type-II InAs/GaSb superlattice photodiodes in the midwavelength infrared range. *Appl. Phys. Lett.*, 86:233106–233109, 2005.

[130] E. Yablonovitch, D.L. Allara, C.C. Chang, T. Gmitter, and T.B. Bright, *Phys. Rev. Lett.*, 57, p.249, 1986.

[131] E. Yablonovitch, C.J. Sandroff, R. Bhat, and T. Gmitter. *Appl. Phys. Lett.*, 51, p.439, 1987.

[132] E. R. Youngdale, J. R. Meyer, C. A. Hoffman, F. J. Bartoli, C. H. Grein, P. M. Young, H. Ehrenreich, R. H. Miles, and D. H. Chow. Auger lifetime enhancement in InAs/GaInSb superlattices. *Appl. Phys. Lett.*, 64:3160–3162, 1994.

[133] Z. Y. Liu, T. F. Kuech, and D. A. Saulys. A comparative study of GaSb (100) surface passivation by aqueous and nonaqueous solutions. *Appl. Phys. Lett.*, 83:2587–2589, 2003.